Interferometric stacks in partially coherent areas
PhD Thesis

Ing. Ivana Hlaváčová
Department of Mapping and Cartography
Faculty of Civil Engineering
Czech Technical University, Prague
Supervisor: Doc. Ing. Lena Halounová, CSc.

Anotace

Práce se zabývá zpracováním 24 družicových radarových snímků metodou radarové interferometrie. Snímky byly pořízeny z družic ERS-1/2 v 90. letech 20. století. Snímky jsou převzorkovány na jeden z nich, utvořeny všechny možné dvojice snímků a z nich interferogramy. Z interferogramů byly vybrány nejvíce koherentní, které následně vstoupily do dalšího zpracování za účelem zmapování poklesů na výsypkách.

Mapovány jsou dvě oblasti: Ervěnický koridor a oblast kolem obce Košťany (okres Teplice). V obou oblastech jsou postaveny umělé stavby (silnice, železnice) na výsypkách, a tyto stavby v průběhu času klesají. Cílem projektu je zjistit rychlost poklesu.

Nejvýznamnějším problémem radarové interferometrie jsou chyby v rozbalení fáze, které se zde snažíme odhadnout a opravit na základě reziduí z vyrovnání – vyrovnání je pak iterativní. Metoda ale není schopna nalézt optimální řešení, jelikož by se jednalo o NP-úplný problém, tj. problém neřešitelný v polynomiálním čase, a tak prohledáváme jen část stavového prostoru.

Výsledky nejsou příliš povzbuzující, avšak jsou definovány dílčí problémy, které je nutno řešit, a po jejich vyřešení očekáváme výrazné zlepšení výsledků.

Abstract

This thesis deals with the processing of 24 radar scenes, acquired by the ERS-1/2 satellites, using the radar interferometry method. The scenes were acquired in 1990s. The scenes were first resampled to one of them, then paired to all possible combinations and interferograms were created from each pair. Out of these, the most coherent were selected for postprocessing. The purpose is to map the temporal progress of subsidence on waste dumps.

Two areas are mapped: the Ervěnice corridor (known for large subsidences in 1980s) and the area around the Košťany village near Teplice. In both areas, artificial objects (roads, railways) are built on waste dumps, and these objects are assumed to subside. The goal of the project is to find out the velocity of the subsidence.

The key problem of radar interferometry are phase unwrapping errors, which we try to estimate and correct on the basis of adjustment residues – the adjustment then becomes iterative. However, finding the optimal solution is a NP-hard problem, unsolvable in a polynomial time, and therefore our method searches only a part of the state space.

Unfortunately, the results are not nice, but particular problems of the method are defined, and we expect a significant improvement after they are solved.

Contents

Acknowledgements

Data for this project were provided by ESA (European Space Agency) within a Category-1 project id 3423.

I would also like to thank to the people supporting me during the years of working: first, to my supervisor, Lena Halounová, and to my husband. Also to other people in the InSAR team: Ján Kianička and Barbora Knechtlová, and to Jan Bitta for several advices in mathematics.

Part I

Theory

Chapter 1

Introduction

Radar interferometry (InSAR) is a method of processing two SAR images acquired by an airplane or a satellite. The satellite transmits a radar signal and receives the echo from a wide swath (about 100 km), allowing to process a large area at the same time.

Synthetic aperture radar (SAR), in comparison to a generic radar, allows to preserve not only the amplitude of the transmitted and received signal, but also its phase. Radar wavelength is in the order of centimeters, allowing to recognize a shift of an imaged object in the order of centimeters - even a few milimeters, if an enhanced processing method is used.

The method can be used for DEM generation, for deformation mapping or for atmospheric delay mapping. In case of DEM generation, the deformations are assumed not to occure and atmospheric delay is treated as noise. For deformation mapping, a DEM is required to be subtracted, and atmospheric delay is again treated as noise. In case of atmospheric mapping, a DEM is required to be subtracted, and a stable area should be used.

Unfortunately, InSAR only works in a coherent area. To be functional, the method requires that two images, which are processed together into an interferogram, are very similar to each other. The interferogram is the difference in phase of the two images, and the phase difference is required to change slowly within the imaged area. In practice, it means that the object surface must not change significantly between the two times of acquisition. On the other hand, if an object, ideally contained in more imaged pixels, moves as a whole, it can be seen in the interferogram and recognized as a deformation.

An ideal area to map by InSAR (with regard to coherence) is a city. It contains many artificial object, such as buildings, roads or bridges, which often reflect the radar signal back to the satellite, and their surface does not change within many years. On the other hand, water surfaces are always decorrelated, and so are vegetated areas, agricultural fields etc.

Enhanced processing methods (Repeat-pass InSAR, Permanent Scatterers) also allow to eliminate some noise effects, such as atmospheric delay, orbit error influence, and also allow to compute DEM error. These methods require many more than two SAR images, and the result is the deformation progress in time, not only the deformation between the two times of acquisition. However, these methods again process two SAR images into an interferogram – they differ from the conventional InSAR only in the postprocessing.

This thesis deals with the Repeat-pass InSAR and uses 24 SAR scenes for processing. The first part contains the InSAR theory, the second part describes the data, processed area, processing procedure and results. Interferometric processing was performed in the GAMMA software, postprocessing was implemented in MATLAB by the author.

Chapter 2

The Basics of the SAR Interferometry

Radar interferometry processes a pair of radar scenes (acquired either by an airplane, or a satellite) in order to get a digital elevation model (DEM). It can also be used for geophysical deformation monitoring, or atmospheric monitoring.

This thesis deals only with satellite radar interferometry. A significant advantage of using satellites is that the position of the radar centre is known to the accuracy of centimeters; on the other hand, the satellite's altitude is much higher than an airplane's – this requires different processing techniques.

In comparison to other remote sensing techniques, radar interferometry takes advantage not only of the magnitude of the signal, but also of its phase. While the signal magnitude corresponds to the reflectivity of the ground, the phase φ corresponds to the distance r between the satellite (*slant range*) and the reflector which is

$$r = n \cdot \lambda + \varphi \frac{\lambda}{2\pi} \tag{2.1}$$

where n is an integer ambiguity and λ is the radar wavelength.

The interferometric processing uses the reflectivity information only for coregistration of the images; for DEM creation, deformation mapping and exploration of the atmosphere, only the phase information is used.

2.1 Terminology

In interferometry, two satellite scenes are used, no matter whether acquired by two satellites or by one satellite in different passes. Let us call one of the scene *master* and the other one *slave*. All results are then related to the master scene.

If more scenes are to be processed, scene pairs must be created first, either by constructing all pairs, or a half of them (exchanging master and slave scene should not make any difference if their orbits are accurate enough).

The distance between the satellites in the moment of acquisiton of the scenes is called *(spatial) baseline* B (it can vary throughout the image if the satellite tracks are not exactly parallel). The baseline is always perpendicular to the master track [33] (actually, the tracks are always almost parallel). We recognize the *perpendicular baseline* $B_\perp$ and *parallel baseline* $B_\parallel$, i.e. perpendicular and parallel to the radar ray transmitted towards the Earth.

Let us emphasize here that radar does not acquire the scenes perpendicular to the Earth surface — the *look angle* Θ (the angle between the Earth normal and radar ray) is 16 – 21 ° (for ERS-1/2). This allows the images to have better resolution than they would have in case of perpendicular view (the radar only allows to measure the distance, not the angle). On the other hand, the *incidence angle* $(\Theta + \varepsilon)$ is the angle between the Earth normal and radar ray at the place where the ray reaches the ground (see figure 2.1). For ERS, the difference between the angles is approximately 4 degrees.

However, the non-zero look angle of the radar results in most of the energy being scattered to all directions and only a small portion coming back to the satellite – the amount of received energy depends largely on the coarseness of the imaged area, e.g. water surfaces reflect almost no energy back to the satellite (if the water is flat, i.e. without waves) and therefore are usually imaged in black; on the contrary, corner reflectors such as buildings or bridges over water are usually imaged brightly.

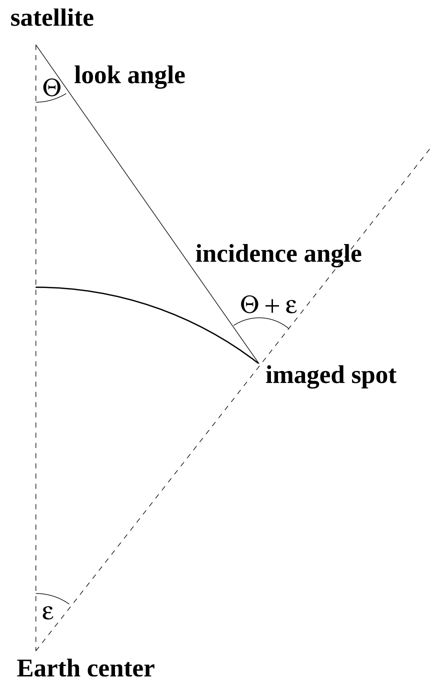

Figure 2.1: The difference between the look angle and the incidence angle.

The *temporal baseline* is the temporal difference between acquisitions of the two scenes.

The radar itself acquires *raw data*, i.e. (sampled) signal in one dimension only (time). This signal needs to be *SAR focused* (see section 3.6) in order to generate the *SLC data* (single-look complex) which are already two-dimensional (in space). These SLC data are used for the interferometric processing.

Another important term is the *height ambiguity*. As mentioned above, the phase value is ambiguous, and so is the height of the reflector computed out of the phase. Height ambiguity is the height difference corresponding to one phase fringe, i.e. 2π radians. Height ambiguity value will be derived and dealt with in Chapter 4.

Let us also mention the resolution of the image. We can distinguish two directions: *azimuth* direction is parallel to the satellite track, while *range* direction is perpendicular to it. The resolution of the acquired scene is approx. 4.5 m in the azimuth direction and 20–30 m in the range direction. Due to the radar acquisiton geometry, the resolution in the range direction changes throughout the image, being better at far range.

Because of the dispropotion between the azimuth and range resolution, the image is often *multilooked*, i.e. n azimuth pixels with the same range are averaged to form one. Then, the resolution becomes approximately the same in both directions. However, multilooking is not recommended to perform before interferogram creation – usually it is performed at the end and multilooked images used only for display.

Let us also define that a scene (image) *line* is a line of the pixels having the same azimuth coordinate, while the range coordinate changes. On the other hand, if we talk of a *pixel* coordinate, we mean the range direction pixel number.

For radar scenes, we need to recognize *slant range* and *ground range*. Taking the first pixel in a line as a reference, the ground range is the distance between the first pixel and the given pixel measured on the (flat) Earth surface, while the slant range is the difference between the distance measured to the first pixel and the given pixel from the satellite.

2.2 Steps of Interferometric Processing

Interferometric processing consists of the following steps:

- Image coregistration and filtering: A pixel in one image must accurately correspond to a pixel in the other image, and also the spectras in both directions must exactly overlap in order to maximize interferogram coherence. Both procedures are described in Chapter 5.

- Interferogram creation: The phases of the two corresponding scenes are then pixel-wise subtracted (using complex conjugate multiplication):

$$I(i,j) = S_1(i,j) \cdot S_2(i,j)^* = |S_1|\,|S_2|\,e^{j(\varphi_1-\varphi_2)} \tag{2.2}$$

  where $I(i,j)$ is the interferogram phase of the (i,j) pixel and $S_k(i,j)$ is the complex value of the master ($k=1$) or slave ($k=2$) scene (pixel (i,j)). Please note that j in the exponent denotes the imaginary unit.

- Computation and subtraction of the flat-Earth phase: The phase of the received signal (i.e. the difference between the received and transmitted signal) is largely dependent on the distance between the transmitter/receiver and the reflector. We want the interferogram phase to be uniform if the imaged area has no topography. Before flat-Earth subtraction, the interferogram mostly consists of parallel lines in the azimuth direction; after subtraction, the most distinctive feature in the interferogram is topography. Flat-Earth phase subtraction is described and derived in Chapter 4.

- Coherence computation: Coherence is a measure for reliability of the phase and is discussed in detail in Chapter 6.

- Interferogram filtering: In order to reduce interferogram noise, the interferogram is filtered. This is in particular useful when the interferogram is unwrapped afterwards, because the noise may significantly reduce the number of residues (for residues, see Chapter 7). Image filtering is performed using an adaptive algorithm, evaluating noisiness of each interferogram segment and constructing a different filter for it. For details, see [12].

- Phase unwrapping: This is a critical step of the interferometric processing. The ambiguous phase in the $\langle -\pi, \pi)$ interval must be converted to an unambiguous value, which can be of any real value. The procedure and its problems are described in detail in Chapter 7.

- DEM phase subtraction: In order to eliminate the topographic signal, the phase corresponding to an external DEM may be subtracted. This DEM needs to be radarcoded first (i.e. converted to the system of radar; after radarcoding, it looks like an interferogram without noise and decorrelated areas) and then subtracted. DEM subtraction is described and derived in Chapter 4.

- Differential interferogram creation: Another way to eliminate the topographic signal from an interferogram is to use an interferogram which is assumed not to contain deformation signal (for deformation mapping; this interferogram usually has a short temporal baseline). The topographic interferogram to be subtracted from the other one must be first unwrapped and rewrapped to correspond with the other interferogram (the height ambiguity must be the same). Then, both interferograms are subtracted. In this thesis, this step is not used and therefore neither described, for details refer e.g. to [41].

- Geocoding: Transformation of the SAR system (line, pixel, phase) to a geographic coordinate system (φ, λ, H_{el}) or (φ, λ, d) where d is the deformation. In the GAMMA software, it is performed using an external DEM: a lookup table between the geographic coordinate system (in which the DEM is defined) and the SAR system is computed at first. Then, a simulated SAR image (amplitude only) may be computed from the DEM and coregistered with the real SAR image, making it possible to correct for orbit errors. However, we found out that the geocoding error does not account for more than a pixel and due to the type of the terrain and crop size it often fails, and therefore we only compute the lookup table and then resample the data using it.

2.3 Applications and requirements

The interferogram (after flat-Earth phase subtraction) contains the following signals:

- topographic signal: corresponds to the actual height of the ground spot (reflector),
- deformation signal: corresponds to the deformations that occurred between the acquisition of the two scenes,
- atmospheric signal: corresponds to the delay of the signal caused by its passing through the atmosphere,
- orbit error influences: the phase changes due to imprecise satellite positions,
- DEM errors: the difference between the real topography in the moment of acquisition and the available DEM to be subtracted; when using the two-pass method, the error of the coregistration between the interferogram and the DEM must be considered as well.

Interferometry is often used for DEM creation. In this case, the perpendicular baseline should be as large as possible, in order to reach a low height ambiguity and therefore a high height accuracy of the DEM. For ERS-1/2, the upper limit of the spatial baseline is about 2 km; for such a long spatial baseline, the phase information of the two scenes is too different to allow coregistration. On the other hand, the temporal baseline should be as short as possible in order not to allow too much decorrelation and ground deformation.

When used for deformation mapping, the perpendicular baseline should be as short as possible in order to reduce the topographic signal in the interferogram as much as possible. Even if the interferogram contains the topographic signal and a DEM must be used in order to eliminate it, a higher height ambiguity means reduced accuracy requirements for the DEM. The temporal baseline should be long enough to allow the deformations to occur, but the deformations can't be too large. (If the deformation slope exceeds 2.8 cm/px, phase unwrapping is very unreliable, and large deformations also cause decorrelation, especially when occuring in the azimuth direction.) An optimal way is to process a larger set of scenes. There are many "spots" in an interferogram which need to be verified in other interferograms or by other methods in order to be sure that they are caused by a deformation. Interferometric stacks also allow to estimate and filter out the atmospheric contribution; however, the procedure requires the temporal sampling to be dense enough so that the deformation signal changes only slowly between particular acquisition times.

Other research groups often map deformations after an earthquake; if these earthquakes occur in a desert, there are no decorrelated areas there and the deformations are large enough to produce fringes. Detecting landslides is more difficult because the landslides themselves often cause decorrelations and may not be large enough to be visible in an interferogram.

It is also possible to determine some properties of the atmosphere using radar interferometry. It has been proven (see e.g. [34, 35]) that weather changes (fronts, storms) cause a great heterogeneity in the signal delay.

For topographic or deformation mapping, data selection is often performed with the purpose of eliminating these effects, i.e. no rain and snow dates are preferred. If there is no storm (or similar phenomenon) in the mapped area, the atmospheric influence usually has a "long-wave" characteristics, i.e. changes slowly in the area (see e.g. [17]).

The atmospheric influence (i.e. delay) depends not only on the weather conditions, but, according to [19], it also depends considerably on the range, i.e. on the look angle. For an increasing look angle, the path of the ray through the atmosphere gets longer. The atmospheric delay may reach the value of 15 m but the difference between the two acquisitions is expected to be lower. This influence is significant if the perpendicular baseline is very short, or if one acquisition is performed at night and the other during the day. However, ERS-1/2 satellites are sun-synchronous, and therefore all scenes acquired at the same track have a very similar acquisition daytime.

Atmospheric influence is dealt with in detail in section 9.4.

Another important feature of the method is that all measurements are relative. Theoretically, the phase of the differential interferogram should be zero in areas of no deformation, but there are systematic errors influencing the measurements and therefore the deformations (or DEM) can be determined only relatively with respect to the surroundings.

2.4 Problems of the Method

The most important problem of the method is decorrelation. All vegetated areas are decorrelated due to the fact that their surface changes (the movement of leaves etc.) are comparable to the radar wavelength. The only way to overcome this is to acquire both scenes simultaneously, such as in the SRTM (Shuttle Radar Topography Mission) mission.

Water surfaces are always decorrelated. The surface moves so quickly that it is impossible to see it correlated even in the case of simultaneous acquisition of both scenes. In addition, only a small portion of the transmitted signal is reflected back to the radar.

In our area of interest, which is covered by large open mines, another problem may be an old DEM. Also, DEMs acquired by different methods may cause a problem because radar interferometry (C-band) maps the top of forests, in comparison to geodetic methods, which map the ground.

A little disadvantage of the two-pass method with the use of SRTM DEM is that all computation are performed in the WGS-84 coordinate system and the heights are related to the WGS-84 ellipsoid, while the SRTM DEM is related to the geoid. Fortunately, the difference between the bodies is neglectable in the areas where the geoid-to-ellipsoid offset is changing only slowly (i.e. causes only a bias).

Chapter 3

Image Acquisition

The acquisition principle of the radar systems is different than that of a usual remote sensing system. Let us deal only with satellite systems here.

Radar antennas are, in comparison to photography, unable to recognize the angle from which the signal comes, they only transmit a signal of beamwidth β. The beam should be as narrow as possible in order to reach a good spatial resolution – however, the narrower the beam, the (physically) longer antenna is neccessary. For satellites, an optimal antenna length would be about several hundreds meters, which is impossible to construct (and in addition, satellite stability could be jeopardized). For antennas being used in satellite SAR systems, the azimuth resolution would be several kilometres (in the ground range).

Therefore, synthetic aperture radars (SARs) are used to obtain better resolution. The principle of SAR is using a short antenna and processing the signal in a way allowing to reach the spatial resolution of a few meters. The requirement for a radar to be used as a SAR is that it must be coherent, i.e. phases of both the transmitted and the received signals are stored.

The principle of radar image acquisition consists of emitting pulses of a predefined length and shape and measuring the echo. The time of reception of the backscattered signal is given by the distance of the resolution cell, its magnitude is given by the backscattering properties of the resolution cell.

3.1 Spatial resolution

For SAR systems, we consider resolution in two directions:

- In the azimuth direction, the resolution is determined by the antenna length (aperture).
- In the slant range direction, the resolution is given by the effective pulse length.

The synthetic aperture is (according to [31]) "equal to the distance the satellite travelled during the integration time" illuminating the given resolution cell; according to [1], it is the length of the radar footprint in the azimuth direction. Due to the relativity principle, both definitions are equivalent.

Pulse repetition frequency (PRF) is limited by the antenna length and satellite velocity. According to [25], "in SAR, the satellite must not cover more than half of the along-track antenna length between the emission of successive pulses. For example, a 10-m antenna should advance only 5 m between pulses, to produce a 5-m-long final elementary resolution pixel. For a satellite traveling approx. 6 km s^{-1} over the ground, this implies a PRF of approx. 1 kHz."

In comparison to real aperture radars, where the resolution is given by the radar footprint, the important feature of SAR (see [32]) is that the azimuth and range resolutions are independent. This is due to the fact that more distant areas are observed longer.

3.2 Phase behaviour

Both the phase and the amplitude, i.e. the entire complex signal, are constructed from many little reflectors within the given resolution cell (approximately corresponding to a pixel). That is, reflectors with a better reflectivity have more influence on the resulting phase (please note that the signal wavelength of 5.6 cm is much smaller than the resolution cell (approx. 20 m in the range direction)) than less-reflecting objects. Construction from many small objects may sometimes be an obstacle for interferometry: the phase is naturally random and if the look angles of the two images differ too much (the parallel baseline is too long), i.e. also the incidence angles are different, the phases of the corresponding pixels are uncomparable and irregular with respect to the image. That is the reason why the upper limit for the baseline is about 2000 m for ERS-1/2 (derived e.g. in [25]). That is also the reason why data from different tracks or even different satellites cannot be combined to produce an interferogram (however, ERS data may be combined with ENVISAT data but the optimal perpendicular baseline is not zero – for details, see [10]). Even combining data of the descending and the ascending passes of the same satellite is not easy; a solution is suggested in [8].

Also, the phase is "stable" and therefore useful only in "stable" areas. The "stability" is meant in relation to the wavelength – i.e. artificial objects such as buildings and roads are stable but trees (with moving leaves) are very unstable, except for the winter season when they have no leaves. The same applies to fields and meadows – these areas are useful for interferometry only in late autumn and early spring. Also, water or snow bodies are considered to be "unstable" except for areas of permanent snow or glaciers.

Let us note here that if we take the two images at the same time – as was the case of the SRTM mission [28], or airborne radars – this problem of stability arises only over water bodies whose surface changes very quickly. The "fundamental condition for interferometry" [25] is

$$2L(\sin\theta_1 - \sin\theta_2) < \lambda \tag{3.1}$$

where L is the ground-range pixel length (approx. 20 m at far range), θ_1 and θ_2 are the incidence angles of the two images respectively, λ is the radar wavelength. The difference in round trip distance of both ends of a pixel is $2L \sin\theta$ and the condition (3.1) means that the phases of all the small targets within a pixel subtract in a similar way — if the condition wasn't satisfied, the targets would add both constructively and destructively and the resulting phase difference would be random, without any meaning. Let us emphasize here that θ_1 and θ_2 are the incidence angles so the quality of the interferogram is also influenced by the local terrain slope.

Also, according to [25], the "direction of observation must be identical for the two images" in the along-track direction. "The degradation becomes total when the angle between the two directions of observation exceeds the width of the antenna beam ($0.3\,^o$ for ERS-1/2)." This corresponds to "excessively large difference" between the Doppler centroids of the two images. Doppler centroid is explained below.

According to [1], let us consider two processes: SAR data acquisition, that is the conversion from the reality (with the infinitesimal resolution) to the raw data (blurred due to the SAR principle), and SAR processing, i.e. conversion from the raw data to the image (with resolutions cells about 20 by 5 meters large). SAR processing is therefore the inverse process to data acquisition.

3.3 Antenna

Let us have a rectangular antenna with the (azimuth) length of L_a and (range) width of D_a. The normalized antenna pattern (i.e. the transmitted energy as a function of the off-center beam angles ϕ_r (range) and ϕ_a (azimuth)) can be written as (λ is the radar wavelength)

$$a(\phi_r, \phi_a) = \frac{\sin^2\left(\frac{D_a}{\lambda}\phi_r\pi\right)}{\left(\frac{D_a}{\lambda}\phi_r\pi\right)^2} \cdot \frac{\sin^2\left(\frac{L_a}{\lambda}\phi_a\pi\right)}{\left(\frac{L_a}{\lambda}\phi_a\pi\right)^2}$$

and a 2-dimensional simplification is shown in figure 3.1.

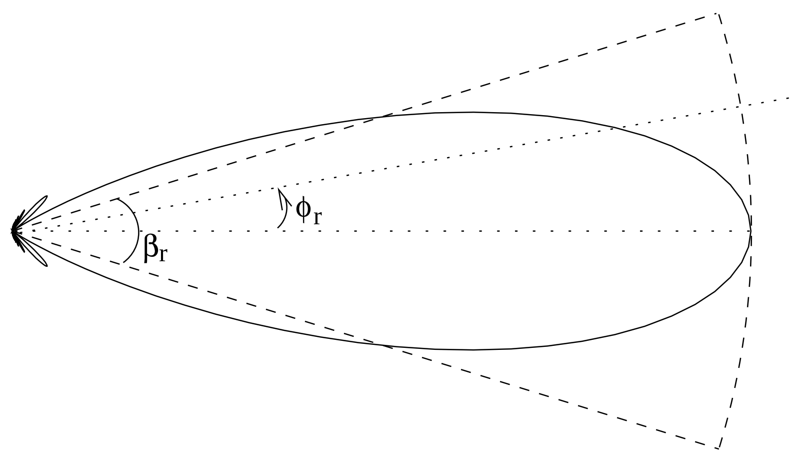

Figure 3.1: 2-dimensional antenna pattern, with β_r as the beamwidth

For ERS-1/2, the antenna length is $L_a = 10$ m, the antenna width is $D_a = 1$ m [26].

For simplification, let us consider (as usual) the antenna pattern to be a triangle, having the slopes where the "real" antenna pattern has a half power (-3 dB) (see the dashed line in figure 3.1). Now, the beamwidths in the azimuth and range direction are $\beta_r = 0.886\frac{\lambda}{D_a} = 2.870°$, $\beta_a = 0.886\frac{\lambda}{L_a} = 0.287°$ [26].

The pattern within this angle limit is called the "main lobe", all the energy transmitted outside the limits is attributed to "sidelobes."

According to [17], the beamwidth of the main lobe is slightly broadened in range direction, "in order to get the power distributed more evenly across the full swath" [26]. In practice, the beamwidths in range and azimuth direction are [17] $\beta_r = 5.4°$ and $\beta_a = 0.228°$ respectively. This is inconsistent with beamwidths presented in [26] and [1], where $\beta_a = 0.208°$. The inconsistency is probably caused by different consideration of limits (i.e. "first zero" versus "half power" and possibly by taking Earth rotation into account).

3.4 Range processing

Let us define two time scales: the first one, let us call it "fast time" [1] and denote τ, concerns the range processing. The transmitted pulse is just $37.1\mu s$ long and the echo, although a little longer, contains the information to be separated to pixels in one line in the range direction. The other time scale, let us call it "slow time" and denote t, concerns the pulses; the pulses are transmitted with the frequency of PRF = 1680 Hz and the echo to each pulse generates a distinct line in the azimuth direction.

Because there is a several orders of magnitude difference between these two time scales, we can consider them to be independent. After range decompression, azimuth decompression is performed after range migration correction (will be discussed later).

The radar emits pulses of the length $\tau_p = 37.1\mu s$ with the PRF of 1680 Hz. After transmitting nine such pulses, first echo is received. According to [1], let us ignore the fact that the spacecraft moved between the transmission and reception. The swath width (in ground range) is about 100 km, short enough to enable reception of the whole echo before transmitting another pulse. Thus, one antenna is used for both transmission and reception.

The transmitted frequency-modulated pulse can be written as

$$p_t(\tau) = g(\tau) \cdot \exp(-j2\pi f_0 \tau), \tag{3.2}$$

where $g(\tau)$ is the (complex) envelope, τ is the "fast time" and $f_0 = 5.3$ GHz is the carrier frequency (corresponding to the radar wavelength $\lambda = 5.6$ cm). The envelope could be a regular rectangle but, in this case, it would be a problem to transmit a great power within a short pulse; a longer pulse would cause worse resolution. That is why longer phase-coded pulses are used. Thus the envelope to be modulated is

$$g(\tau) = \exp(j\pi k\tau^2) \cdot \mathrm{rect}(\tau k/B_\nu), \tag{3.3}$$

where k is the frequency modulation rate (for ERS-1/2, $k \approx 0.42MHz/\mu s$) and B_ν is the range bandwidth (i.e. maximal frequency of the chirp before modulation).

The rect(x) function is defined in the following way [1]: for $|x| < \frac{1}{2}$, rect$(x) = 1$; for $|x| = \frac{1}{2}$, rect$(x) = \frac{1}{2}$; and for $|x| > \frac{1}{2}$, rect$(x) = 0$.

That means that the frequency of the chirp increases linearly, reaching the maximum of $\nu = 15.55$ MHz (for ERS-1/2) for $\tau = \tau_p$.

The transmitted signal therefore looks like (omitting the magnitude)

$$p_t(\tau) = \exp\left(-j(2\pi f_0 \tau - k\tau^2)\right), \tag{3.4}$$

its phase is

$$\phi(\tau) = 2\pi f_0 \tau - k\tau^2, \tag{3.5}$$

i.e. in the phase image and further processing, the radar wavelength of 5.6 cm corresponds to the 4π phase cycle (because the phase is influenced by the round-trip distance).

The received signal (after demodulation and comparison with the transmitted one) has the form of (omitting the magnitude)

$$p_r(\tau) = g(\tau - 2R/c) \cdot \exp(-j4\pi R/\lambda), \tag{3.6}$$

where R is the range and c is the speed of light. The phase $4\pi R/\lambda$ must be stored before further processing.

According to [26], "processing of the returned signal involves stripping off the carrier frequency and performing a correlation with a copy of the transmitted signal". According to [17], the stripping off means down-conversion of the signal to the intermediate frequency of 123 MHz and sampling with the frequency of 18.96 MHz.

The received pulse after matched filtering has the form of [26]

$$h_r(\tau) = (\tau_p - |\tau|) \frac{\sin\left(k\tau\left(\tau_p - |\tau|\right)\right)}{k\tau\left(\tau_p - |\tau|\right)} \mathrm{rect}\left(\frac{\tau}{\tau_p}\right). \tag{3.7}$$

For the case of a single scatterer, this function has a sharp maximum at τ_d corresponding to the real time delay (phase). According to [26], the first zero of this signal is often taken as a measure of the time resolution

$$r_\tau = \frac{\tau_p}{2}\left(1 - \sqrt{1 - \frac{4}{B_\nu \tau_p}}\right). \tag{3.8}$$

Now the compression ratio is $\frac{\tau_p}{r_\tau}$ and r_τ is selected to be $r_\tau \approx \frac{1}{B} \approx 64$ ns. This is the effective pulse length, i.e. the length of a rectangular pulse to achieve the same range resolution.

The slant range resolution is then 9.68 m (according to [26, 17]) or 8.56 m (according to [1] where half-power values are considered), corresponding to the ground range of 21.8 m (at far range) to 29.3 m (at near range) [26].

For radar data, it is usual for the pixel to be slightly larger than the resolution (i.e. the pixels overlap a little). This is given by the non-sharp antenna pattern and spectra in both the azimuth and the range directions.

The resolution is then degraded by weighting the correlation function due to the sidelobes [26].

3.5 SAR principle

The azimuth beamwidth is $\beta_a \approx 0.287°$, corresponding to approx 4.5km pixels in the ground range. This is quite a large area, useless for further applications. But, if SAR processing/focusing is done, the resolution improves to approx. 5m. The following derivation comes from [26].

The azimuth direction is the direction of the satellite movement vector $\vec{v}$. The received echos are influenced by the Doppler effect, i.e. the frequency of the received signal is different than the frequency of the transmitted signal. Also, the actual received frequency depends on the position of the scatterer in the beam. There is always a direction in which the Doppler shift is zero, called zero-Doppler plane. Unfortunately, due to small instabilities of the satellite movement, Earth rotation and other effects, this zero-Doppler plane is not in the center of the beam, i.e. the beam is not exactly perpendicular to the flight direction (with regard to the ground) – the difference between the perpendicular direction and the beam center is called a *squint angle* ψ . The frequency which is received from the beam center is called the Doppler centroid f_{DC} and is always smaller than the PRF. It is given by [1]

$$f_{DC} = -\frac{2v}{\lambda} \sin \psi. \tag{3.9}$$

The value of the Doppler centroid is computed during SAR processing and can be also changed during the process which may be useful for SAR interferometry – in the optimal case, both images have the same Doppler centroid [25]. However, in this case we would had to order RAW data and convert them to SLC ourserves.

Because the echo of a given scatterer is received within many pulses (all the time while staying within the radar beamwidth), the SAR processing procedure needs to be done first, in order to improve the resolution. Although improving range resolution is quite simple (it is a one-dimensional problem), improving azimuth resolution is more complex, mainly due to range migration.

Range migration means that the range between the scatterer and the receiver is changing during acquisition. During acquisition, received data are stored in lines with respect to the "fast time" of their reception. That means that a scatterer lies on an approximate hyperbola (see [1] for a more exact approach or derivation) in the raw data matrix. Also, the curvature of hyperbolas is dependent on the minimal range of the scatterer (see [1]). This makes the problem of SAR focusing "two-dimensional and non-separable" [1].

Now, let us derive the achievable azimuth resolution (taken from [26]):

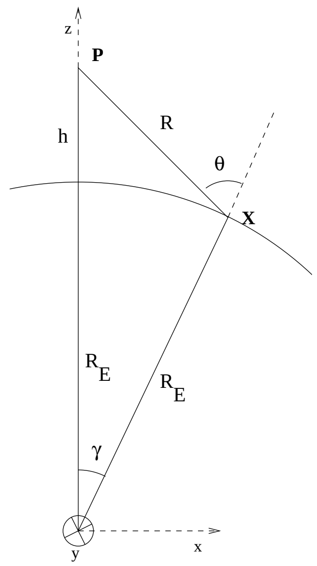

Figure 3.2: Coordinate system for azimuth resolution derivation. This figure is taken from [26].

A point X (located on the Earth's surface) has coordinates of $X = R_E(\sin\gamma, 0, \cos\gamma)$ (see figure 3.2), the satellite has coordinates of $P = (R_E + h)(0, \sin\Omega t, \cos\Omega t)$, where Ω is the Earth rotation speed, t is the time and h is the satellite height. Let us define R_0 as the minimal slant range at time 0, $R_0 = |X - P|_{t=0}$. Then

$$R_0 = \sqrt{(R_E \sin\gamma)^2 + (R_E \cos\gamma - (R_E + h))^2}, \tag{3.10}$$

$$\begin{aligned} |X - P| &= \sqrt{(R_E \sin\gamma)^2 + ((R_E + h)\sin\Omega t)^2 + (R_E \cos\gamma - (R_E + h)\cos\Omega t)^2} && (3.11) \\ &= \sqrt{R_0^2 + 2R_E(R_E + h)\cos\gamma\cos\Omega t}, && (3.12) \end{aligned}$$

$$|X - P| \approx R_0 + \frac{R_E(R_E + h)\cos\gamma\Omega^2 t^2}{2R_0} \tag{3.13}$$

for small values of Ωt, corresponding to the small beamwidth. Therefore, the corresponding (two-way) phase of the received signal is [26]

$$2\varphi(t) \approx \frac{-4\pi R_0}{\lambda} - \frac{2\pi}{\lambda}\frac{R_E(R_E + h)\cos\gamma\Omega^2 t^2}{R_0}, \tag{3.14}$$

which is equivalent to linear frequency modulation. Frequency variation of

$$f_d = \frac{1}{2\pi}\frac{d\varphi}{dt} \approx -\frac{2}{\lambda}\frac{R_E(R_E + h)}{R_0}\cos\gamma\Omega^2 t$$

gives the half-Doppler-bandwidth for maximum allowed t_{max}, which is the half-time of illumination of a ground point.

The illuminated area on the ground (the synthetic aperture length) is approximately $R_0\beta_a$ and the ground velocity of the beam is $v = R_E\Omega\cos\gamma$, so the half-time of illumination is

$$t_{max} = \frac{1}{2}\frac{R_0\beta_a}{R_E\Omega\cos\gamma}, \tag{3.15}$$

corresponding to the resulting (Doppler) bandwidth of

$$B_\nu = \frac{2}{\lambda}\beta_a(R_E + h)\Omega. \tag{3.16}$$

Time resolution (according to the above relations) is $\tau_a = 1/B_\nu$, and during the time, the beam moves a ground distance of $v\tau_a$ and the azimuth resolution therefore is

$$r_a = \frac{R_E}{R_E + h}\cos\gamma\frac{\lambda}{2\beta_a}, \tag{3.17}$$

i.e. approximately 4.5m for ERS-1/2 SAR.

3.6 SAR processing (focusing)

This section is based on [1].

The SAR focusing procedure should “unblur” the raw data, i.e. separate the contributions from the “real” resolution cells. As already noted, it is approximately an inverse procedure to the data acquisition. Without SAR focusing, the data would be unusable because of very large resolution cells.

The first step of SAR focusing is the range decompression, i.e. correlation of the received signal with the transmitted one (both demodulated), resulting in the delay τ, determining the pixel to which the phase and magnitude of the received signal are stored.

Second, the Doppler centroid is estimated. It is done by the spectral analysis in the azimuth direction. According to [1], “since the Doppler centroid frequency varies over range, estimation is performed at several range positions.”

After that, range migration correction is performed. That means transforming the approximate hyperbola in which a given scatterer lies (the exact shape of the curve depends, among others, on the actual range) to a line in the azimuth direction. This means that the signal needs to be shifted back in the τ direction and, because a single pixel of the actual data corresponds to many scatterers with different range migration corrections, this is not a trivial problem and there are at least four approaches to its solution. One of them is range-Doppler (the others are named in [25]), which first computes the Fourier transformation of the data in the azimuth direction, separating the data with different Doppler frequency and therefore with different range. The data are then focused in this range-Doppler domain (i.e. the range direction is not transformed unlike the azimuth one). For more details, see e.g. [1].

After range migration correction, azimuth decompression is a one-dimensional problem. It is done by correlation with the azimuth chirp.

Chapter 4

SAR Geometry

This chapter deals with the geometrical model of SAR interferometry. From now on, we only deal with the SLC data, i.e. SAR-focused raw data. The relation between the phase of the SLC data for a particular pixel and its elevation (with regard to a reference body) or deformation is derived here. All relations include the perpendicular baseline $B_\perp$ or the parallel baseline $B_\|$, which are defined in Chapter 2.

4.1 Height ambiguity

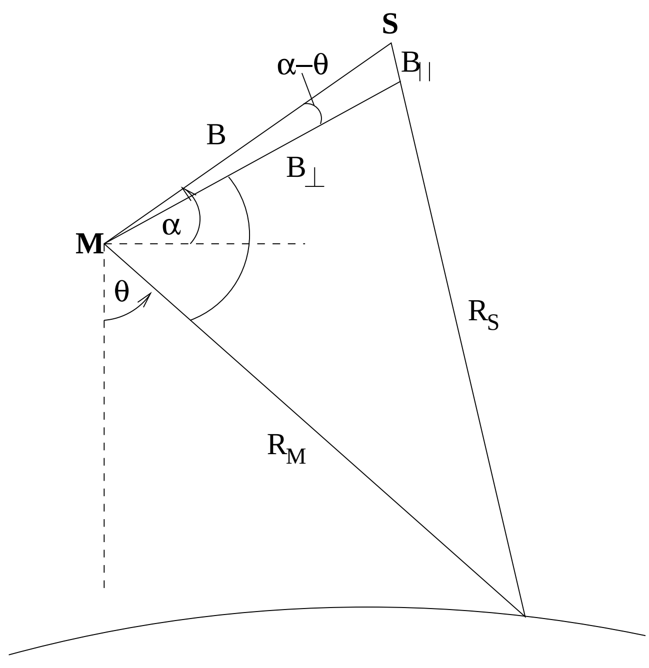

Figure 4.1: Geometrical model of radar interferometry, M denotes the satellite acquiring the master scene, S denotes the satellite acquiring the slave scene. The figure is taken from [21].

The following derivation of the height ambiguity value and flat-Earth phase is taken from [21]. The parallel and perpendicular components of baseline can be expressed as (see figure 4.1)

$$B_{\|} = R_M - R_S = B\sin(\Theta - \alpha), \tag{4.1}$$

$$B_{\perp} = B\cos(\Theta - \alpha). \tag{4.2}$$

Meaning of the symbols used should be clear from figure 4.1. Please note that we only deal with the plane containing both satellites and the reflector. The phases of a pixel corresponding to a reflector at the distance R_M from the satellite M and at the distance R_S from the satellite S are:

$$\varphi_M = -\frac{4\pi}{\lambda}R_M + \varphi_{err,M}, \tag{4.3}$$

$$\varphi_S = -\frac{4\pi}{\lambda}R_S + \varphi_{err,S} \tag{4.4}$$

where $\varphi_{err,M}$ and $\varphi_{err,S}$ are phase errors due to e.g. atmospheric delay of the radar signal. The difference between the phases of the master and slave scenes (interferogram phase) is therefore

$$\Delta\varphi = -\frac{4\pi}{\lambda}(R_M - R_S) + \Delta\varphi_{err} = -\frac{4\pi}{\lambda}B\sin(\Theta - \alpha) + \Delta\varphi_{err} = \Delta\varphi_E + \Delta\varphi_{tpg} + \Delta\varphi_{err}, \tag{4.5}$$

where $\Delta\varphi_E$ is the flat-Earth phase

$$\Delta\varphi_E = -\frac{4\pi}{\lambda}B\sin(\Theta_0 - \alpha), \tag{4.6}$$

where Θ_0 is the look angle for the point on an arbitrary reference surface (this value changes according to the reference surface), $\Delta\varphi_{tpg}$ contains the topographic signal and $\Delta\varphi_{err}$ contains deformation and atmospheric signals.

According to formula (4.5), the topographic influence can be modeled as

$$\Delta\varphi_{tpg} = -\frac{4\pi}{\lambda}B\left(\sin(\Theta_0 + d\Theta - \alpha) - \sin(\Theta_0 - \alpha)\right) \approx -\frac{4\pi}{\lambda}B_{\perp}d\Theta, \tag{4.7}$$

where $\Theta = \Theta_0 + d\Theta$. Here we consider $d\Theta$ to be very small, i.e. $\sin d\Theta \approx d\Theta$ and $\cos d\Theta \approx 1$.

The height of a point on the Earth surface (above the reference surface) may be derived according to figure 4.2.

Assuming the interferogram contains only the topographic signal, i.e. $\Delta\varphi = \Delta\varphi_{tpg}$, the value of $d\Theta$ is according to formula (4.7)

$$d\Theta = -\Delta\varphi\frac{\lambda}{4\pi}\frac{1}{B_{\perp}}, \tag{4.8}$$

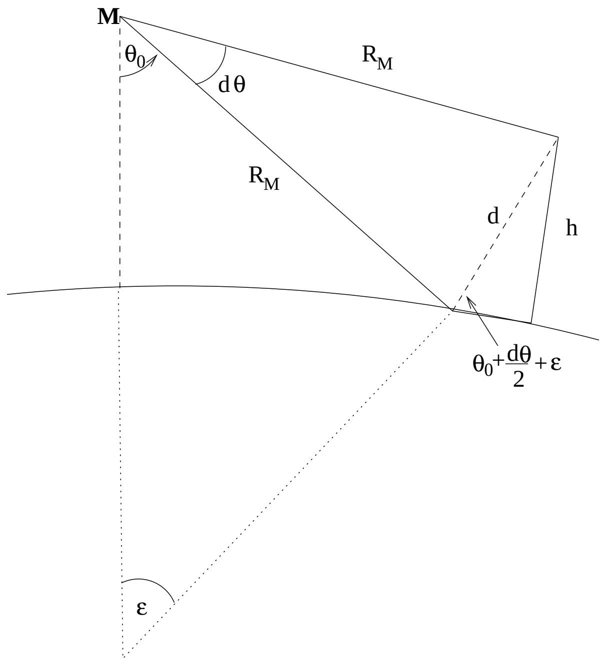

Figure 4.2: Height ambiguity derivation

the distance d is (see figure 4.2)

$$d = R_M \sqrt{2}\sqrt{1-\cos d\Theta} = 2R_M \sin\frac{d\Theta}{2}, \tag{4.9}$$

and the height h above the reference surface is therefore (see figure 4.2)

$$h = d \sin\left(\Theta_0 + \frac{d\Theta}{2} + \varepsilon\right). \tag{4.10}$$

With a few substitutions we get (assuming $\sin^2 \frac{d\Theta}{2} \approx 0$ and $\cos \frac{d\Theta}{2} \approx 1$)

$$h = 2R_M \sin\left(\Theta_0 + \varepsilon\right) \sin\frac{d\Theta}{2}, \tag{4.11}$$

where $\Theta_0 + \varepsilon$ is the incidence angle.

The height ambiguity (i.e. the height difference corresponding to a 2π phase difference) is, using (4.8) and (4.11) and considering $\sin\frac{d\Theta}{2} \approx \frac{d\Theta}{2}$,

$$h_a = -R_M \sin\left(\Theta_0 + \varepsilon\right) \frac{\lambda}{2} \frac{1}{B_\perp}, \tag{4.12}$$

which is in accord with, e.g., [17]. However, this is only an approximate value because R_M also changes with the look angle Θ. In addition, please note that the height ambiguity changes throughout the image: the length of the perpendicular baseline changes, and so does the look angle Θ and the distance to the master satellite R_M. However, the height ambiguity is used for data selection and pair comparison, and it is precise enough for these applications.

4.2 Deformation

We can also derive the error phase $\Delta\varphi_{err}$, used in formula (4.5), which can also include the deformation signal:

$$\Delta\varphi_{err} = \Delta\varphi_{atm} + \Delta\varphi_{defo} + \Delta\varphi_{other} = \Delta\varphi - \Delta\varphi_E - \Delta\varphi_{tpg} \tag{4.13}$$

i.e.

$$\Delta\varphi_{defo} = \Delta\varphi - \Delta\varphi_E - \Delta\varphi_{tpg} - \Delta\varphi_{atm}, \tag{4.14}$$

where $\Delta\varphi_{defo}$ is the phase corresponding to the geophysical deformation that has occured between the acquisition times of the two scenes, $\Delta\varphi_{atm}$ is the difference between atmospheric delays during the two acquisitions, and $\Delta\varphi_{other}$ is the noise caused by other causes, see Chapter 9. Due to the fact that we cannot evaluate the last two phases, we will consider them stochastic (see Chapter 8). The topographic phase is then defined (using formula (4.11)

$$\Delta\varphi_{tpg} = -\frac{4\pi}{\lambda}\frac{B_\perp}{R_M\sin(\Theta_0+\varepsilon)}h, \tag{4.15}$$

using the same approximations as in formula (4.12), and the deformation phase relates to the actual deformation with a simple formula

$$\Delta\varphi_{defo} = -\frac{4\pi}{\lambda}D, \tag{4.16}$$

where D is the deformation in the line of sight.

Chapter 5

Coregistration and Filtering

Two scenes need to be coregistered in order to accurately overlap, pixel by pixel. According to [17], the coherence lowers with the worsening coregistration accuracy, and the accuracy of a tenth of a pixel is found out to be sufficient.

During spectral filtering, the non-overlapping parts of the spectra of the master and slave images are eliminated. If there are non-overlapping parts of the spectras, the interferogram also may be (partially) decorrelated [3].

In other words, the coregistration procedure makes the two scenes exactly overlap in the spatial dimension, while the filtering procedure makes the two scenes exactly overlap in the frequency dimension. Both procedures apply to both azimuth and range directions.

5.1 Coregistration

Coregistration has two phases: first, the overlapping (low-order) polynomial is computed, and then the slave scene is resampled with regard to the polynomial.

The shift between the two scenes is not constant. This is caused by the following factors:

- the orbits need not be exactly parallel, therefore causing one scene to be little rotated with respect to the other,
- if the scenes were acquired from different SAR centers, the resolution is different for each scene (the resolution depends on range),
- if the scenes were acquired from different SAR centers, the look angle changes, and so do effects such as layover and shadow.

However, no rotation angle is enumerated during the coregistration process. The shift between the two scenes is evaluated as a 2D polynomial. An approximate shift between the scenes must be known a-priori, either estimated manually from image magnitude, or from satellite positions during acquisition. Let us call this approximate shift s_a^{apr} in the azimuth direction and s_r^{apr} in the range direction. The required accuracy of the shift estimation depends on the window inside which the shift is enumerated.

Then, both scenes are cut into small windows (in the GAMMA software, window size may be user-adjusted) which should approximately overlap. Then, all windows are oversampled by a (user-defined) factor (about 16, the precision required is about one tenth of a pixel) and the correlation function between the windows is computed

$$C(s_a, s_r) = \frac{\sum_i \sum_j A_m(i,j) \cdot A_s(i - s_a, j - s_r)}{\sqrt{\sum_i \sum_j A_m(i,j) \cdot A_m(i - s_a, j - s_r) \sum_i \sum_j A_s(i,j) \cdot A_s(i - s_a, j - s_r)}}. \quad (5.1)$$

where i, j are the azimuth and range indices and should cover the window size, A_s is the (adjusted) magnitude of the master image and A_s is the (adjusted) magnitude of the slave image. The correlation is computed for all possible values of s_a and s_r, i.e. throughout the window.

Image magnitudes in each window must be first adjusted: they must have zero mean. Then, the shift in both direction is evaluated as

$$\{s_a, s_r\} = \max C(s_a, s_r) \quad (5.2)$$

The shift is evaluated in each window independently. The number of windows may be user-adjusted and the windows may overlap, resulting in the shift to be evaluated in a very dense net of pixels.

Then, the shift is divided by the oversampling factor, in order to exactly correspond to the pixels, and is referenced to the window center. A polynomial function of a low degree is used to define the scene shift for each scene point.

Finally, let us note that the described method is computationally inefficcient. In actual implementations, the shift for each window is evaluated using FFT. However, the result stays the same.

5.2 Introduction to spectral filtering

Spectral filtering can be written as a multiplication with a window in the spectral domain [3]

$$F'(f) = F(f) \cdot Q(f), \quad (5.3)$$

where $F(f)$ is the original scene spectrum (in the range direction), $Q(f)$ is the spectral filter and $F'(f)$ is the resulting scene spectrum.

The simplest spectral filter is a rectangular window, defined as

$$Q_{rect}(f) = \begin{cases} 1, & f_{low} \leq f \leq f_{high} \\ 0, & \text{elsewhere} \end{cases} \quad (5.4)$$

where f_{low} and f_{high} are defined on the basis of spectral overlap of the two scenes (from one scene, the higher part of the spectra is eliminated, for the other, the lower part of the spectra is eliminated. The eliminated parts have the same extent – considering that the spectra of both original scenes have the same width).

However, this filter causes overshooting in the spectral domain, and therefore it is not optimal. The following windows are used instead [3]:

- Von Hann window, defined as

$$Q_{Hann}(f) = \begin{cases} 0.5 + 0.5\cos\frac{2\pi f}{f_{high} - f_{low}}, & f_{low} \leq f \leq f_{high} \\ 0, & \text{elsewhere}, \end{cases} \tag{5.5}$$

- Hamming window, defined as

$$Q_{Hamming}(f) = \begin{cases} 0.54 + 0.46\cos\frac{2\pi f}{f_{high} - f_{low}}, & f_{low} \leq f \leq f_{high} \\ 0, & \text{elsewhere}, \end{cases} \tag{5.6}$$

- or general Hamming window, defined as

$$Q_{Hamming}(f) = \begin{cases} \alpha + (1-\alpha)\cos\frac{2\pi f}{f_{high} - f_{low}}, & f_{low} \leq f \leq f_{high} \\ 0, & \text{elsewhere}, \end{cases} \tag{5.7}$$

  where α is a parameter (for ERS data, $\alpha = 0.75$ is used most frequently).

5.3 Range filtering

The bandwidth in the range direction (i.e. the difference $f_{high} - f_{low}$, below referred to as range bandwidth) is given by the maximum chirp frequency (see section 3.4), i.e. is constant for a given platform. However, the spectra of two scenes acquired by the same platform from the same orbit do not have to exactly overlap.

A difference in the incidence angles of one point during the two acquisition causes that the received signal has a different phase, resulting in decorrelation. The difference in phase can be displayed as a spectral shift of one of the scene with regard to the other, if the FFT (fast Fourier transform) of the scene in the range direction is performed.

The change in the look angle is small, same as the perpendicular baseline. However, elimination of the non-overlapping parts of the spectra results in a higher coherence of the image; however, a part of the image information gets lost.

The spectral shift between two scenes may be evaluated as [3]

$$\Delta f = \frac{B_{\perp} c}{\lambda r_0 \tan(\Theta - \alpha)}, \tag{5.8}$$

where c is the speed of light, r_0 is the (approximate) distance between the scatterer and one of the satellites, and α is the topographical slope. Please note that if the perpendicular baseline is so long that the frequency shift is larger than the range bandwidth, the scenes cannot be coregistered at all.

5.4 Azimuth filtering

Similarly to the range direction, the scene spectrum in the azimuth direction has an (approximately) predefined form. The bandwidth is constant (1378 Hz [3]) and it is centered around the Doppler centroid frequency (see section 3.5).

This is given by the fact that the range of frequencies acquired during the overflight is approximately constant (depends mostly on the speed of the satellite with regard to the ground and the beamwidth); however, the direction where the Doppler shift is zero, may be different (depends on the squint angle, as mentioned in section 3.5).

The spectral shift between two scenes may be caused by a different platform (e.g. ERS-1 for one scene, and ERS-2 for the other) or by satellite maneuvres between the particular dates of acquisition. In addition, two gyroscopes (out of three) have been broken since 2000 on ERS-2, causing the scenes acquired after to have a value of Doppler centroid largely different from the scenes acquired before, and therefore the images acquired before and after could not be processed together to form a single interferogram. (The maximum allowed Doppler centroid difference is generally believed to be 400 Hz – the bandwidth is close to 1400 Hz [17].)

As in the range direction, the azimuth spectras of both scenes should exactly overlap in order to maximize the interferogram coherence (for details about the influence of improper filtering to coherence, see [3]).

Chapter 6

Statistical Properties of a Resolution Cell

The resolution cell, i.e. the area from which the scattered signal is transformed into one image cell, contains many small scatteres. For ERS-1/2 SAR, the resolution cell is about 20-30 m long (in the range direction) and about 4.5 m wide (in the azimuth direction). Radar wavelength is $\lambda = 5.67$ cm, which is much shorter. In addition, the resolution cell is a little larger than the distance between the neighbouring pixel centers.

The actual phase values of resolution cells are not as important in SAR interferometry as the phase difference between neighbouring (and more distant) cells. This is the reason why the frequently used model of uncorrelated observations should not be used [17]. In addition, some error influences (imprecise satellite position, atmosphere) introduce errors in the phase – however, the error of the phase differences between neighbouring cells is much smaller, even negligible.

6.1 Observation as a Gaussian random variable

According to [17], the observation (i.e. pixel value) is a complex (circular) Gaussian random variable if the following conditions apply:

- none of the scatterers within the resolution cell dominates (i.e. none of the scatterers reflects more energy back to the SAR than other scatterers),
- the phase of individual scatterers has uniform distribution (which is fulfilled due to the fact that range resolution is much bigger than radar wavelength),
- the phase of individual scatterers is uncorrelated,
- the amplitude of individual scatterers is uncorrelated.

The probability density function (PDF) of a complex circular Gaussian random variable y is

$$pdf(y) = \frac{1}{2\pi\sigma^2} \exp\left(-\frac{(Re(y))^2 + (Im(y))^2}{2\sigma^2}\right) \tag{6.1}$$

where $\sigma^2 = \sigma^2_{Re(y)} = \sigma^2_{Im(y)}$.

Then, it can be derived [17] that the amplitude of the resolution cell has Rayleigh distribution and the phase has uniform distribution (however, this does not apply to a multilooked image). This means that the phase of a single image does not contain any information.

For SAR interferometry, the phase difference between two scenes (acquired at different times or from different places) is more important than the phase value itself. Reference [36] derives the interferogram phase distribution and the result is

$$pdf(\varphi_1, \varphi_2) = \frac{1-\gamma^2}{2\pi} \frac{1}{1-\gamma^2\cos^2(\delta\varphi)} \left(1 + \frac{\gamma\cos(\delta\varphi)\arccos\left(-\gamma\cos(\delta\varphi)\right)}{\sqrt{1-\gamma^2\cos^2(\delta\varphi)}}\right) \tag{6.2}$$

where γ is coherence (described in the following section), $\varphi_0 = \arg(\gamma)$ and $\delta\varphi = \varphi_1 - \varphi_2 - \varphi_0$. That means that the interferogram phase probability density function depends only on the phase difference and coherence, and is centered around the coherence argument. That means that in comparison to the scene phase, the interferogram phase contains information, and the reliability of the information depends on image properties, evaluated as coherence.

6.2 Coherence

Both pixels (of the master and slave scenes) can be considered to be circular Gaussian signals (y_1, y_2) and the joint PDF is

$$pdf(y_1, y_2) = \frac{1}{\pi^2 |C_y|} \exp\left(-\begin{bmatrix} y_1^* & y_2^* \end{bmatrix} C_y^{-1} \begin{bmatrix} y_1 \\ y_2 \end{bmatrix}\right) \tag{6.3}$$

where C_y is the complex covariance matrix and $|C_y|$ is its determinant [17] (* means complex conjugation),

$$C_y = E\left\{\begin{bmatrix} y_1 \\ y_2 \end{bmatrix} \begin{bmatrix} y_1^* & y_2^* \end{bmatrix}\right\} = \begin{bmatrix} E\{|y_1|^2\} & \gamma\sqrt{E\{|y_1|^2\}E\{|y_2|\}^2} \\ \gamma^*\sqrt{E\{|y_1|^2\}E\{|y_2|^2\}} & E\{|y_2|^2\} \end{bmatrix}, \tag{6.4}$$

$$|C_y| = E\{|y_1|^2\}E\{|y_2|^2\}(1-|\gamma|^2), \tag{6.5}$$

where γ is the complex coherence. The phase of γ is equal to the phase difference between y_1 and y_2, and therefore the interferogram phase, while its magnitude $|\gamma|$ is always in the interval $\langle 0, 1\rangle$ and corresponds to the stability of the scatterer, i.e. also to the stability (reliability) of the phase.

6.3 Practical approach

These formulas require the knowledge of the mean (or expectance) value of the observation, which is impossible. Regular statistics works with one variable observed many times. This is not possible in SAR interferometry – due to the SAR principle (described in Chapter 3) it is impossible to make multiple looks of the same area.

The area is imaged multiple times in order to allow deformation mapping – however, the temporal decorrelation (changes in the surface) and also the variability of the SAR center makes it impossible to make these observations comparable from the statistical point of view. Therefore, the complex covariance matrix and the coherence itself cannot be evaluated precisely and an approximate method is used, evaluating the dispersion of the complex signal within the particular cell neighbourhood.

Please note that in the following formula, coregistered scenes are used (i.e. the slave scene must be resampled first):

$$\gamma = \frac{\frac{1}{N}\sum_{i=0}^{N} M \cdot S^*}{\sqrt{\frac{1}{N}\sum_{i=0}^{N} M \cdot M^* \frac{1}{N}\sum_{i=0}^{N} S \cdot S^*}}, \tag{6.6}$$

where M, S are the complex values of a pixel in the master and slave images and N stands for the size of the window used for coherence computation. Unfortunately, the coherence estimation is biased for small number of looks (i.e. small window sizes for the previously-mentioned approximation) and small coherence values (see e.g. [18]); however, there is currently no other possibility to estimate the value better. Large estimation windows may cause coherent areas to get lost.

Thesis [36] now separates the derivation for Gaussian scatterers and for point scatterers. For Gaussian scatterers, the phase standard deviation may be written as

$$\sigma_{\delta\varphi}^2 = \int_{-\pi}^{\pi} \delta^2\varphi pdf(\delta\varphi) d\delta\varphi, \tag{6.7}$$

while for point scatterers, it is

$$\sigma_{\Delta\varphi,\gamma} = \frac{1}{\sqrt{2N}} \frac{\sqrt{1-\gamma^2}}{\gamma}. \tag{6.8}$$

However, this relation is biased – it applies only for very high coherence values. Please note that the phase standard deviation for point scatterers is always significantly lower than for Gaussian scatterers [36].

Reference [36] contains a graph showing the relation between coherence and interferogram phase standard deviation, where it can be seen that a coherence of 0.3 corresponds to a phase standard deviation of about 80 degrees (for distributed targets), but using (6.8), we get a phase standard deviation of about 16 degrees (for point targets).

Point scatterers usually have a high amplitude (i.e. intensity of the received signal) and are considered to have stable phase behaviour (will be dealt with in Chapter 10).

Chapter 7

Phase Unwrapping

In SAR interferometry, phase unwrapping is a key problem. It may be omitted only in special cases, such as deformation mapping in an area where the deformations are small – on the contrary, it may be difficult to detect them in this case.

On the other hand, phase unwrapping is the process which can produce the largest errors – their distribution is not normal because the errors may only be multiples of 2π. It is an ambiguous process and if two key conditions are not fulfilled, the correct solution, i.e. the one corresponding to reality, is not guaranteed to be found.

7.1 Problem definition

First, let us emphasize that we perform phase unwrapping in a 2D array. Some articles [6, 7] even mention phase unwrapping in a 3D array (the third dimension is time, using interferogram stack), but the methodology is not described there.

The problem is that phase is ambiguous: it is always in the $(-\pi, \pi)$ interval, independent on the actual elevation or deformation. Let us call this the *wrapped phase* (ψ). The actual (i.e. correct phase, corresponding to the real terrain or deformation) phase is denoted as ϕ and the *unwrapped phase* (i.e. the phase after the unwrapping process) as φ (although the phase refers to an interferogram, not the scene). The unwrapping criterium is therefore

$$\varphi = \arg\min \sum_{i=1,j=1}^{i=M,J=N} |\varphi(i,j) - \phi(i,j)|^p , \tag{7.1}$$

where i and j are the indices of the given array cell, N and M define the size of the array and the factor p indicates which norm to minimize.

However, criterium (7.1) is impossible to minimize due to the fact that the real phase ϕ is usually unknown. Therefore, another approach to the problem should be adopted. Let us define wrapped and unwrapped phase differences

$$\Delta_x^{\psi}(i,j) = \psi(i+1,j) - \psi(i,j) + 2k\pi, \tag{7.2}$$

$$\Delta_y^{\psi}(i,j) = \psi(i,j+1) - \psi(i,j) + 2k\pi, \tag{7.3}$$
$$\Delta_x^{\varphi}(i,j) = \varphi(i+1,j) - \varphi(i,j), \tag{7.4}$$
$$\Delta_y^{\varphi}(i,j) = \varphi(i,j+1) - \varphi(i,j), \tag{7.5}$$

where k is an integer guaranteeing that $\Delta_x^{\psi} \in (-\pi, \pi\rangle$ and $\Delta_y^{\psi} \in (-\pi, \pi\rangle$. Therefore, we can use a realizable criterium:

$$\varphi = \arg\min \sum_{i=1,j=1}^{i=M-1,j=N-1} \left| g_x(i,j)\left(\Delta_x^{\psi}(i,j) - \Delta_x^{\varphi}(i,j)\right) + g_y(i,j)\left(\Delta_y^{\psi}(i,j) - \Delta_y^{\varphi}(i,j)\right)\right|^p, \tag{7.6}$$

where $g_x(i,j)$ and $g_y(i,j)$ are the weights of the appropriate gradients.

However, minimization of such an L^p norm does not guarantee that the phase is unwrapped correctly; the norm itself depends on the weights selected. On the other hand, the fact that the phase is correctly unwrapped cannot be mathematically formulated or verified.

For topography phase, we expect that when going from one point to another using different paths, the other point will have the same height in all cases. The same applies to phase, i.e. if we come back to the starting point, we need to have zero phase change. We require the unwrapped phase to have this property.

According to [11], this condition means that the following equation applies:

$$\left(\Delta_x^{\varphi}(i,j) - \Delta_x^{\varphi}(i,j+1)\right) - \left(\Delta_y^{\varphi}(i,j) - \Delta_y^{\varphi}(i+1,j)\right) = 0 \tag{7.7}$$

for $i \in \langle 1, M-1\rangle$, $j \in \langle 1, N-1\rangle$.

This condition seems evident but it usually does not apply to the wrapped phase.

On the other hand, if equation (7.7) is fulfilled in all points, the phase unwrapping problem has a trivial solution. A reference point is selected and the unwrapped phase of a point is computed using the unwrapped phase of a neighbour and the phase difference, independently on the selected neighbour (*unwrapping path*).

In practice, equation (7.7) is based on two conditions:

- the real phase differences do not exceed π,
- the phase array does not contain noise.

In practice, these conditions are typically not fulfilled: the phase differences are large at steep slopes (in addition, the orientation with regard to SAR must be considered), and vegetated areas always contain noise.

If the wrapped phase does not fulfill equation (7.7) in all points, phase unwrapping is ambiguous, i.e. the unwrapped phase depends on the unwrapping path.

According to [11], *residue* is the point where condition (7.7) is not fulfilled. Its value may be 2π or -2π – the residue may be either positive or negative (we do not consider the theoretical case when it is $\pm 4\pi$). Let us generate *branch cuts*, connecting the same number of positive and negative residues. The branch cuts may also connect a residue with the array boundary (in this case, it is not neccessary for the branch cut to contain the same number of negative and positive residues; our problem is always spatially limited). If the unwrapping paths do not cross the branch cut, the unwrapped phase is unambigous. However, the ambiguity of the problem remains in the selection of the branch cuts.

7.2 Approaches

According to [11], there are two basic approaches to solve the problem:

- *path-following* algorithms,
- methods that minimize a certain norm.

Both methods may be applied with or without weights, weighing particular phase differences.

In SAR interferometry, coherence $\gamma = |\gamma_c|$ (6.6) is often used for weighing the particular phase differences.

There are some differences between path-following and norm-minimizing algorithms:

- While the path-following algorithms consider the properties of the neighbour of a particular point (i.e. only local properties of the phase array), the norm-minimizing methods are global, always considering the whole phase array.
- For path-following algorithms, the difference between the wrapped and unwrapped phase for all points is an integer multiple of 2π. This is not the case for the norm-minimizing algorithms, and after applying the method, an operation guaranteeing the fulfillment of this condition must be performed (*congruence operation*) – the phase is simply rounded to the closest "permitted" value. However, after that, the solution is no longer optimal.

7.3 Basic terminology of graph mathematics

Let us consider a *network* (directed graph) $\mathbf{G} = (\mathbf{N}, \mathbf{E})$, where $\mathbf{N}$ is a set of *nodes* and $\mathbf{E}$ is a set of *directed edges*. *Flow* f is defined in the network, where some nodes are *sources* ($S(n) > 0$), some are *sinks* ($S(n) < 0$) and the others are neutral. Each edge has a positive capacity $c(e)$ and positive weight $w(e)$. The flow must fulfill the following conditions:

- The capacity of an edge cannot be exceeded: $f(e) < c(e)$ for each $e \in \mathbf{E}$.

- The flow is conserved, i.e.

$$\sum f_+(n) - \sum f_-(n) + S(n) = 0 \text{ for all } n \in N, \tag{7.8}$$

  where $\sum f_+(n)$ is the flow coming to the node n (from all edges containing n), $\sum f_-(n)$ is the flow leaving the node n (to all edges containing n) and $S(n)$ is the strength of the source/sink node.

First of all, the sum of source strengths must be equal to the sum of sink strengths. If not – and this may easily be the case of SAR interferometry – the array borders may be defined as both sources and sinks.

As a conventional mathematical problem, only one source node and one sink node are present in the network. The problem of finding the minimal cost flow is then reduced to finding the shortest way in the graph which is resolved using the Dijkstra's algorithm; if the capacities are too low to absorb the required flow, another "shortest" way in the graph is looked for for the remaining flow.

However, this is not the case of interferograms. Here, all sources and sinks have a unique strength (strength of 2 is only a theoretical case) but are distributed within the whole graph. On the other hand, the capacities are not neccessary to be defined here which reduces the problem complexity. However, the capacities (when defined) can limit the maximum flow in each edge of the network – and also allow the limit to be different for each direction [5] (each phase difference is represented by two directed edges – one in each direction – because the flow is only allowed to be positive).

The interferometric problem also has one more constraint: the flow must be integer (only integer multiplies of 2π can be added to each phase difference).

However, as will be explained later, we are looking for a flow with minimum cost. Let us note here that a solution with the shortest branch-cut length does not need to be optimal in any way – the branch cut only prevents the unwrapping path to cross it, but the flow in the corresponding edge may be zero, i.e. the phase difference need not be adjusted.

7.4 The minimum cost flow algorithm

Let us remind that each edge has also a positive weight $w(e)$, and the total cost of the flow in the network is defined as

$$C = \sum_{e \in \mathbf{E}} f(e) \cdot w(e), \tag{7.9}$$

with both the previously mentioned conditions fulfilled.

The aim of the minimum cost flow algorithm is to minimize C.

The particular steps of the method are not described here and are subject of the graph mathematics.

7.5 L^1 or L^0 norm?

Obviously, the phase differences must be adjusted somewhere in order to get a residue-free interferogram. Also, the adjustments have to be minimal in some way – and therefore all adjustments are penalized. However, the question is, should the penalty be proportional to the adjustment itself?

Let us deal now with the value of p in expression (7.6). For $p = 2$, the minimization task corresponds to the classical least-squares problem that can be dealt with efficiently by non-iterative methods. However, the least-squares solution reduces the number of large adjustments and causes the adjusted phase differences to be spread throughout the phase array [5]. The L^2 norm is generally viewed as unsuitable for SAR interferometry.

If the penalty is proportional to the phase difference change, we call it minimizing the L^1 norm ($p = 1$) – the total sum

$$\sum_{e \in \mathbf{E}} |d(e)| \cdot w(e), \tag{7.10}$$

where d is the adjustment size, is minimized. The advantage of the method is that large adjustments are largely penalized, and therefore there remains only a small probability that a phase difference is adjusted largely.

The other approach uses L^0 norm, i.e. minimizing the number of adjustments, irrespective of the size of the adjustments. The expression

$$\sum_{e \in \mathbf{E}} d_{thr}(e) \cdot w(e) \tag{7.11}$$

is minimized, where d_{thr} is zero if $d = 0$ and otherwise it is 1. This criterium is said to be better (i.e. better corresponding to the reality) for SAR interferometry [11].

In terms of the network (as introduced above), the problem of L^1 norm is solved efficiently by the minimal cost-flow (MCF) algorithm – the weights are constant for this case. However, the problem of L^0 norm requires the weights to be dependent on the actual flow through the edge, i.e. the problem is highly non-linear and NP-hard (the proof is disclosed in [4]). NP-hard problems are problems which are exponentially difficult to solve – cannot be solved in a polynomial time. However, the cited article suggests an algorithm finding an approximate solution.

7.6 The method used

Phase unwrapping is performed by the `UNWRAP` batch which is a part of the GAMMA software. According to [42], phase unwrapping is performed by the minimum cost flow method with some adjustments, which are discussed below. Generally, the path-following algorithms appear to give more reliable results for SAR interferometry.

According to [42], let us consider that a four-pixel cell (used for residue assessment) is a node. Source nodes are defined as positive residues and sink nodes are defined as negative residues. Between two neighbouring nodes, there are two directed edges (because the flow may be only positive).

The weights are given as the coherence of each pixel, and pixels with a very low coherence (the threshold is to be user-adjusted) are even excluded from the unwrapping process, i.e. no node nor edge is created at its place.

Then, the minimum cost flow is found for the given evaluated graph. The edges are associated with the phase differences between neighbouring pixels, and a non-zero flow in each edge indicates that the difference should be adjusted by $2k\pi$, where k is the flow (may be different that ± 1).

Pixels with coherence lower than a predefined threshold are excluded from the unwrapping, and therefore the graph must be adjusted. This is done using Delaunay triangulation (definition taken from [43]): "the Delaunay triangulation or Delone triangularization for a set P of points in the plane is the triangulation DT(P) of P such that no point in P is inside the circumcircle of any triangle in DT(P). Delaunay triangulations maximize the minimum angle of all the angles of the triangles in the triangulation; they tend to avoid 'sliver' triangles."

The triangulation also (according to [42]) doubles the number of edges – causing that the network is more dense and allows for better localization of residues.

The fact that some pixels are excluded from the unwrapping process may cause some areas to be separated from the rest of the scene, and therefore introduce large unwrapping errors; on the other hand, the results are more reliable than if the coherence threshold is set too low and more incoherent areas are unwrapped.

In addition, large areas with "no phase" may be present in the unwrapped scene. This depends on the selection of the unwrapping seed (i.e. the pixel where unwrapping starts) – all the continuous area containing the seed is unwrapped, irrespective of its size.

Chapter 8

Models

8.1 Model definition

Let us denote observations, i.e. the measured interferogram phase for each pixel, as $\Delta\varphi$ and the unknowns, such as elevation, deformations etc. for each pixel, as x. Then the linear Gauss-Markoff model [17] may be applied as

$$\mathcal{E}\{\Delta\varphi\} = A \cdot x, \tag{8.1}$$

$$\mathcal{D}\{\Delta\varphi\} = Q_{\Delta\varphi} \tag{8.2}$$

where A is the design matrix and $Q_{\Delta\varphi}$ is positive-definitive covariance matrix of the interferogram phases.

Let us emphasize here, that this model applies independently to each pixel of the processed scene crop and the number of unknowns depends on the task formulation.

In order to solve the model, the number of unknowns must be equal or smaller than the number of observations. Then, the most probable vector of unknowns and its covariance matrix may be evaluated as

$$\hat{x} = (A^T Q_{\Delta\varphi}^{-1} A)^{-1} A^T Q_{\Delta\varphi}^{-1} \Delta\varphi, \tag{8.3}$$

$$Q_{\hat{x}} = (A^T Q_{\Delta\varphi}^{-1} A)^{-1}. \tag{8.4}$$

The model may be used in several variations: the observations may or may not include the flat-Earth phase or topographic signal. In addition, the phase is due to the complex nature of the received signal known only modulo 2π which makes the problem more complex and nonlinear.

The unknowns include the topographic height, geophysical deformation, atmospheric delay during the acquisition of both scenes, and the integer ambiguity number (possible unwrapping error).

However, as equations (8.1) and (8.2) apply for each interferogram pixel, the number of unknows is always larger than the number of observations. Ramon Hanssen in [17] cites three strategies for the problem solution:

- *more observations can be added to the model,*
- *apriori information can be introduced,*
- *the model can be reformulated.*

In the radar interferometry, the only possibility to add more observations to the model is to use more scenes, corresponding to a larger number of overflights, generating new deformations, new atmospheric delays, and new phase unwrapping ambiguities. Due to the processing method, it is also impossible to acquire two scenes of the same area during an overflight. Therefore, the number of unknowns is larger too – the only improvement may be seen in the topography signal, which stays all the same.

Introducing apriori information means e.g. using known topographic height of each pixel for subtracting the phase corresponding to the height (or neglecting the topography phase due to a flat terrain or small perpendicular baseline). Or, the processed area can be assumed to be geophysically stable, therefore no deformations are expected, or the phase unwrapping can be assumed to be perfect.

Reformulating the model means e.g. neglecting some parameters and transferring them into the stochastic part of the model (this is often the case of the atmospheric delay).

8.2 Interferometric stacks for deformation monitoring

Let us overview the interferometric stacks. There are N scenes of the same area and a DEM is available, obtained from a different source. Let us assume that the phase unwrapping was performed perfectly, i.e. the unwrapped phase corresponds to the reality. In addition, let us neglect the atmospheric delay and orbit error influence which may appear as the phase trend in some of the interferograms.

All $N(N-1)$ interferograms are created, i.e. each scene is combined with each other. However, some interferograms may be omitted due to a low coherence and some points in some interferograms may be omitted in the consistency check step (see Chapter 13), causing the number of observations to be different for each interferogram pixel.

The observations are the phases of each interferogram, with the flat-Earth and DEM phase subtracted. However, both processes use only orbit information of the master scene and baseline information, so they are deterministic and do not influence the stochastic part of the model). The phase to be adjusted is also unwrapped and unwrapping errors should be found and corrected before the adjustment itself (or are corrected iteratively), so unwrapping errors are not considered in the basic adjustment model.

In the literature dealing with interferometric stacks, there are basically two models for deformation adjustments:

- *deformation model*, where the deformations in the times of acquisitions are searched for,

- *velocity model*, where the velocities between individual times of acquisition are searched for.

Properties of both approaches are discussed in the following sections.

8.3 Pseudoinverse

Pseudoinverse is a method for inverting a non-regular matrix. For a regular matrix, the result of pseudoinverse is the same as the result of inverse.

If a system of equations

$$A \cdot x = b, \tag{8.5}$$

is to be solved, the solution for regular A is

$$x = A^{-1}b. \tag{8.6}$$

However, A is not always regular. The system of equations may be

- overdetermined, i.e. there are more equations than unknowns, the exact solution generally does not exist; the problem is then reformulated by minimizing the quadratic norm of $b - Ax$ and formula (8.3) is used for computation of x;
- underdetermined, i.e. there are more unknowns than equations, and the system of equation has an infinite number of solutions. In this case, pseudoinverse is computed by the Singular Value Decomposition (SVD) technique (in MATLAB) and the solution with minimal quadratic norm of x is selected. Unfortunately, the SVD technique does not allow weighting the values of x.

However, the case of InSAR often brings problems, that are both overdetermined and underdetermined. If there is a scene within the set that is contained in no interferogram, or if the interferograms divide the set of scenes into more subsets, there are many interferograms to determine the main set (i.e. that one containing the reference scene) and also to determine the other sets, but there is no information to interconnect these subsets – in this view, the system of equations is underdetermined. This is the problem often encountered in the deformation model (see the next chapter).

8.4 Deformation model

Here, the unknowns are defined as deformations Φ in each acquisition time t_i where i is the scene number (with regard to one of the scenes where the deformations are assumed to be zero). An auxiliary matrix A_{aux} has N columns (one for each scene) and M rows (one for each existing interferogram for a particular pixel) and contains -1 if the corresponding scene is the master of the interferogram, and 1 if it is the slave (please note that A_{aux} may be different for each pixel). Then, the design matrix A may be written as

$$A = \frac{4\pi}{\lambda} \cdot A_{aux}. \tag{8.7}$$

Before the processing itself, matrix A needs to be regularized, which may be performed by eliminating the column corresponding to a reference (master) scene (selected before processing), in which acquisition time the deformations are considered to be zero. However, it may happen that during the consistency check step (described in Chapter 13) all interferograms containing the reference scene are excluded (for a point) – in this case, no adjustment can be performed.

This deformation model (used in [37]) does not need any assumptions of the deformation linearity in time. In addition, it does not assess DEM errors but these may be added to the model (see section 8.8). Atmospheric influence is said [37] to be partially eliminated in the adjustment; however, we suppose that the atmospheric influence is not eliminated at all and it is a part of the results – if the deformations are attributed to individual acquisition times, so are the atmospheric delays. Partial elimination is possible only if the deformation curves are then low-pass filtered.

Due to a large number and structure of unknows, there may be a problem of the regularity of the matrix A^TA. During the interferogram consistency check steps, some interferograms may be excluded from the adjustment, causing that some columns of the A matrix may be empty or there are more independent sets of scenes, which are not interconnected by any interferogram. In both of these cases, the matrix A^TA is singular and there are two ways of solving it:

- excluding the empty columns from the matrix A, eventually separating the independent sets of interferograms into more matrices and independent adjusting; however, some elements of the vector $\Delta\varphi$ are missing in the case of exclusion and the independent sets of vector Φ, computed by separate adjustments, cannot be interconnected in any way without a priori information (e.g. from neighbouring pixels or by temporal interpolation).
- using the pseudoinverse (described in section 8.3). A disadvantage of this method is that the results may be inconsistent with the physical reality (due to the minimization as described in section 8.3), as noted in [2], where the pseudoinverse with the changing-velocity model (see section 8.7) is recommended. The deformations in the separated sets that do not contain the reference scene are minimized in the deformation model – without respect to the other deformations, causing large jumps in the deformations.

8.5 Constant-velocity model

The constant-velocity model assumes that the deformations are linear in time, respectively the deformations may be represented by an explicit function of which the parameters are searched for.

Here, there is only one unknown (independently for each processed point): the deformation velocity v.

Let us define vector $dt = A_{aux} \cdot t$ (the auxiliary matrix A_{aux} is the same as for the deformation model) where t is the vector of acquisition times (in days, e.g.). The vector dt therefore contains temporal baselines of each interferogram.

The constant-velocity model can be expressed in the following way:

$$\Delta\varphi = \frac{4\pi}{\lambda} dt \cdot v + \delta\varphi, \tag{8.8}$$

where $\delta\varphi$ is again the phase noise to be minimized by the least-squares adjustment.

If expression (8.8) is rewritten to the matrix notation, the design matrix has the form of

$$A = \frac{4\pi}{\lambda} \cdot dt. \tag{8.9}$$

A great advantage of this model is that there is only one unknown (if the velocity is also expressed by few parameters, there are more, but significantly less than for the deformation model) and therefore there are no problems with singularity. However, the problem is that the parametric expression of the deformations may be unknown in advance and that the assumption of constant velocity need not be always satisfied.

This model is used in the Permanent Scatterers technique, overviewed in chapter 10.

8.6 Seasonal-velocity model

Article [22] mentions the way to model seasonal influences within the constant-velocity model (as described in the previous section). This is performed by adding two parameters and the constant velocity is substituted by

$$v = v_0 + v_A \sin \frac{2\pi}{T}(t - t_0) = v_0 + v_{A1} \sin \frac{2\pi}{T} t + v_{A2} \sin \frac{2\pi}{T} t, \tag{8.10}$$

where v_0 is the constant (i.e. season-independent) velocity component, v_A is the amplitude factor of the velocity, T is the season length (usually one year), t is the time of acquisition, t_0 is the temporal shift of the seasonal influence. Please note that in the first part of the equations, unknowns are v_0, v_A and t_0 – the second part of the equations serves for the computations (it is linear in unknowns) and the unknowns are v_0, v_{A1} and v_{A2} here. The adjustment is similar to the velocity model except for the fact that the number of unknowns is higher.

8.7 Changing-velocity model

This model is described in [2] in detail and its number of unknowns is the same as for the deformation model. It is not the deformation velocity to be looked for, but the deformations themselves – however, the velocity nature allows for avoiding some problems of the deformation model and preserving the physical meaning of the results at the same time.

One of the main disadvantages of the deformation model is that the interferogram set may be separated into two or more subsets – which are interconnected by no scene. In this case, the deformation modeling leads into situation where $A^T A$ is singular, and therefore irreversible.

Article [2] suggests to do it another way. $A^T A$ is singular, but its inversion to the rank (which is the number of scenes used) may be obtained by pseudoinverse (see section 8.3). However, it notes that results obtained by this technique do not always correspond to the physical reality, being minimal in a wrong way.

They suggest to estimate velocities – velocities different for each time interval between two acquisitions. Now, the formulation of the design matrix A is not as trivial as in previous cases,

$$v_i = \frac{\Phi_i - \Phi_{i-1}}{t_i - t_{i-1}} \tag{8.11}$$

with $\Phi_0 = 0$ and $t_0 = 0$ (we select the reference scene as the first one in time, although it is not the optimal solution with regard to the standard deviations), and therefore

$$\Delta\varphi_j = \sum_{i=1}^{j} v_i (t_i - t_{i-1}) + \delta\varphi \tag{8.12}$$

for all time intervals considered (depends on the master and slave scenes for the particular interferogram). Therefore, design matrix A then contains time intervals $t_i - t_{i-1}$ in the appropriate places (velocities v_i are to be estimated).

Now, the minimum-norm of the pseudoinverse (see section 8.3) is not applied to the deformations, but to the velocities (which are not contained in the subset containing the reference scene), and the deformations (obtained after integration of the velocities) do not contain large discontinuities [2]. That also means that the model formulation is different from that defined by (8.14), i.e. not the deformation residues are to be minimized, but the velocity residues. The deformations (together with their standard deviations) are computed after adjustment itself by integration, and that means the standard deviation grows up when reaching further and further away from the reference scene. The SVD technique (used for pseudoinverse) also provides no weights, so that a unique covariance matrix is used.

In practice, let us imagine that design matrix A is block-diagonal, i.e. all scenes are processed into interferograms, but there are separate sets of them. Then, the system of equations is both overdetermined (if the number of interferograms is high enough) and underdetermined – there are few scenes which cannot be determined in any way (one for each of the block; minus the reference one). Let us imagine that each block will be adjusted separately with its own reference scene – and the results of each block will be shifted (together with its reference scene) to give the minimum quadratic norm.

However, the minimum norm is applied to the velocities, not to the deformations themselves: i.e. if a velocity cannot be determined by the adjustment, it is said to be as small as possible to fulfill the other conditions. That means that the deformations which cannot be determined by the adjustment will "get lost" among the other ones.

A disadvantage of this method is that due to the integral nature of the deformations, the standard deviation of the last deformation is significantly worse than those of the first deformations (in time).

Article [2] suggests to correct the data first for the DEM error and atmospheric influence, then perform phase unwrapping again and then the adjustment. However, this is not the way we do that, and the atmospheric delay stays in the interferograms which may negatively influence the "minimal" velocities. In other words, if the deformations were discontinuous in time (and continuous in space), we would say that this is caused by atmospheric delay. However, if some deformations are estimated on the basis of velocities, they may be significantly influenced by atmospheric delays during the other passes.

8.8 DEM error estimation

Another unknown, often estimated within the model, is the DEM error, i.e. the difference between the external DEM used for topography subtraction and the DEM contained in the interferograms. The principle is that topography contained in an interferogram depends strongly on its perpendicular baseline – and therefore the DEM error is transferred into each interferogram with a different (known) factor.

The number of degrees of freedom (i.e. the difference between the number of measurements and the number of unknowns) is usually high enough to allow one more unknown (though different for each pixel).

The equations only get one more parameter (and the design matrix therefore gets one more column)

$$\delta\Delta\varphi = \frac{4\pi}{\lambda}\frac{B}{r\sin\Theta}\cdot\Delta z, \tag{8.13}$$

where $\delta\Delta\varphi$ stands for the interferogram phase (or its residue) change due to the DEM error, B is the perpendicular baseline (please note that it is not different only for each interferogram, but also for each pixel, it changes in both azimuth and range directions), Θ is the look angle and r is the distance between the master satellite and the scattering object (both changing slightly in the range direction), and Δz is the DEM error to be estimated.

It may seem that for small baselines (100-200 m), the DEM error should not significantly influence the interferometric phase; however, it is worth subtraction [2] – the precision of the estimated deformations is getting better.

8.9 Adjustment with phase unwrapping errors

However, phase unwrapping cannot be considered perfect at all in our case, where the interferograms are mostly incoherent and separate patches are processed – this fact is also confirmed by our experience. The general adjustment may be then formulated as

$$\hat{x} = \arg\min r^T Q^{-1} r, \tag{8.14}$$

where r is the vector of adjustment residues

$$r = u - A \cdot \hat{x}, \tag{8.15}$$

(each of the previously defined models can be substituted), Q is the covariance matrix (to be dealt with in the following section), and x is the vector of unknowns (also, all of the previously defined models can be substituted). Variables with ˆ are the estimations of the unknowns.

Here, u are the "correct" phase values, therefore

$$u = \Delta\varphi + 2k\pi, \tag{8.16}$$

where k are integer unwrapping errors.

In addition, the following relations must be fulfilled [36, 37]:

$$\Delta\varphi_{AB} + \Delta\varphi_{BA} = 0, \tag{8.17}$$

$$\Delta\varphi_{AB} + \Delta\varphi_{CA} + \Delta\varphi_{BC} = 0, \tag{8.18}$$

where the first index applies to the master scene and the other to the slave scene and $\Delta\varphi$ may be either the original phase (without flat-Earth subtraction), or the (whatever subtracted) phase referenced to a certain point, or the unwrapped phase referenced to the certain point.

These formulas may be rewritten in matrix form as

$$C \cdot u = 0, \tag{8.19}$$

where C is known (all interferograms doubles and triples are contained).

The problem therefore has measurements l, parameters Q, C, A and unknowns x, k.

As a whole, the minimization problem may be rewritten from (8.14) to

$$\hat{x}, \hat{k} = \arg\min (l + 2k\pi - Ax)^T Q^{-1} (l + 2k\pi - Ax) \tag{8.20}$$

with

$$C \cdot (l + 2\hat{k}\pi) = 0. \tag{8.21}$$

However, as it looks as a simple minimization problem with a condition, it is not. It is caused by the fact that the k vector must be integer. If it did not have to, the problem would be easy to solve and ambiguous. However, the requirement for integer k makes the problem nonlinear, directly unsolvable [22], and neccessary to be solved iteratively, with the danger of getting stuck in a local minima.

A theoretically easy approach would be to try out all possible k vectors (the number of them is only countable and only small values of k (less than about 50) come into consideration. However, with the number of interferograms about 100, this gets 100^{101} different k vectors, for which the adjustment must be performed – and all this for each pixel of the crop!

Article [22] suggests to use the LAMBDA method (designed for GPS) for ambiguity resolution for Permanent Scatterers processing (described in Chapter 10). As Permanent Scatterers (PS) processing has many features common with stack interferometric processing, it is not the same. They advice not to search the space of unknowns, but to search the space of unwrapping ambiguities/errors, which is guaranteed to give an exact solution if the whole space has been searched [22].

However, the authors admit that in some conditions, the search can take a very long time and they limit it to a certain number of iterations, which may cause that an acceptable solution is not found. Please note that in the case of ambiguity resolution (for InSAR), no approximate solution should be accepted – due to the fact that the one-point difference (due to the integer nature of the ambiguities) makes a difference of 2.8 cm in deformations.

Our approach also uses search in the ambiguity space and is described in detail in section 13.7.

8.10 Stochastic part of the model

8.10.1 Phase accuracy

The inaccuracies influencing image acquisition and interferometric processing are described in Chapter 9. Chapter 6 describes how an approximate measure of phase reliability (standard deviation) may be obtained from image properties.

As mentioned in [14, 16], the interferogram phase value itself does not have a significant meaning due to the fact that the atmospheric delay may account for even five phase cycles. On the other hand, the atmospheric delay is expected to be continuous in space, i.e. the difference between two cells in an interferogram is expected to contain the significant information.

With respect to it, the interferogram phase to be adjusted is referenced to a certain point (the point is recommended to be stable and required to be coherent in as many interferograms as possible; for other details, see section 13.4).

However, if an interferogram phase has a standard deviation of $\sigma_{\Delta\varphi}$ (e.g. evaluated using formula (6.8)), the standard deviation of the referenced interferogram phase is then

$$\sigma_{\Delta\varphi,\gamma,ref} = \sqrt{2}\sigma_{\Delta\varphi} \tag{8.22}$$

assuming that the point to be referenced and the stable point both have the same phase accuracy. Usually, this is not the case but for simplicity, let us use this formula.

Using formula (6.8), for coherence 0.3, we get interferogram phase standard deviation of 25.8°. As described in Chapter 6, this estimation is biased, and therefore the true standard deviation is even higher. Let us note here that this accuracy measure is attributed only to coherence, reso. decorrelation.

Therefore, applying formula (8.22), we get that the referenced phase standard deviation is 36.4° at maximum (resp. its part attributed to decorrelation).

8.10.2 Covariance matrix

Let us assume that the observations, i.e. the phases of the scenes, are independent (this is not absolutely true because the resolution cells partially overlap and all points are referenced to a single one). Then, the covariance matrices for the unknowns may be expressed (for all models) using formula (8.4).

The adjustment is performed independently for each point of the scene, and therefore the scene phases are really independent within this adjustment.

However, the problem is not as trivial as it may seem. This is due to the fact that the "observations", i.e. the phase of the scenes, which are independent, are not known accurately enough (see Chapter 6), and are therefore the unknowns. For the real observations, i.e. the interferogram phases, the accuracy may be evaluated (see Chapter 6), however, their independence is questionable (although the scene phase has a uniform distribution) due to the fact that various interferograms may contain one scene in common.

References [36, 37, 2] do not consider different interferogram phase variances at all, the covariance matrix is unitary. We first tried to construct the covariance matrix in such way that it corresponds to the accuracy of particular interferograms (for each point), but finally we decided to use the unitary matrix too. The reasons are following:

- standard deviation of an interferogram phase, computed by (6.8), takes in account only the coherence, i.e. the rate of decorrelation;
- as discussed in this chapter, unwrapping errors cannot be involved in the covariance matrix at all due to the fact they are unknown before adjustment;
- as will be discussed later, the referencing errors are also significant;
- Kolmogorov-Smirnov test (described in section 13.9) tests if the adjustment residues are normally distributed and does not take into account their weights.

Chapter 9

Error Influences in SAR Interferometry

According to Chapter 2, the following factors may influence the accuracy of SAR interferometry results:

- during acquisition:
  - thermal noise,
  - decorrelation (i.e. a change in acquistion conditions),
  - atmospheric delay,
  - satellite clock instability,
- during processing:
  - satellite position errors,
  - DEM errors,
  - errors in phase unwrapping.

The influence of individual factors will be dealt with in the following text.

9.1 Satellite position errors

Satellite position is a very important factor for radar interferometry precision. Even a few-centimeter error may cause the interferogram phase to be errorneous by more than a radian.

Satellite position is computed during flight, and this information is contained in the received radar data. However, this position may be errorneous by few meters in each direction. In addition, satellite position is computed by ESA and by DEOS [27] later, using the later-acquired data, and the resulting satellite positions are much more accurate than those of the real-time systems. However, these positions are available several months after the date of acquisition and are not available for all the period of satellite life, usually due to some problems onboard.

The methods to achieve satellite positions are in detail discussed in [41], including their accuracy. Let us only recapitulate here that the position error may be split into radial, across-track and along-track component, the radial standard deviation is about 5–6 cm for precise orbits, across-track standard deviation is about 15 cm for precise orbits, and the along-track error is not available, but it is known to be the highest. The along-track error may be substituted by timing errors [40] – on the other hand, usually it does not influence the data so significantly as noticed in the cited article (the large timing error was probably caused by an improper SAR processing in that case).

Although the particular satellite orbit errors have a random character, they influence the interferogram as a whole, so the errors may be estimated and corrected if large enough. The method is described in [25], and although criticized in [17], it is correct, as derived in [41]. The errors appear as fringes throughout the interferogram, the smaller the errors, the smaller fringe frequency. The correction is possible only for large errors (not for precise orbits) because a small fringe frequency is impossible to manually estimate. Phase trend in interferograms may also be estimated computatively by a sophisticated method – this is used in the PS processing (as described in Chapter 10).

The orbit errors influence the interferogram in two processing steps:

- during flat-Earth phase subtraction, where the residual phase may be expressed as (as derived in [41])

$$d(\Delta\varphi_E) = \frac{4\pi}{\lambda}\left(dB_h \sin\Theta - dB_v \cos\Theta\right), \tag{9.1}$$

  where dB_h and dB_v are the orbit errors in the horizontal and vertical directions respectively (see figure 9.1);

- and during topography subtraction, where the residual phase is expressed as (derived in [41])

$$d(\Delta\varphi_{tpg}) = \frac{4\pi}{\lambda}\frac{1}{\sin(\Theta+\varepsilon)R_M}\left(dB_h \cos\Theta h + dB_v \sin\Theta h\right), \tag{9.2}$$

  where h is the elevation.

Both equations (9.1) and (9.2) contain a sinus or cosinus of the look angle Θ, which is different for different range — meaning that the residual phase is slowly changing in the range direction. The fringes may also appear in the azimuth direction – this is caused by a change in the orbit error during the scene acquisition and the number of azimuth fringes is usually far lower due to the fact that the orbit errors are considered not to change quickly.

As mentioned in Chapter 2, the topography phase may be also subtracted by the 3-pass method: this is discussed in detail in [41] and [40] and will not be discussed here.

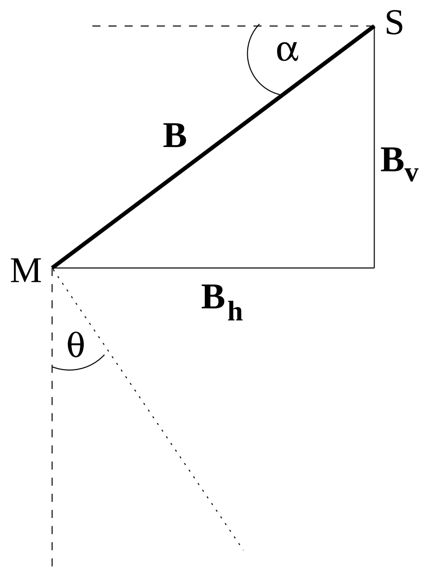

Figure 9.1: Baseline representation: M is the master satellite, S is the slave satellite, B_h is the horizontal component of the baseline B, and B_v is its vertical component. In this case, the parallel baseline $B_{\|}$ is zero and perpendicular baseline $B_{\perp} = B$ (due to the fact that look angle Θ is the same as the orientation angle α)

.

9.2 DEM errors

The effect of the DEM errors is also derived in [41] and has the following character:

$$d(\Delta\varphi_{DEM}) = \frac{4\pi}{\lambda}\frac{1}{\sin(\Theta+\varepsilon)R_M}B_{\perp}dh, \tag{9.3}$$

where dh is the DEM error for a particular interferogram pixel. The DEM errors vary for each interferogram pixel and cannot be a priori estimated. Their estimation may be contained in the adjustment process (see section 8.8).

9.3 Phase unwrapping errors

Phase unwrapping errors are probably the biggest problem in InSAR applications. The phase unwrapping process is ambiguous in incoherent areas or due to the radar geometry deformations, such as foreshortening or layover, and a "correct" (i.e. corresponding to reality) estimation of the phase ambiguity is not easy, often even not possible.

The complexity of the phase unwrapping process grows with the number of fringes in the interferogram – therefore it is more difficult to unwrap an interferogram containing the topographic signal, than an interferogram with the topography already subtracted. We unwrap the interferograms without topography, but the phase unwrapping errors also occur and they are very large in some cases.

The phase unwrapping errors are the only which do not have the normal distribution – their value is $\pm 2k\pi$, where k is an integer. Although they cannot be estimated during the unwrapping process itself, they can be estimated during postprocessing, if more interferograms are available (see Chapter 13).

9.4 Atmosphere

SAR processing uses the vacuum speed of light for derivation of phase φ using the two-way travel time, which contains a bias due to the non-vacuum atmosphere. However, this is not the problem due to the differential basis of InSAR. On the other hand, atmospheric properties (humidity, pressure etc.) may be different during the two acquisitions, causing a nontrivial phase bias of the interferogram.

The two atmospheric layers where the most significant atmospheric delay may originate are

- ionosphere (the uppest atmospheric layer), due to a different electron density (dependent on the local hour, latitude, solar activiy and geomagnetic conditions of the ionosphere [34], all of which factors change very slowly in the spatial dimension). The inospheric delay is dependent on the frequency of the signal – and was observed up to 2.8 cm for the C-band radar (which is carried by ERS-1/2) [15]. The signal extension is mostly larger than 30 km [15], allowing for low-pass spatial filtering of the inospheric contribution. The other problematic layer is
- troposphere (first 50 km from the ground, where the refractive index depends on local temperature, humidity and pressure [34]). The cloud-forming processes proceed in this layer, causing the delay to be spatially variable [15]. However, the variability is expected to be (at least partially) correlated with the topographic height [15]. The correlation is a theme of a current diploma thesis.

The tropospheric delay therefore is expected to be correlated with the topographic height and may be partially estimated (and corrected) within the DEM error. The ionospheric delay is compensated for by the procedure of referencing the phase with respect to a certain pixel. Article [2] recommends to extract the atmospheric contribution by low-pass filtering in the spatial dimension and high-pass filtering in the temporal dimension (with the purpose of distinguishing the deformation – however, the temporal sampling of the data with respect to the deformation rate must be dense enough for this method).

9.5 Satellite clock instability

Satellite clock instability may cause the following:

- the error in PRF (see section 3.5),
- the error in range decompression (see section 3.4),

- errorneous orbits (see section 9.1).

It is impossible to correct for the clock instability, and therefore the satellites are designed to have the clock instability as small as possible. However, I was unable to find the designed clock instability frequency for ERS-1/2.

9.6 Error budget

Let us suppose here that both atmospheric and orbit influence are stable within the interferogram crop, i.e. that the values of the influence change only slowly, or not at all. Then, the phase value itself does not contain the required information, but a phase difference between two cells does [14]. That is why all interferograms are referenced to a certain point (see section 13.4).

According to relation (6.8), an approximate standard deviation of the interferogram phase may be evaluated using coherence. However, the standard deviation evaluated using this relation does not contain the influence of imprecise orbits and DEM errors. In addition, the limited use of the relation (6.8) is described in section 6.3.

On the other hand, atmospheric delay influences the received phase in the same way as the Earth-crust deformations: both are given only by the acquisition dates. This is different in comparison to e.g. DEM error, which influences the phase with regard to the perpendicular baseline. Therefore, we decided not to separate the deformations and atmospheric delay during adjustment, hoping that the atmospheric influence will not be significant due to the small area processed. In addition, small atmospheric disturabnces may be (high-pass) filtered in the deformation development graph.

Chapter 10

Permanent Scatterers

Permanent Scatterers, or Persistent Scatters, etc. is a relatively new method of deformation monitoring with SAR interferometry technique.

In comparison to classical interferometric processing, this method makes use of point reflectors, i.e. not Gaussian scatterers, as described in section 6.1. The phase of the point reflectors does not depend so much on the incidence angle, and therefore the maximum allowed perpendicular baseline is much larger (about 1 km), which allows to make use of many more scenes (tens or even hundreds).

A detailed description of the basics of the method (during time, the method has been successively improved) can be found in [9] which is also source of the following short review.

The possibility to use many scenes, together with the point nature of the reflectors, allows to reach much better accuracy than for the classical InSAR processing, even deformations in the range of milimeters. However, complex knowledge of statistics and signal processing is required.

The basic requirement of the method is that the processed area contains enough permanent scatterers. The point scatterers are usually quite dense in urban areas, while quite rare in agricultural areas, and almost none in forested areas. They can be formed by buildings, bridges etc. A density of about 100 permanent scatteres per km^2 is required [9].

The number of permanent scatterers may be also increased using artificial reflectors placed to the investigated site. However, this is expensive and requires a special processing [24].

In addition to deformation mapping, the method also allows to evaluate DEM error in each point – the principle is similar to that described in section 8.8.

10.1 Processing steps

1. First, permanent scatterer candidates (PSc) are found in the scene. Magnitude dispersion within all scenes is computed for each scene pixel. If this dispersion is smaller than a threshold, the pixel is declared to be a PSc.

However, the magnitude of each scene must be first radiometrically corrected in order to be comparable. The calibration factor κ may be found in [23].

2. A master scene is selected and the interferograms are computed (i.e. the number of interferograms is $n-1$ if n is the number of scenes).

3. The flat-Earth phase and the topographic phase are subtracted from the interferograms (the DEM used for topographic subtraction need not be very accurate).

4. The phase difference of each point may be written as [9]

$$\Delta\varphi = a + p_x \cdot x + p_y \cdot y + B_\perp \cdot z + T \cdot v + e, \tag{10.1}$$

where a is a constant (for an interferogram), x, y are SAR coordinates (azimuth and range), $B_\perp$ is the perpendicular baseline (for an interferogram; computed separately for each point for higher accuracy), T is the temporal baseline (for an interferogram) and e is the noise. The rest of parameters are unknowns: p_x, p_y define the phase plane which represents atmospheric delay and orbit errors (assumed to be small enough to be represented by a plane; i.e. suitable only for small crops), z is the DEM error to be estimated and v is the deformation velocity (also to be estimated; assumed to be constant over time).

Four unknowns for each point is too many to be estimated; however, the p_x and p_y unknowns are constant within an interferogram, and z and v are constant for each point within the stack.

The problem is then viewed in two ways:

- the x-y plane within each interferogram (spatial dimension), which needs to be estimated, and
- the $B_\perp$-T plane within the stack (baseline-temporal dimension), which needs to be estimated too. This requires both $B_\perp$ and T to be approximately uniformly distributed (the solution may diverge otherwise [9]).

The problem would be linear and easy to solve, if φ was the unwrapped phase, which is not the case.

5. Using a periodogram, a, p_x and p_y are estimated for each interferogram.

6. The data are compensated for the estimated parameters.

7. Using a periodogram, z and v are estimated for each PSc.

8. The data are compensated for the estimated parameters.

9. Some points may be eliminated or added to the set of PSc on the basis of their phase stability.

10. Continue iteratively with point 5, if the changes of z and v were not small enough.

The detailed description of the algorithm may be found in [9], appendix A.

10.2 Properties of the method

Let us summarize here the advantages and disadvantages of the method:

- Point scatterers with the required density need to be in the processed area.
- Only constant velocity component is estimated (however, other articles describe improvements of this method with regard to deformations non-linear in time. The best situation is when a deformation model is available to be proved).
- A large number of scenes is required, with the perpendicular and temporal baselines to be distributed as uniformly as possible.
- The accuracy of the estimated parameters, i.e. DEM error and deformation velocity, is very good (few milimeters), but the parameters are estimated only for the permanent scatterers (they are usually interpolated for other points).

This method is being used abroad for deformation mapping; however, our department does not have software for it yet. We plan to use it in the future.

Part II

Practical processing and results

Chapter 11

Data and Area Description

11.1 Data

The data used for processing were acquired by ERS-1 and ERS-2 satellites during 1996-2000. The data were acquired at track 394, frame 2583 and then divided into two (independent) stacks, in order to reduce the perpendicular baseline to less than 300 m. Table 11.1 displays the data used.

Some data were excluded due to the fact that none of the interferograms created from this scene were coherent. These data are not mentioned in table 11.1.

11.2 Orbit precision

As orbit information, the "Delft precise orbits" were used [27]. However, at some periods, mostly due to an operational error of some satellite instrument, the orbits cannot be computed with such an accuracy to be called "precise" (radial precision in the radial direction should be 5-6 cm and about 15 cm in the across-track direction) – they are called "fast-delivery and their precision is about 2 cm worse in the radial direction and about 6 cm worse in the across-track direction [27].

For most of the scenes, precise orbit information was obtained; however, for orbits 43468 and 25933, only fast-delivery orbits were available.

For orbit 40963, no precise or fast-delivery orbits were found, and therefore less precise orbits, delivered within the data (i.e. computed during the acquisition) were used, which causes phase trend in the range direction in all intereferograms created using this scene [41]. However, we finally decided to use this scene – we hope the crops are small enough for the influence to be small.

However, it seems that a significant orbit inaccuracy is involved in scene 25432 – not only that the crops contain fringes (even the crops are very small and therefore should not), but also the DEM (in the DEM subtraction process) is localized imprecisely, making the scene 25432 unusable as the master scene. We decided to exclude all interferograms containing this scene – the fringes in these interferograms are very clear.

Orbit	satellite	date	perp. bas.
23428	ERS-1	1996-01-07	**0**
3755	ERS-2	1996-01-08	-69
24430	ERS-1	1996-03-17	77
4757	ERS-2	1996-03-18	100
25432	ERS-1	1996-05-26	-329
5759	ERS-2	1996-05-27	-433
25933	ERS-1	1996-06-30	6
9266	ERS-2	1997-01-27	26
9767	ERS-2	1997-03-03	-275
10268	ERS-2	1997-04-07	254
11771	ERS-2	1997-07-21	-249
12773	ERS-2	1997-09-29	-266
14777	ERS-2	1998-02-16	-206
15278	ERS-2	1998-03-23	-214
15779	ERS-2	1998-04-27	91
16280	ERS-2	1998-06-01	155
17282	ERS-2	1998-08-10	-258
40963	ERS-1	1999-05-16	107
23294	ERS-2	1999-10-04	-213
23795	ERS-2	1999-11-08	-209
43468	ERS-1	1999-11-07	-49
26300	ERS-2	2000-05-01	-262
28304	ERS-2	2000-09-18	130
29306	ERS-2	2000-11-27	171

Table 11.1: Data. Boldface denotes the master scene, with regard to which the perpendicular baselines are related. The perpendicular baselines are only approximate.

11.3 The area

The area to be investigated is the Norhern-Bohemian brown-coal basin. The basin is quite large (about 1420 km^2), its length is more than 80 km. The coal deposits themselves take up about 850 km^2 and their thickness is about 30 m, at some places even 60 m [38].

The coal has been mined in the basin since the 15th century using different techniques: at first, using "selské dobývání" which contains many potential hazards, then deeply and now through open-pit mines. The deeps mines are mostly situated in the central part of the basin (the coal is deposited deeper) and in the areas which make open-pit mining impossible.

According to [38], the most endangered part of the basin due to landslides is the area around the city Teplice, because this area was to be mined again, and therefore the reclamation was not performed here.

Open-pit mining is more effective than deep mining, allowing to mine about 95 % of the deposit. On the other hand, it significantly disturbs the countryside: the reclaimed areas may be unstable – however, their utilization is designed with respect to this factor. Unfortunately, sometimes it is neccessary to build a road or similar object on a waste dump – and in this case, the subsidences are significant, mainly in the first years after construction.

Deep mining was at first performed in areas near Ústí n. Labem, where the Labe River allowed to transport the coal away early in the history. Here, the deeps mines are less deep than in the Most area, and therefore the area endangered by subsidences should be smaller. However, the mining companies are responsible to make the area stable with the new deep mines – therefore, no observations with regard to deformations are performed and no areas are known to subside due to deep mines.

The Northern-Bohemian coal basin passess continuously into the Ore Mountains, and on the divide and in the Ore Mountains, there is a lot of ore mines. Also other raw materials such as clays or calcite, are being mined in the area. However, the deformations are not monitored here and no area is known to subside.

A detailed list of deep and open-pit mines, same as the other mines, is out of scope of this thesis and can be found in [39].

11.4 Crops

There are two crops processed within this thesis. One is a road built up on a waste dump, created as a by-product of the mining activities. This is the famous Ervěnice corridor, a road, railway and pipeline between the Komořany viallage and Jirkov town. The other is the village Košťany (near Teplice) and its neighbourhood (unfortunately, the coherence is bad in the neighbourhood), which may be partially undermined (in history) and which is close to a former open-pit mine (now flooded, Barbora lake, to the north and to the west from the village). In addition, the village is surrounded by waste dump transported out of the mine on the northern edge – however, the areas of the waste dump are mostly reclaimed and therefore are not expected to be coherent. The road from Košťany to Mstišov is also built on the waste dump – however, the road leads through a forest and therefore is not recognized in the image. The western part of the village (cemetery) is situated almost on the bank of the Barbora lake and is known to slide down – unfortunately, neither this area is coherent. The village lies out of the coal area; however, it contains a small separate coal bed. The centre of the village is expected to be stable [20]. In the area, also landslides can be expected (according to Geofond, [20]), but mostly in the flooded mines and also to the north-east from the village (out of the intown area).

Both areas known to subside; however, up-to-date, we have no information of the subsidence velocity.

Tables 11.2 and 11.3 show the geographic dates about these crops.

The Ervěnice corridor is known to subside – it is a road, railway and a pipe built on a waste dump in 1983. The corridor is surrounded by open-pit mines, and therefore can be easily recognized in the coherence map, see e.g. figure 13.1. The expected deformations are about 10–20 cm/year here, and are irregular.

The center of the village Košťany is situated about 1 km from the Barbora lake, black area e.g. in figure 12.8. The Barbora lake is a former open-pit mine. The waste dump

	north	west	south	east	unw. seed
SAR (az.) [pix]	17600	18200	18200	17600	464
SAR (range) [pix]	2150	2150	1900	1900	49
WGS-84 (φ) [°]	50.529252	50.508405	50.498317	50.519163	50.505016
WGS-84 (λ) [°]	13.475404	13.467872	13.537865	13.545430	13.525712
S-JTSK (Y) [m]	802487	803361	798617	797743	799359
S-JTSK (X) [m]	984772	986985	988832	986619	987968

Table 11.2: Borders of the Ervěnice crop. The SAR coordinates are specified with regard to scene 23428. The SAR coordinates of the unwrapping seed are with regard to the crop.

	north	west	south	east	unw. seed
SAR (az.) [pix]	12950	13540	13540	12950	191
SAR (range) [pix]	1370	1370	1270	1270	68
WGS-84 (φ) [°]	50.658732	50.641373	50.637119	50.654477	50.650759
WGS-84 (λ) [°]	13.757805	13.751411	13.780595	13.787000	13.764477
S-JTSK (Y) [m]	780593	781320	779346	778619	780254
S-JTSK (X) [m]	973465	975310	976077	974232	974411

Table 11.3: Borders of the Košťany crop. The SAR coordinates are specified with regard to scene 23428. The SAR coordinates of the unwrapping seed are with regard to the crop.

mined was transported and deposited at the north-eastern part of the Košťany village and the road to the Mstišov village is built on the waste dump, and therefore is also expected to subside.

The area may also be partially undermined; however, the deep mines are old and the area is not expected to subside anymore.

Chapter 12

Data Analysis

12.1 The relation between coherence and baseline

Overall coherence is computed as the mean coherence of the crop, excluding pixels with coherence 0 (these are not processed). All interferograms were processed into this analysis, not only those selected for postprocessing.

We know that the overall coherence is not a measure of the interferogram quality – and that the coherence of the area of interest should be measured instead – however, the overall coherence may be used as a measure for comparison of various interferograms.

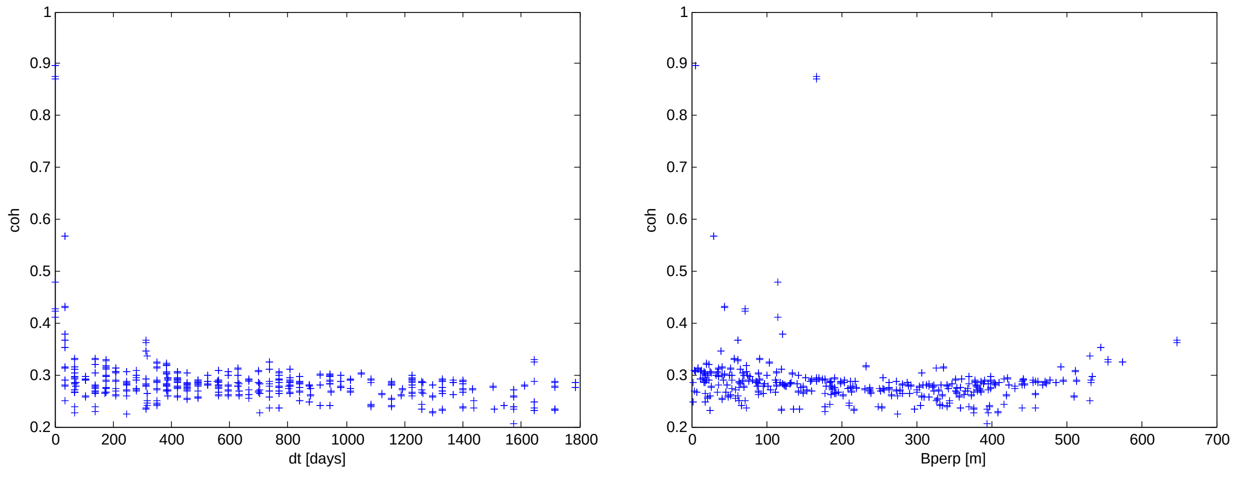

a b

Figure 12.1: The relation between the temporal baseline and coherence (a) and between the perpendicular baseline (absolute) and coherence (b) for the Košťany area. All points in the crop were processed into this graphs, not only the points selected for further processing.

Please note that the points in the graphs appear in pairs – these are two interferograms created from the same two scenes, only master and slave are interchanged. The difference in coherence is not very clear and is usually very low (except for the tandem pair

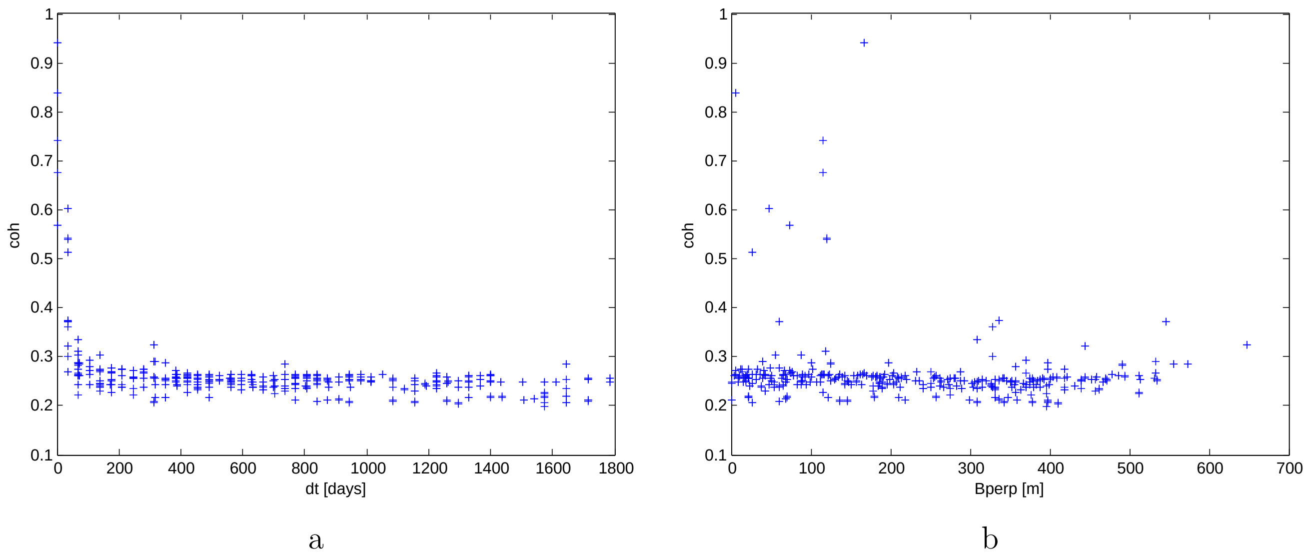

Figure 12.2: The relation between the temporal baseline and coherence (a) and between the perpendicular baseline (absolute) and coherence (b) for the Ervěnice area. All points in the crop were processed into this graphs, not only the points selected for further processing.

25432 and 5759, where a large orbit error is suspected for 25432 (also other facts support this suspection, such as fringes in interferograms made from it, different look of the interferogram after DEM subtraction etc.).

12.2 Phase sums in cycles

Theoretically, phase sum in cycles should be zero according to equations (8.17) and (8.18). This applies for the interferogram phases (after complex-conjugate multiplication), for the flattened interferogram phases, and also for DEM-subtracted phases. If a constant error is present, it is eliminated by referencing the phase to a selected point (as described in section 13.4).

However, the sums in cycles are never exactly zero. Also, for the processing method, where scenes are resampled in advance and then complex-conjugated multiplicated with each other, even the decorrelation is not the cause of the non-zero phase sums. Possible causes for non-zero sums in interferogram doubles are following:

- inappropriate referencing (i.e. the phase of the reference point has a bad value); the other influences are almost negligible;
- phase filtering in decorrelated areas – the phase may change significantly during filtering if the neighbouring pixels have significantly different values – the difference may be caused by filtering rules with respect to the master magnitude;
- an error in the phase of the reference point – its phase may be influenced by phase filtering; in this case, the sum is non-zero, but constant;

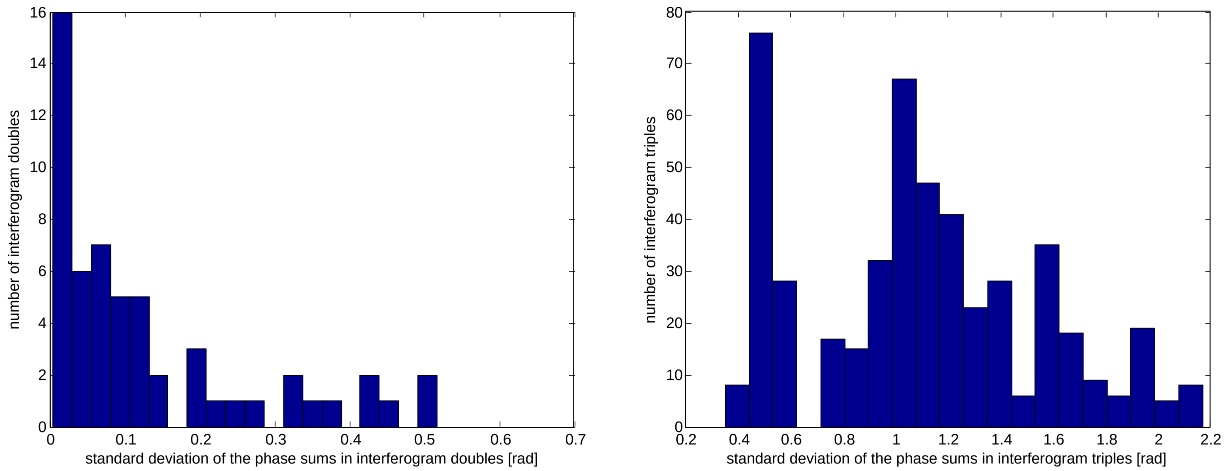

a b

Figure 12.3: Histogram of the phase sum standard deviation $\sigma_{cyc,i,intf}$ for interferogram doubles (a) and triples (b) for the Ervěnice area.

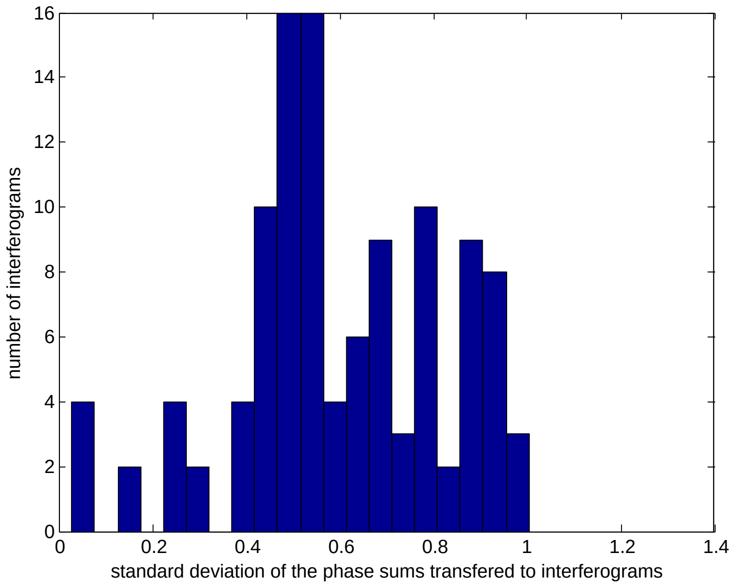

Figure 12.4: Overall histogram of m computed using (12.3) for the Ervěnice area. Please note that the zeros correspond to interferograms excluded due to a low coherence value of the reference pixel.

- processing noise, i.e. rounding errors, which are not expected to be significant.

For interferogram triples, the following causes may apply in addition:

- orbit error influence, as described in section 9.1 – each interferogram in the triple has different parallel baseline;

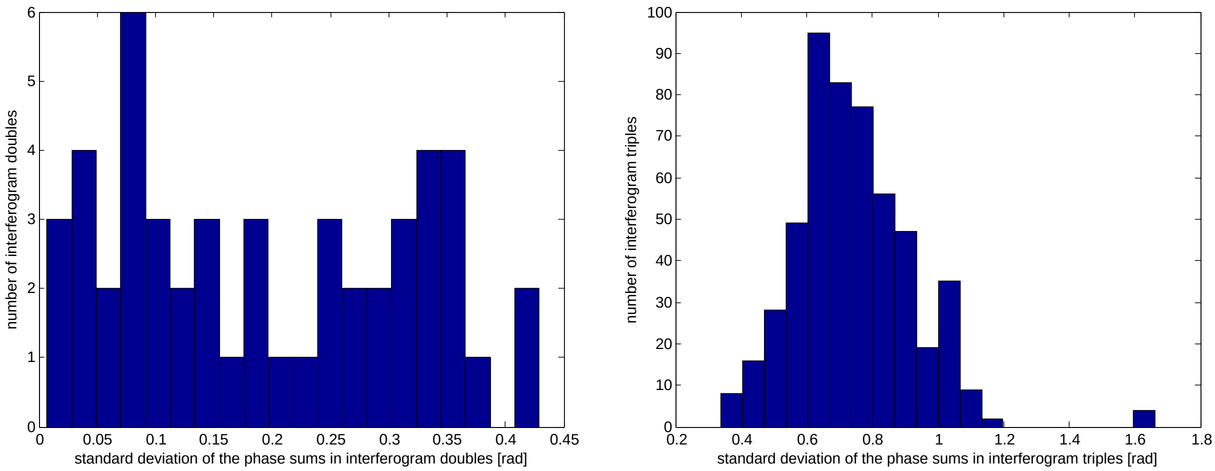

a b

Figure 12.5: Histogram of the phase sum standard deviation $\sigma_{cyc,i,intf}$ for interferogram doubles (a) and triples (b) for the Košťany area.

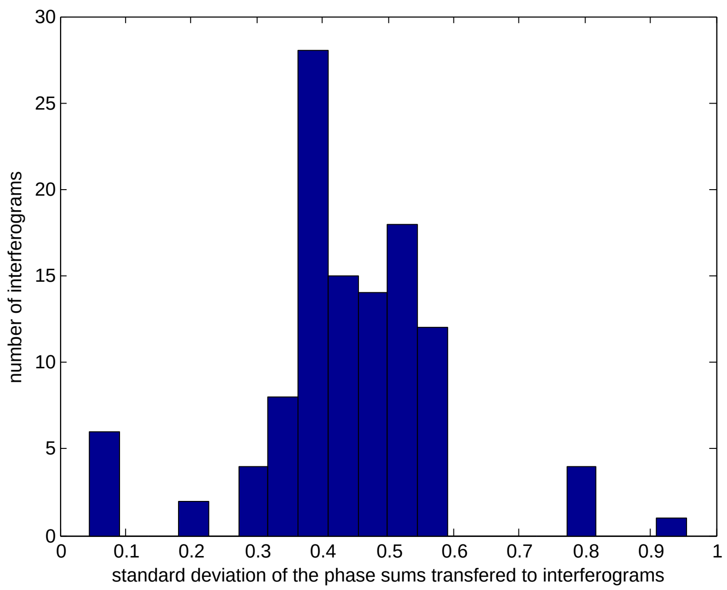

Figure 12.6: Overall histogram of m computed using (12.3) for the Košťany area.

- DEM error influence, as described in section 9.2 – each interferogram in the triple has different perpendicular baseline.

Both of these influences apply for both the processed and reference points.

None of these errors (except for the processing noise) causes decorrelation in a single interferogram.

During processing, the phase sums are tested pixelwise – in order to decide whether an interferogram/point is to be excluded from the processing or not. Here, we make an overall analysis of the data with the purpose to exclude hugely errorneous interferograms or just to get an information about the phase accuracy.

12.2.1 Analysis

Let us note first that this analysis is performed only for interferograms selected for processing, but for all points in the interferogram (the selection procedure is described in section 13.2.

For each interferogram double or triple (cycle), the phase sum is computed on the pixel-by pixel basis. All interferograms are referenced to a selected point before actual summing. Then the phase sum standard deviation is computed

$$\sigma_{\sum\Delta\varphi} = \sqrt{\frac{\sum_{i=1}^{N}(\sum\Delta\varphi)_i^2}{N}}, \tag{12.1}$$

where N is the number of points in the interferograms and $\sum\Delta\varphi$ stands for the phase sum in a cycle. Let us note here that the correct value of the phase sum is known to be zero.

However, the information about a high or small phase sum standard deviation in a phase sum is kind of inapplicable – we would rather get an information about a quality of a particular interferogram. We decided to transfer the standard deviation information to the interferogram set using the following procedure:

- First, the phase sum STD are "distributed" into all interferograms involved in the particular cycle:

  $$c = |C| \cdot \frac{\sigma_{cyc,i,intf}}{\sqrt{n}} \tag{12.2}$$

  separately for each line of C, yielding a line of c. C is the matrix of phase cycles, see equation (8.19)), n is the number of interferograms in the particular cycle.

- Then, the phase STD are averaged for each interferogram (STD from different phase cycles are averaged):

  $$m = \frac{\sum C \cdot |c|}{\sum |c|}, \tag{12.3}$$

  now computed separately for each column of C, c.

This analysis can also be used for the estimation of the phase error to be used for statistical tests after adjustment (see section 13.9). We estimate it as

$$\sigma_{\Delta\varphi apr} = \sqrt{\frac{\sum m^2}{n}} \tag{12.4}$$

where n is the number of interferograms. For the Ervěnice area, $\sigma_{\Delta\varphi apr} = 0.65$ rad (37°), for the Košťany area, $\sigma_{\Delta\varphi apr} = 0.51$ rad. These values were computed only using the points selected for further processing (see section 13.2). These values are computed from all interferograms except for those preliminarily excluded due to orbit errors (i.e. interferograms containing scene 25432). Individual interferogram exclusion, as described in section 13.4.3, was performed after these computations, gaining $\sigma_{\Delta\varphi apr} = 0.53$ rad for the Ervěnice area and 0.47 rad for the Košťany area.

However, to evaluate the final phase standard deviation for an interferogram, we must quadratically sum this value with the standard deviation caused by decorrelation (0.64 rad using (6.8), and therefore we use 0.83 rad for the Ervěnice area, and 0.82 rad for the Košťany area. These are final values computed after exclusion of individual interferograms (see section 13.4.3). Please note that these numbers are different for the wrapped and unwrapped interferograms due to the fact that different interferograms were selected (different thresholds) and different interferograms were excluded. Details can be found in section 13.4.3.

12.3 Preliminary estimation of the DEM error

The DEM error, as mentioned in section 8.8, is estimated preliminarily from eight tandem interferograms, which are included in the dataset. We assume that the one-day temporal baseline did not allow the deformations to occur or the deformations were negligible.

Because there are four tandem pairs in the dataset, eight interferograms were created out of them. Their (wrapped) phase is presented in figures 12.7 and 12.8. It can be seen that the interferograms are similar in pairs (except for the 25432 – 5759 and 5759 – 25432 pair which is discussed below). However, the difference between the particular doubles can be attributed to the DEM errors.

In accordance with section 12.2, where the reasons for non-zero phase sums in interferogram doubles are described, and due to the fact that tandem interferograms are mostly coherent (see figures 12.7 and 12.8), the phase referenced to a certain point is expected to be close to zero. The referencing errors are expected to apply here only insignificantly, the observed phase of the reference pixel should be opposite in both interferograms and the reference pixel is selected to be very coherent. The only error influence expected here may be the DEM error (deformations are excluded by the assumption of the short temporal baseline).

Obviously, there is a problem with interferogram 25432 – 5759. This problem is similar to all interferograms which have 25432 as master, and due to the fact that a hole can be seen in the interferogram, similar to other interferograms, which originates from the step of DEM-phase subtraction, we assume that orbits of 25432 have a large error. The scene 25432 was excluded from the following processing.

Due to the fact that some of the interferograms were unable to be unwrapped with the seed selected for the whole set, a different seed was located for the analysis – as the most coherent point within the Ervěnice corridor (coordinates 340 (line), 70 (pixel) within the crop). The most coherent point for the Košťany crop is 439 (line), 16 (pixel).

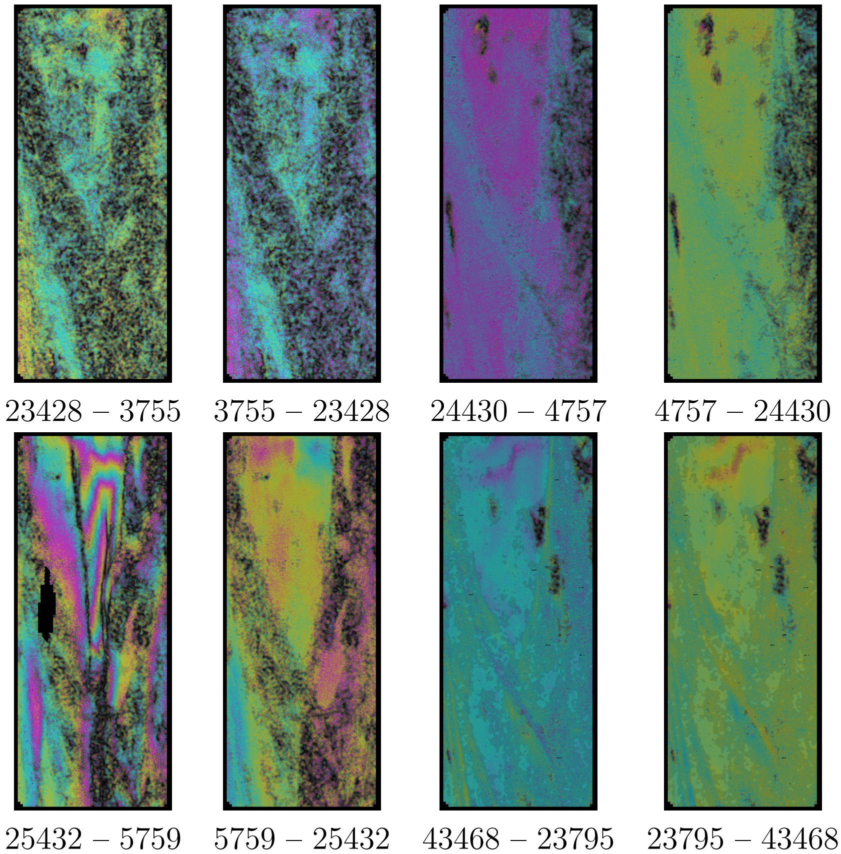

Figure 12.7: Tandem interferograms of the Ervěnice crop: the first orbit corresponds to the master image, the second one to the slave image. Please note the obvious difference between 25432 – 5759 and 5759 – 25432. All points of the Ervěnice crop are imaged here, the points to be processed are filtered later. The phase scale is imaged in figure 12.9.

Tables 12.1 and 12.2 contain the mean of the referenced phase within the pixels selected for processing (as selected during the process described in Chapter 13.2). Please note that a large value here may be caused by several factors, such as decorrelation (however, in this case the pair sum is near zero), orbit errors (if the orbit error difference within each pair is large, the pair sum is also large) or atmosphere delay trend (no influence on the phase sum). Scene 25432 has a very large orbit error (also indicated in figures 12.7 and 12.8 where interferograms 25432 – 5759 and 5759 – 25432 are significantly different). For interferogram pair 23428 – 3755 and 3755 – 23428, the large values are probably caused by decorrelation with higher probability of unwrapping errors.

12.3.1 Resampling interferograms from different track

In order to increase the number of tandem interferograms available for DEM error estimation, another two tandem pairs were used which were acquired on a neighbouring track. The area of interest is in the overlapping area. Some details about the data are contained in table 12.3.

The area to be cropped from these scenes was obtained through geocoding of the inter-

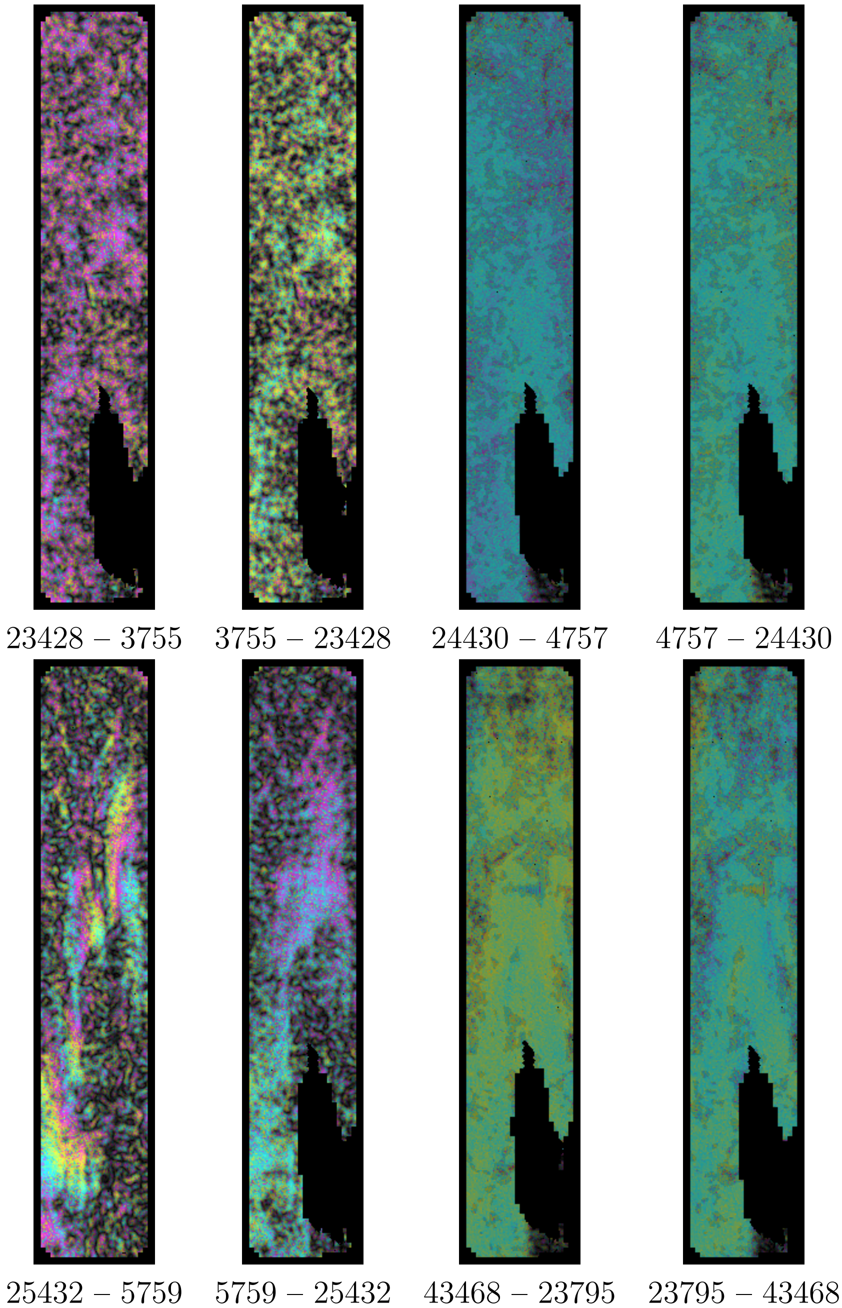

Figure 12.8: Tandem interferograms of the Košťany crop: the first orbit corresponds to the master image, the second one to the slave image. Please note the obvious difference between 25432 – 5759 and 5759 – 25432. All points of the Košťany crop are imaged here, the points to be processed are filtered later. The phase scale is imaged in figure 12.9.

Figure 12.9: Colorscale for the wrapped phase. $-\pi$ on the left, π on the right.

interferogram	phase mean [rad]	interferogram	phase mean [rad]	sum [rad]
23428 – 3755	-3.8459	3755 – 23428	4.3570	**0.5111**
24430 – 4757	0.1640	4757 – 24430	-0.1531	**0.0109**
25432 – 5759	6.5836	5759 – 25432	-2.0963	**4.4873**
43468 – 23795	0.1578	23795 – 43468	-0.1176	**0.0402**
24659 – 4986	-0.7509	4986 – 24659	1.3325	**0.5816**
25160 – 5487	-0.5014	5487 – 25160	0.5333	**0.0319**

Table 12.1: Unwrapped and referenced (to a single point) phase mean of each of the processed interferograms for the Ervěnice crop. The mean is computed only within the points selected for further processing.

ferograms from the regular track (394) and estimating the SAR coordinates using the `coord_to_sarpix` script – however, this script works only approximately, not using any height information, and the results are therefore approximate too. The coordinates used for cropping (using the `SLC_copy` script) are given in tables 12.4 and 12.5.

The interferograms created from the scenes described in table 12.3 are shown in figures 12.10 and 12.11. As in the previous analysis, four interferograms were created, alternating the master and slave images for each pair.

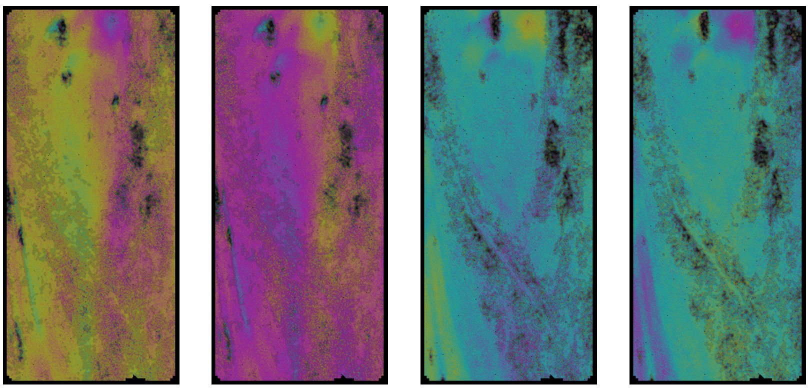

24659 – 4986 4986 – 24659 25160 – 5487 5487 – 25160

Figure 12.10: The (non-unwrapped) phase of the tandem interferograms from track 122 for the Ervěnice crop. The colorscale is the same as in other cases and is shown in figure 12.9. Please note that the image scale is different from the original track interferograms (here the crop was 600 lines by 250 pixels), for the new track it is 612 lines by 285 pixels (see table 12.4).

Then, the interferograms (possibly together with their coherence maps) are geocoded (using the `geocode_back` script). The result is an interferogram in the WGS-84 coordinates

interferogram	phase mean [rad]	interferogram	phase mean [rad]	sum [rad]
23428 – 3755	-45.1023	3755 – 23428	42.9522	**-2.1501**
24430 – 4757	0.3685	4757 – 24430	-0.3475	**0.0210**
25432 – 5759	42.9522	5759 – 25432	11.9333	**54.8855**
43468 – 23795	0.2871	23795 – 43468	0.0343	**0.3214**
24659 – 4986	0.8337	4986 – 24659	-0.7836	**0.0501**
25160 – 5487	-0.0173	5487 – 25160	-0.3529	**-0.3702**

Table 12.2: Unwrapped and referenced (to a single point) phase mean of each of the processed interferograms for the Košťany crop. The mean is computed only within the points selected for further processing.

orbit	date	satellite
24659	1996-04-02	ERS-1
4986	1996-04-03	ERS-2
25160	1996-05-07	ERS-1
5487	1996-05-08	ERS-2

Table 12.3: Basic data of the four scenes to form two tandem interferograms from track 122.

and the borders and the size of the area should be similar to those generated by geocoding of the original track interferograms. However, the area is not exactly the same, probably due to the approximity of the initial SAR coordinates, as described above. The exact borders and scale of the area may be found in the parameter file of the DEM crop.

If both geocoded areas are not exactly the same, the geocoded interferograms (and coherence maps) have to be adapted in order to exactly correspond to the geocoded area of the original track interferograms. This is performed in MATLAB, manually by adding or removing some lines or pixels.

Then, the original track lookup table (generated during the geocoding process) should be inversed, using the `gc_map_inverse` script. If both the desired width and height of the resulting data are specified, the resulting lookup table fits it – this is the case when the width and height of the original track interferogram is used. If the height is unspecified, the resulting data are much larger – containing all possible pixels within the large area of the geocoded data. Then, the interferograms (possibly together with their coherence maps) are geocoded (using the `geocode_back` script). The result is an interferogram in the WGS-84 coordinates and the borders and the size of the area should be similar to those generated by geocoding of the original track interferograms. However, the area is not exactly the same, probably due to the approximity of the initial SAR coordinates, as described above. The exact borders and scale of the area may be found in the parameter file of the DEM crop.

Then, the resampling of the geocoded data from the new track is performed, using the `geocode_back` script and the lookup table from the original track data. Also here, both the width and height of the original track data must be specified in order to obtain the

master scene	min range	max range	min azimuth	max azimuth	width	height
24659	4513	4798	20318	20930	285	612
25160	4457	4742	20272	20883	285	612

Table 12.4: Coordinates of the cropped Ervěnice area from the scenes acquired on track 122. Scene 4986 was resampled on scene 24659 and scene 5487 was resampled on 25160, so the coordinates of the other two scenes are similar.

master scene	min range	max range	min azimuth	max azimuth	width	height
24659	3779	3894	15701	16206	115	505
25160	3724	3839	15655	16160	115	505

Table 12.5: Coordinates of the cropped Košťany area from the scenes acquired on track 122. Scene 4986 was resampled on scene 24659 and scene 5487 was resampled on 5487, so the coordinates of the other two scenes are similar.

desired scale of the data.

During all resampling steps (`geocode_back`), the nearest-neighbor method was selected (default).

The interferograms resampled to the original track are shown in figures 12.12 and 12.13.

Phase unwrapping should be performed at the end, in order to ensure the same unwrapping seed as in the original track interferograms.

12.3.2 DEM error estimation – theory

Table 12.6 lists the approximate values of the perpendicular baseline for particular scene pairs.

	Ervěnice		Košťany
interferogram	$B_{\perp min}$ [m]	$B_{\perp max}$ [m]	$B_{\perp}$ [m]
23428 – 3755	-72.40	-72.21	-72.09
24430 – 4757	21.76	21.92	22.33
25432 – 5759	-105.00	-104.74	-105.58
43468 – 23795	-165.64	-165.30	-165.74
24659 – 4986	-82.46	-82.29	-84.42
25160 – 5487	-101.50	-101.25	-105.03

Table 12.6: Minimum and maximum perpendicular baseline for the interferograms (depends both on the azimuth and range coordinates). For the remaining interferograms, the perpendicular baseline is the negative value of the "opposite" interferogram. The Košťany crop is so small that the GAMMA `base_perp` script only gives one value.

DEM error estimation is based on formula (9.3). This formula may be significantly simplified if only interferograms from one track are used; however, in our case, the only constant

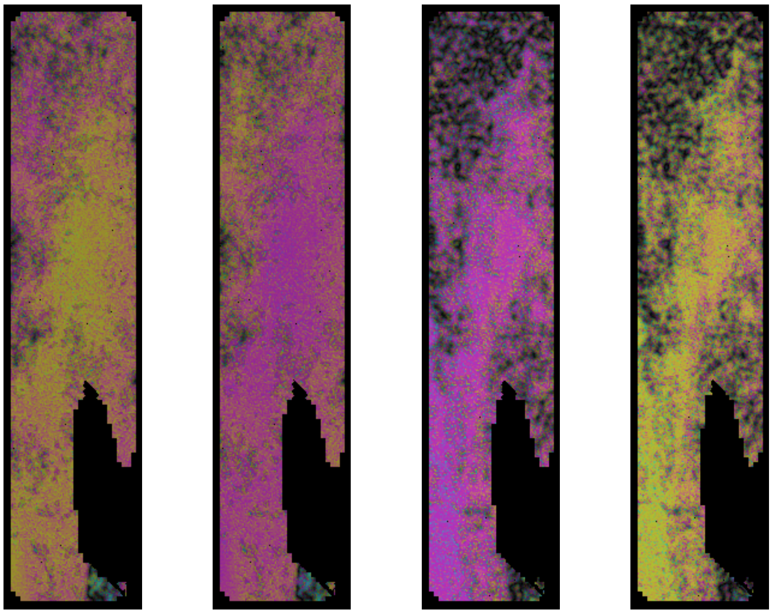

Figure 12.11: The (non-unwrapped) phase of the tandem interferograms from track 122 for the Košťany crop. The colorscale is the same as in other cases and is shown in figure 12.9. Please note that the scale is different from the original track interferograms (here the crop was 500 lines by 100 pixels), for the new track it is 505 lines by 115 pixels (see table 12.5).

to be eliminated is the expression $c_{gen} = \frac{4\pi}{\lambda} dh$.

Formula (9.3) may be rewritten as

$$d(\Delta\varphi_{DEM}) = c_{gen} c_{tr} B_{\perp}, \tag{12.5}$$

where coefficient c_{gen} is the same for all interferograms and coefficient c_{tr} depends on the track. The residual phase $d(\Delta\varphi_{DEM})$ stands here for the interferogram phase.

Due to the non-zero phase sums for the interferogram doubles, which we attribute to small errors in the orbits (or baseline), we use the average of both interferograms. For the DEM error estimation within one of the tandem interferogram double, we may write

$$\Delta\varphi_{A-B} = cB_{\perp,A-B} + \Delta\varphi_{err,A-B}, \tag{12.6}$$

$$\Delta\varphi_{B-A} = -cB_{\perp,A-B} + \Delta\varphi_{err,B-A}, \tag{12.7}$$

where $\Delta\varphi_{err,A-B}$ is the errorneous phase of the interferogram (A is the master scene, B is the slave one), attributed to orbit errors and atmosphere, and $c = c_{gen} \cdot c_{tr}$ (simplified for an interferogram double).

One may say that the atmospheric influence is contained in the interferograms and this contribution is large enough to prevent any adjustment. However, the most of the atmospheric influence was eliminated by referencing the interferograms to a single point, and

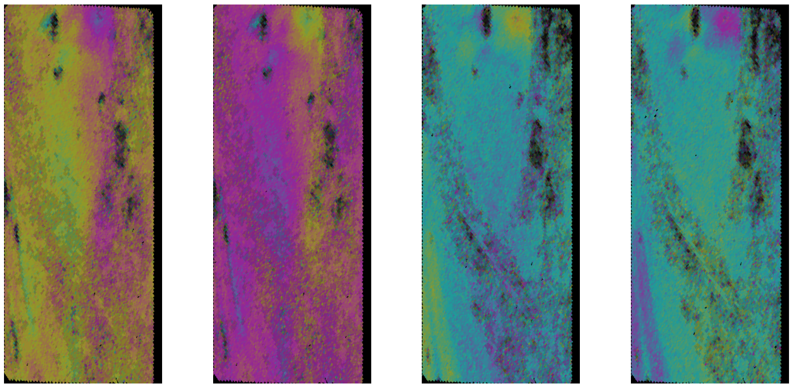

24659 – 4986 4986 – 24659 25160 – 5487 5487 – 25160

Figure 12.12: The (non-unwrapped) phase of the tandem interferograms from track 122 (Ervěnice area), resampled to the interferograms from track 394. The colorscale is the same as in other cases and is shown in figure 12.9.

the rest (small enough to allow adjustment) is contained in the adjustment residues. This only requires the area to be small enough.

Therefore, the first estimate (within one double of the tandem interferograms) of the DEM-error influenced phase is

$$\frac{\Delta\varphi_{A-B} - \Delta\varphi_{B-A}}{2} = \frac{\Delta\varphi_{err,A-B} - \Delta\varphi_{err,B-A}}{2} + cB_{\perp,A-B}, \tag{12.8}$$

that means

$$\Delta\varphi_{A-B} = cB_{\perp,A-B} = \frac{\Delta\varphi_{A-B} - \Delta\varphi_{B-A}}{2} \tag{12.9}$$

due to the unknown values of the errorneous phase (and expected zero mean).

Now, the twelve tandem interferograms may be compressed into six. Then, an adjustment model may be written as (considering c_{gen} as the unknown due to the DEM error dh it contains)

$$\Delta\varphi = \frac{4\pi}{\lambda} dh B_{\perp tr} + e, \tag{12.10}$$

where $\Delta\varphi$ is the vector of interferogram phases for all four interferograms given by (12.9), $B_{\perp tr} = c_{tr} B_{\perp}$ for each interferogram and e is the vector of residues to be minimized. Then,

$$c_{gen} = (B_{\perp tr}^T B_{\perp tr})^{-1} B_{\perp tr}^T \Delta\varphi. \tag{12.11}$$

12.3.3 Precision analysis

During the following analysis, we will try to neglect as many factors and differences as possible. Table 12.7 shows several imaging parameters for one of the scenes for each track.

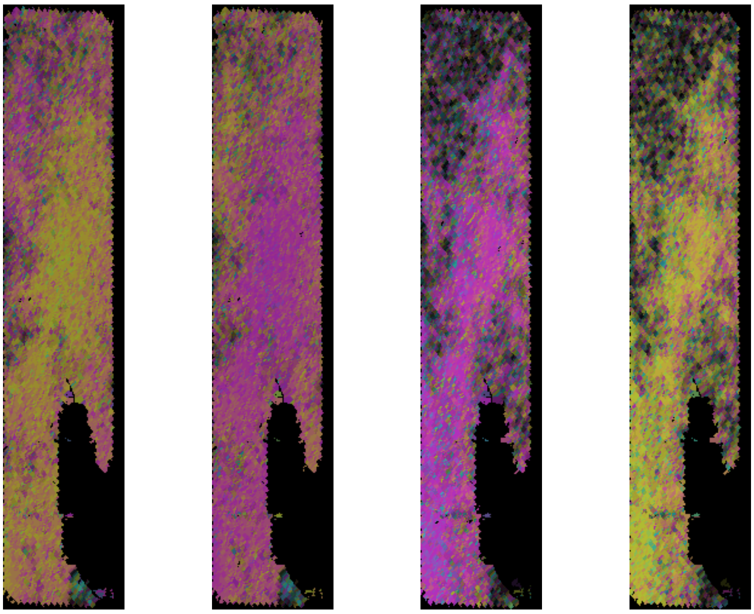

Figure 12.13: The (non-unwrapped) phase of the tandem interferograms from track 122 (Košťany area), resampled to the interferograms from track 394. The colorscale is the same as in other cases and is shown in figure 12.9.

Table 12.7 shows that there is a very significant difference between the coefficients c_{tr} for each track – about an order higher than is the difference between the coefficients computed for close and far ranges within one track. On the other hand, the c_{tr} factor may stay the same when estimating DEM error only from one-track data - even if the scenes are shifted with regard to each other by even a hundred of pixels in the range direction (we found at most about 80 pixels), generating a phase difference of about 0.005 rad (0.3 degree) for DEM error of 10 m and perpendicular baseline of 100 m. In that case, the difference between close and far range may be neglected – it will be contained in the estimated dh factor.

However, we enumerated that the DEM error estimation from two-track data cannot be so simple due to the fact that the phase difference is about 0.1 rad (6 degrees) for a pair with perpendicular baseline of 100 m and DEM error of 10 m. On the other hand, we decided to neglect the difference between the close and far ranges – it will be contained in the estimated dh factor (the difference between particular tracks in the last row of table 12.7 is negligible).

We therefore decided to compute the c_{tr} coefficients for each interferogram (represented by its master scene) individually, but we will use the same value for all pixels of the crop, setting dh not to be the DEM error exactly, but containing also the influence of the range.

Another factor, which is to analyze, is the variability of perpendicular baseline $B_\perp$ which is also significantly dependent on the range. The maximum and minimum baselines for each interferogram can be found in table 12.6. If a baseline does not change even by a meter within an interferogram, it means that the influence on the phase is about 0.0005 rad which is negligible in comparison to other error influences. Therefore, we will also compute the

track (orbit)	**394 (24430)**		**122 (25160)**	
	close range	far range	close range	far range
range pixel	1900	2150	4457	4742
range R_M [m]	849003	850970	869310	871555
SAR to Earth center [m]	7157103		7157083	
look angle Θ [deg]	19.9112	20.1659	22.9203	23.1331
Earth-center angle ε [deg]	2.6069	2.6417	3.0488	3.0838
incidence angle $\Theta+\varepsilon$ [deg]	22.5181	22.8076	25.9691	26.2169
$\frac{1}{\sin(\Theta+\varepsilon)R_M}$ [m^{-1}]	3.0720e-6	3.0315e-6	2.6270e-6	2.5972e-6
$\frac{4\pi}{\lambda}\frac{1}{\sin(\Theta+\varepsilon)R_M}$ [m^{-2}]	**6.8084e-4**	**6.7187e-4**	**5.8223e-4**	**5.7562e-4**
close/far rate (previous line)	1.013		1.011	

Table 12.7: Various imaging parameters for one scene of each track. Precise ranges were found in the parameter file for the scene (.slc.par), look angles were enumerated using the `base_perp` script. The remaining parameters were computed by hand. All parameters refer to the Ervěnice crop. Similar values can be computed for the Košťany crop, where no such analysis has been performed.

perpendicular baseline for the crop center and use this value as a perpendicular baseline for all pixels of the crop.

Tables 12.8 and 12.9 list the important parameters for each interferogram (with regard to the central point of the master crop).

scene	Θ [deg]	$B_\perp$ [m]	range [m]	ε [deg]	$\frac{4\pi}{\lambda}c_{tr}$ [m^{-2}]	$\frac{4\pi}{\lambda}B_{\perp tr}$ [m^{-1}]
23428	20.0435	-72.30	850084	2.6235	6.7652e-4	-0.04891
3755	20.0477	72.30	850113	2.6241	6.7636e-4	0.04890
24430	20.0389	21.84	849986	2.6226	6.7676e-4	0.01478
4757	20.0372	-21.84	850006	2.6225	6.7679e-4	-0.01478
25432	20.0613	-104.87	850072	2.6257	6.7597e-4	-0.07089
5759	20.0689	104.87	850126	2.6268	6.7568e-4	0.07086
43468	20.0476	-165.47	850143	2.6242	6.7634e-4	-0.1119
23795	20.0553	165.47	850193	2.6253	6.7605e-4	0.1119
24659	23.0801	-82.37	870875	3.0746	5.7734e-4	-0.04756
4986	23.0844	82.37	870911	3.0753	5.7722e-4	0.04755
25160	23.0267	-101.37	870432	3.0663	5.7891e-4	-0.05868
5487	23.0317	101.37	870487	3.0671	5.7875e-4	0.05867

Table 12.8: Parameters for each interferogram (master scene) with regard to the central point of the Ervěnice crop.

scene	Θ [deg]	$B_\perp$ [m]	range [m]	ε [deg]	$\frac{4\pi}{\lambda}c_{tr}$ [m^{-2}]	$\frac{4\pi}{\lambda}B_{\perp tr}$ [m^{-1}]
23428	19.0788	-72.08	844511	2.4856	7.1402e-4	-0.05147
3755	19.0831	72.08	844540	2.4863	7.1384e-4	0.05145
24430	19.0740	22.33	844415	2.4847	7.1428e-4	0.01595
4757	19.0723	-22.33	844435	2.4846	7.1432e-4	-0.01595
25432	19.0967	-105.58	844495	2.4878	7.1340e-4	-0.07532
5759	19.1046	105.58	844547	2.4890	7.1307e-4	0.07529
43468	19.0831	-165.74	844570	2.4863	7.1381e-4	-0.11830
23795	19.0909	165.74	844618	2.4875	7.1349e-4	0.11830
24659	22.1686	-82.56	864402	2.9374	6.0429e-4	-0.04989
4986	22.1734	82.56	864437	2.9381	6.0414e-4	0.04988
25160	22.1135	-101.86	863967	2.9289	6.0603e-4	-0.06172
5487	22.1187	101.86	864020	2.9298	6.0585e-4	0.06171

Table 12.9: Parameters for each interferogram (master scene) with regard to the central point of the Košťany crop.

12.3.4 Results

The interferogram double 25432 – 5759, 5759 – 25432 was excluded due to errorneous orbits of 25432. After adjustment, where large DEM errors were estimated, probably caused by unwrapping errors in the low-coherent interferogram double 23428 – 3755, 3755 – 23428, this pair was also excluded. The DEM error estimated from the remaining four interferogram doubles is within $\pm$ 10 m (is higher outside of the corridor but this is not interesting and is probvably caused by unwrapping errors).

The unwrapping error correction based on adjustment residues and described in section 13.6 was used in this case because small unwrapping errors are expected here. The maximum scale found in this adjustment was -2 to 3. Then, all residues are smaller than π. However, the resulting DEM-error map is not very smooth – on the other hand, when we tried to perform the DEM-error estimation with the wrapped phase, the results were even worse – higher DEM error estimated and the map was even less smooth.

Due to the fact that some unwrapping errors may still appear in the result, however not often, we decided to perform low-pass filtering on the result. This is a bit complicated due to the presence of NaNs (not-a-number) out of the processed area and standard MATLAB function `filter2` cannot be used because it causes that the result is even narrower. Therefore, a new function dealing with NaNs in the right way was constructed. Standard convolution filtering was performed and the matrix used is

$$M_{filt} = \begin{bmatrix} 1 & 2 & 1 \\ 2 & 3 & 2 \\ 1 & 2 & 1 \end{bmatrix}. \tag{12.12}$$

The result is imaged in figures 12.15 and 12.16 and we consider it suitable (the SRTM DEM in this area is also smooth). The situation is a bit worse in the case of the Košťany crop where more points with unwrapping errors are assumed.

Figure 12.14: Colorscale for the DEM error. The left and right borders are defined individually for each image.

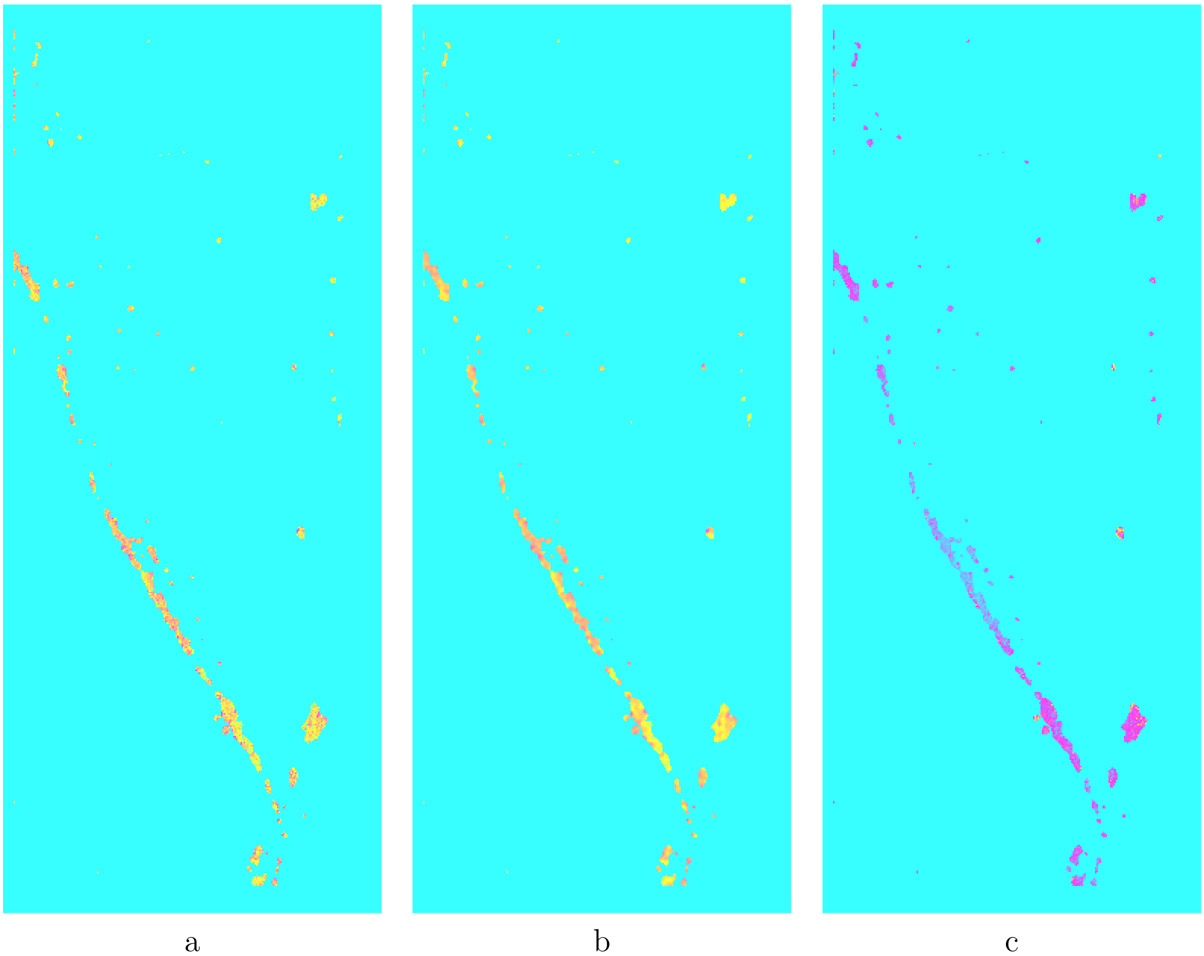

Figure 12.15: DEM error estimated from four tandem interferograms (a), its filtered version (b) and its unique standard deviation (c) for the Ervěnice crop. The colorscale is imaged in figure 12.14, here -6π on the left and 6π on the right for the DEM error and 0 on the left and π on the right for the unique standard deviation.

12.4 Temporal standard deviation

The idea to compute a temporal standard deviation of each point of the interferogram was inspired by [36]. Stefania Usai in her thesis computes the temporal standard deviation in order to measure the quality of each point. She used the interferogram phases referenced to a single point.

According to her, the temporal standard deviation should be small for stable points,

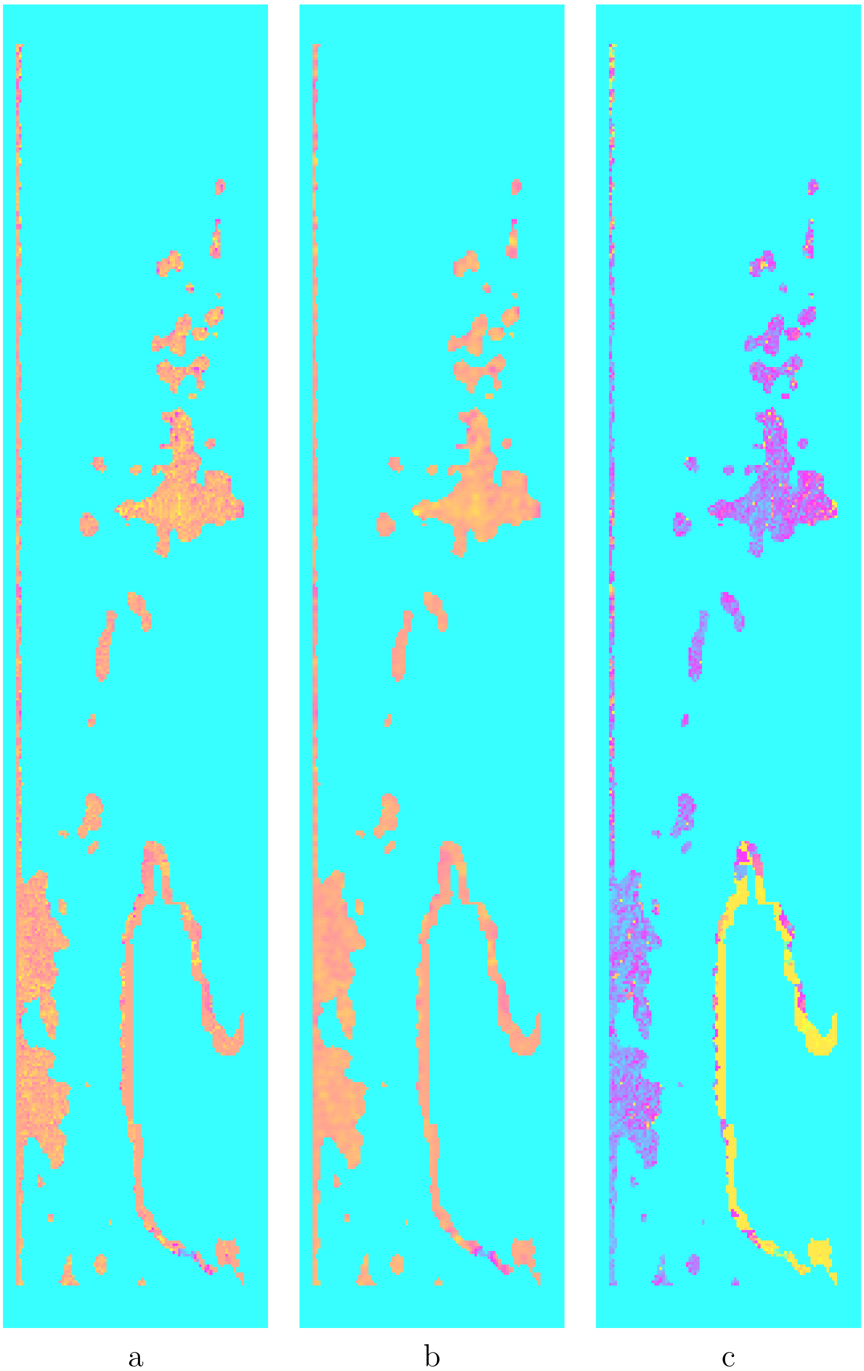

Figure 12.16: DEM error estimated from four tandem interferograms (a), its filtered version (b) and its unique standard deviation (c) for the Košťany crop. The colorscale is imaged in figure 12.14, here -12π on the left and 12π on the right for the DEM error and 0 on the left and π on the right for the unique standard deviation.

because the referenced phase is expected to be similar in all interferograms (she supposes the reference point is stable but we cannot guarantee it).

However, for unstable points the temporal standard deviation is expected to be higher, and due to the fact that unwrapping errors may apply, the phases in the temporal dimension may also have uniform distribution.

In order for the temporal standard deviation to contain an information, i.e. be independent from phase unwrapping errors, it is computed from the phases in the ambiguous interval $(-\pi, \pi)$.

Phase mean is computed regularly with the assumption that the phase is represented in the above mentioned interval; phase standard deviation is computed similarly; however, the differences between the particular values and the mean are adjusted to be always in the same interval.

Finally, we decided to compute a different phase mean and phase standard deviation: we use the wrapped value and before further computations, we divide it by the temporal baseline, yielding the phase change in a day. Therefore, we compute the mean of the daily phase change and its standard deviation.

Please note that for these computations, DEM-error corrected interferograms were used and interferograms containing scenes 25432 and 40963 were excluded due to orbit errors. The results can be found in figures 12.17 and 12.18.

The following conclusions may be done on the basis of the computed means and standard deviations: the deformations are not significant and may get lost in the unwrapping errors. However, the adjustment is much more precise and the deformations may appear there. It may also suggest to perform the iterative adjustment (see next chapter) with the wrapped phase, instead of the unwrapped one – the unwrapping errors are higher in the unwrapped case and the iterative adjustment works better if the unwrapping errors are smaller.

A trend can be seen in figures 12.17 and 12.18. This trend is probably caused by residual atmospheric influence – in adjustment, the atmospheric delay will be a part of the computed deformations where it can be filtered out using a low-pass filter (in the deformation model).

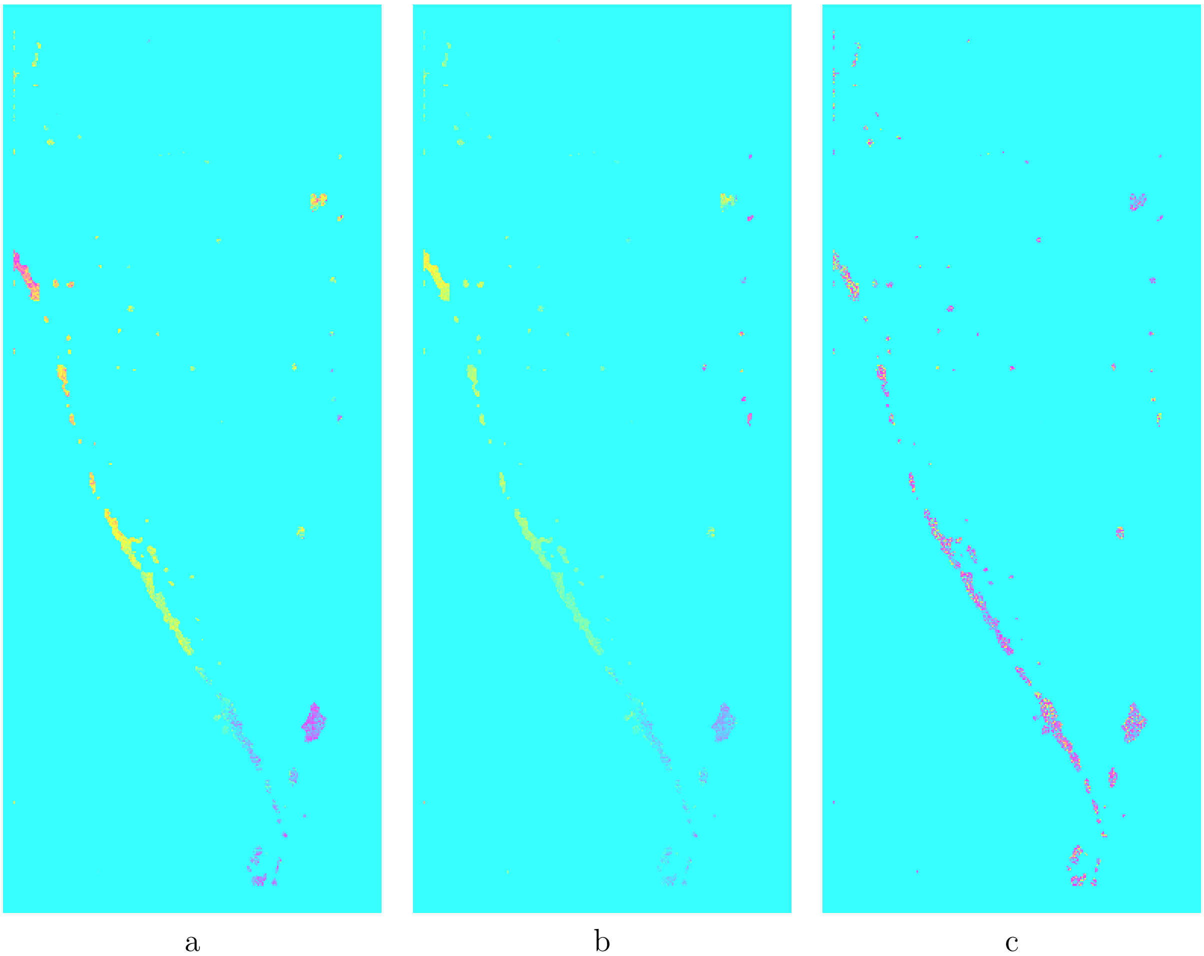

Figure 12.17: Deformation velocity average within the selected interferograms computed with the wrapped phase (a), deformation velocity average computed with the wrapped phase (b) and temporal standard deviation computed with the wrapped phase (c) for the Ervěnice crop. The colorscale is imaged in figure 12.14 and the range is: $(-0.25; 0.25)$ for (a), $(-0.5; 0.5)$ for (b) and $(0; 2)$ for (c). However, there are only 96 points (not spatially continuous) in the crop for which the absolute value of the deformation velocity average is higher than three times its standard deviation. This means that the area is stable by the first approximation. The significant difference between (a) and (b) also indicates many unwrapping errors, particularly further away from the unwrapping seed which is the same as the reference point (near the blue-yellow boundary in (b)).

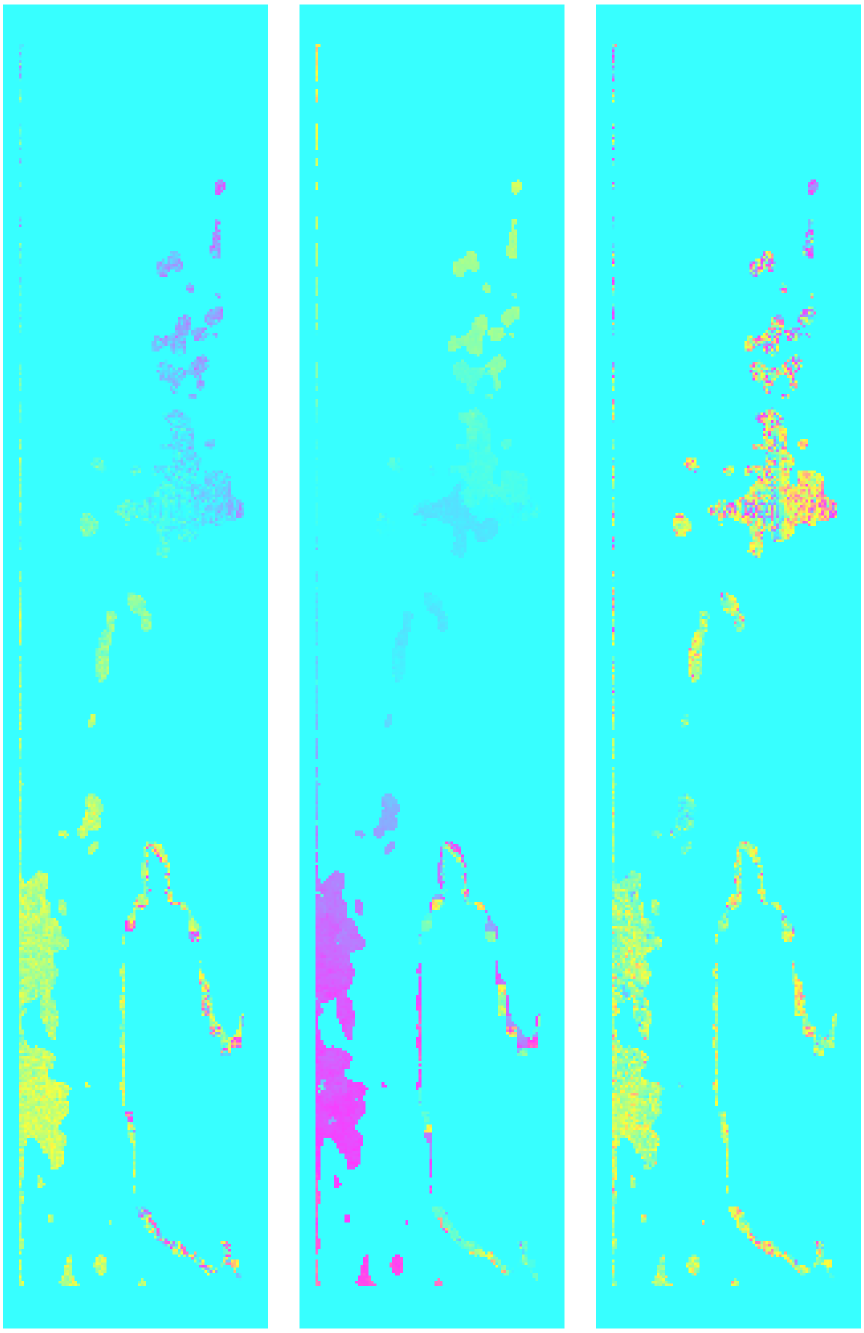

a b c

Figure 12.18: Deformation velocity average within the selected interferograms computed with the wrapped phase (a), deformation velocity average computed with the wrapped phase (b) and temporal standard deviation computed with the wrapped phase (c) for the Košťany crop. The colorscale is imaged in figure 12.14 and the range is: $(-0.1; 0.1)$ for (a), $(-1; 1)$ for (b) (some points at the lake border are out of range in both cases) and $(0; 2)$ for (c). However, there are only 18 points (not spatially continuous) in the crop for which the absolute value of the deformation velocity average is higher than three times its standard deviation. This means that the area is stable by the first approximation.

Chapter 13

Processing Procedure

Data processing has two parts: first, data received from ESA are processed in GAMMA software in order to produce interferograms, subtract the flat-Earth phase and the phase corresponding to topography and unwrap the results, and then the resulting data are processed in MATLAB in order to compute the temporal development of the deformations. The processing procedure is described in detail in the following text.

13.1 Interferometric processing

The first processing step is to read the data from the CDs received from ESA and to substitute the approximate orbits by the precise ones, downloaded from [27]. This is performed by commands `par_ESA_ERS`, `DELFT_orb_SLC` and `DELFT_vec`.

Each pixel of all interferograms must correspond to the same point in reality. During interferogram processing, coregistration with a subpixel precision is performed, but coregistration of all scenes with regard to one of them (*master*) is neccessary. Coregistration during interferogram creation has the disadvantage that it does not allow to create interferograms between two non-master (*slave*) scenes. In addition, coregistrating small crops of the scene is not always successful because of lack of data.

Therefore the following procedure is applied:

1. All scenes are coregistered with regard to the selected master. Magnitude data are used for quantification of the similarity of the two scenes. Coregistration of the whole scenes allows to take advantage of all the magnitude data. This is performed in the GAMMA software using the `offset_pwr` and `SLC_interp` commands. During coregistration, spectral filtering is performed as described in Chapter 5.

2. The coregistered scenes are cropped in order to perform further processing only for the area of interest. This is performed using the `SLC_copy` command.

3. Interferograms are created. Each scene is paired with every other scene and coregistration is no more performed (the `SLC_intf` command).

4. Flat-Earth phase is subtracted using precise-orbit data (the `base_init` and `ph_slope_base` commands).

5. Coherence is computed using the complex values of the coregistered scenes (the `cc_wave` command).

6. The phase corresponding to the topography is subtracted. First, geocoding lookup table of the interferogram (with regard to the DEM) is created using the `gc_map` command. Second, this lookup table is used for conversion of the DEM into SAR coordinates (the `geocode` command). Then, the simulated phase is computed (`phase_sim`), using precise orbits and the converted DEM. Finally, the simulated phase is subtracted from the flattened interferogram (the `sub_phase` command). The resulting phase should contain only the deformation signal.

   It is recommended to perform coregistration between the interferogram (i.e. its magnitude) and the magnitude corresponding to the topography (computed using the DEM), but we omit this step, considering it unneccessary. The same DEM is used for topography reduction of all interferograms, and the position error was smaller than one pixel.

   SRTM DEM [28] is used for topography phase subtraction.

7. The resulting phase is filtered (`adf` command) in order to improve spatial continuity and reduce the number of phase errors. Filtering is performed on the basis of a local fringe frequency, in order not to filter out the high-frequency component of the phase (which is usually not neccessary if filtering topography-subtracted interferogram). More details about the algorithm may be found in [12].

8. The deformation phase is unwrapped. The following commands are used: `corr_flag` for creating the tree branches to be avoided during phase unwrapping using coherence data (areas with coherence lower than 0.3 are avoided), `neutron` uses the intensity information and allows the following script to avoid areas of layover, shadow etc., generating branch trees, and `grasses` for phase unwrapping with the generated branch trees. The reference point is entered as the unwrapping seed, so that this point always has a value in the unwrapped phase file.

9. Due to the fact that the GAMMA software works in big-endian representation and the following processing is performed on a little-endian computer, the data are byteswapped (using home-made `byteswap-float` script).

10. The baseline file, created using the `base_init` command in step 4, contains the baseline and its change rate in the TCN system (the radial, tangential and cross-track components). Using the command `base_perp`, the baseline is converted to the perpendicular-parallel system, with regard to the radar ray direction. This is then used for the estimation of the DEM error, as described in section 8.8.

The following processing is performed in MATLAB, GAMMA software is only used for displaying the results.

13.2 Data selection for processing

As already noted, the interferograms are incoherent on most of their area. On the other hand, the area of interest, i.e. a road or a village, is usually coherent (though not in all interferograms). The problem is now: how to select the interferograms to be processed, and how to select individual pixels?

Unexpectedly, the problems are solved in the reverse order.

13.2.1 Pixel selection

For pixel selection, the mean coherence throughout the interferograms for each pixel is computed. In the resulting map (see figure 13.1 (a) or 13.2 (a)), the most coherent features are obvious. A coherence threshold is found manually and determines pixels to be processed (see figure 13.1 (b) or 13.2 (b)). Threshold for both crops can be found in tables 14.1 and 14.2.

However, before thresholding the mean coherence map must be low-pass filtered in order to eliminate the noise – within the noisy areas, some pixels with higher coherence may appear. Also, the image borders with higher coherence (originating probably from the fact that smaller area is used for coherence computation) must be eliminated – this is performed manually. One can see that only a small number of pixels out of the area of interest are processed.

13.2.2 Interferogram selection

Theoretically, the best result would be obtained if all interferograms were processed. However, the number of interferograms of 552 and the size of the processed area (required to be implemented into a MATLAB array) would mean a very long time for processing, higher probability of getting stuck in a local minimum, and even the eventuality of impossible processing due to the limited memory size (the limit is 2 GB on most computers due to the 32-bit architecture).

During previous processing attempts, we found the optimal number of interferograms processed to be about 100. Of course, the most coherent interferograms are to be selected – but manual selection is very subjective, although it regards the fact that all scenes are present in the processed interferogram (which is not the case of our technique).

We tried three ways of selecting interferograms to be processed:

- The number of "coherent" points within the selected pixels. The term "coherent" means here only that a coherence of the point is required to be above a predefined threshold. More coherence thresholds have been selected – the histogram of the computed number of coherent points may be seen in figure 13.3.
- Phase standard deviation within the selected pixels. The histogram of phase standard deviation can be seen in figure 13.4. This aproach causes interferograms with a low-pass trend (e.g. due to an orbit error) to be less applicable. This feature may be both the advantage and the disadvantage. The trends in the interferograms are an artifact, causing higher residues and therefore higher standard deviations – however, each interferogram has some trend due to the fact that the orbits

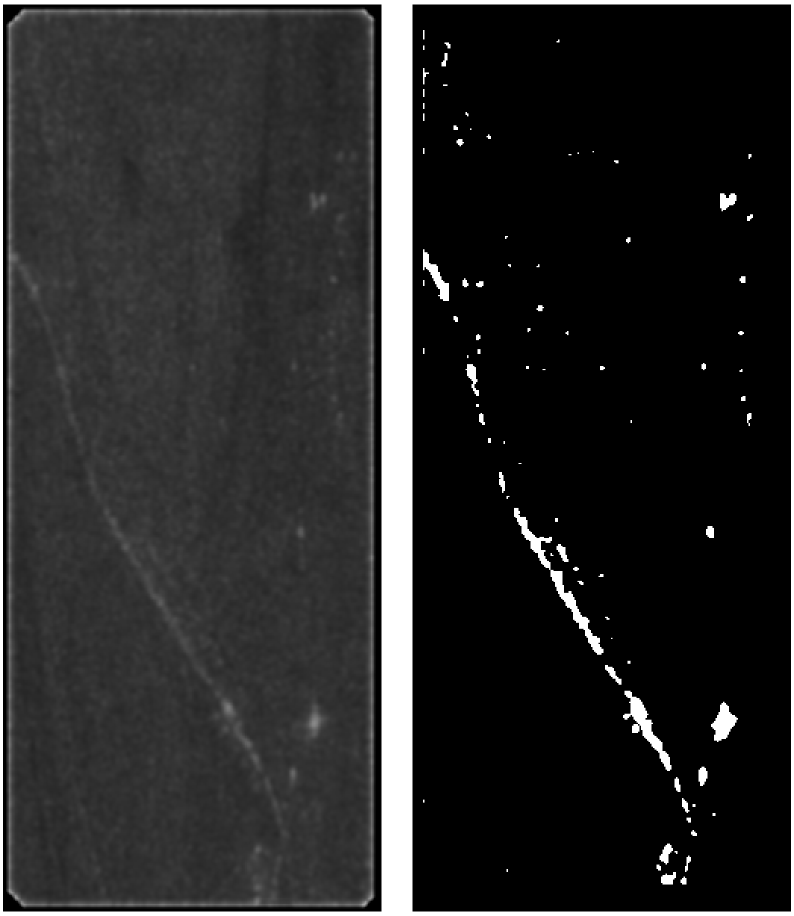

a b

Figure 13.1: Filtered mean coherence of each point (a) and its thresholding with 0.3 (b) for the Ervěnice area. The coherent interferogram borders were eliminated manually.

are never exactly precise – and determining a level of "acceptable" trend is a sensitive question. On the other hand, it is not easy to compute the phase standard deviation from the wrapped phase (and it is even less reasonable to compute the phase standard deviaton for the unwraped phase due to possible unwrapping errors which do not predicate the phase stability) because of the wrapped nature of the phase – and some interferograms, which may be quite good as phase stability is concerned, may get a high phase standard deviation. In addition, this method assumes that interferograms containing deformations within the selected pixels are discriminated.

- Mean coherence within the selected pixels. The histogram of the mean coherence can be found in figure 13.5.

Unfortunately, all histograms have only one local maximum, making it impossible to select the threshold automatically or reliably. Therefore, we decided to choose the threshold on the basis of the desired number of interferograms for processing (please also note that some interferograms cannot be unwrapped due to the incoherence of the unwrapping seed – these may not be taken into account).

Finally, the mean-coherence approach was selected, because of its better reproduction – the threshold may be easily compared with the coherence threshold used during area selection. It is required to be higher than the previous threshold – the incoherent pixels are not involved into this evaluation.

The actual thresholds used for processing can be found in tables 14.1 and 14.2.

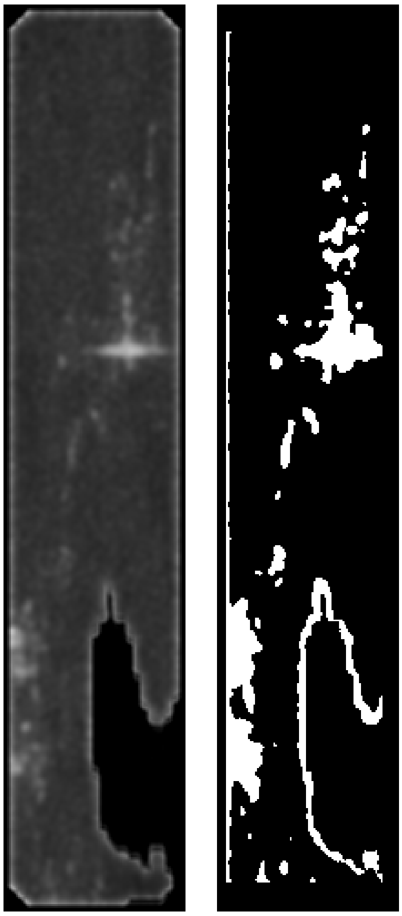

a b

Figure 13.2: Filtered mean coherence of each point (a) and its thresholding with 0.3 (b) for the Košťany area. The coherent interferogram borders were eliminated manually except for the border of the Barbora Lake (bottom right).

13.3 DEM error correction

Before further processing, DEM error correction is performed. It is not involved in the adjustment step, as suggested in section 8.8, because adjustment like this was very problematic due to the unwrapping errors – the estimated DEM error was in the order of kilometers in some cases. We therefore decided to estimate the DEM error separately using only tandem pairs, where no deformation is expected, and due to the insufficient number of coherent tandem interferograms, also tandem interferograms from a different track were used, as described in section 12.3.

Now, the phase of all interferograms is corrected with regard to the estimated DEM error and the perpendicular baseline figured out for each interferogram (using the `base_perp` script). The baseline variations within the interferogram are neglected, as evaluated in paragraph 12.3.3. The maximum phase correction within the stack was a little larger than 2π, and we therefore consider the phase correction to be adviced to be performed before referencing, due to the fact that it can easify finding the unwrapping errors during the following process.

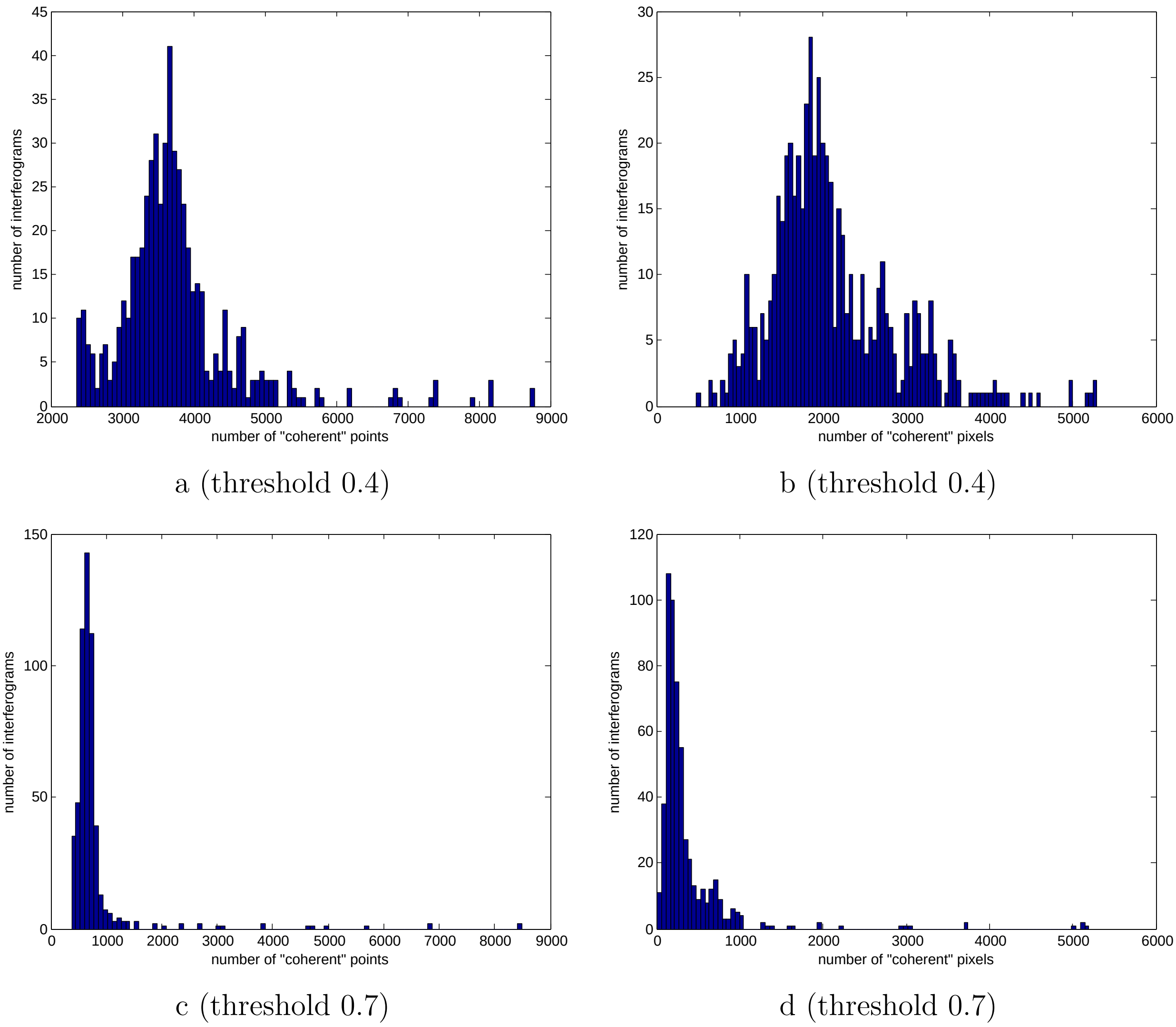

Figure 13.3: The histogram of the computed number of coherent points in an interferogram within the previously selected points for Ervěnice (a,c) and Košťany (b,d) areas.

As suggested in [2], the phase should be reunwrapped after correcting the phase for the DEM errors. However, this is contraproductive in our case, because phase unwrapping should be performed for the whole interferogram (2D array), while the DEM error was only estimated for a small number of points which are not neccessarily spatially continuous. Phase unwrapping in an array, where a part is corrected for DEM errors, and a part is not, would probably produce even more unwrapping errors than if this post-correction unwrapping is not performed at all.

13.4 Referencing to a single point

The first thing to be performed with the inteferograms is their referencing. The reason is that a single interferogram phase is assumed to be influenced by more error sources than

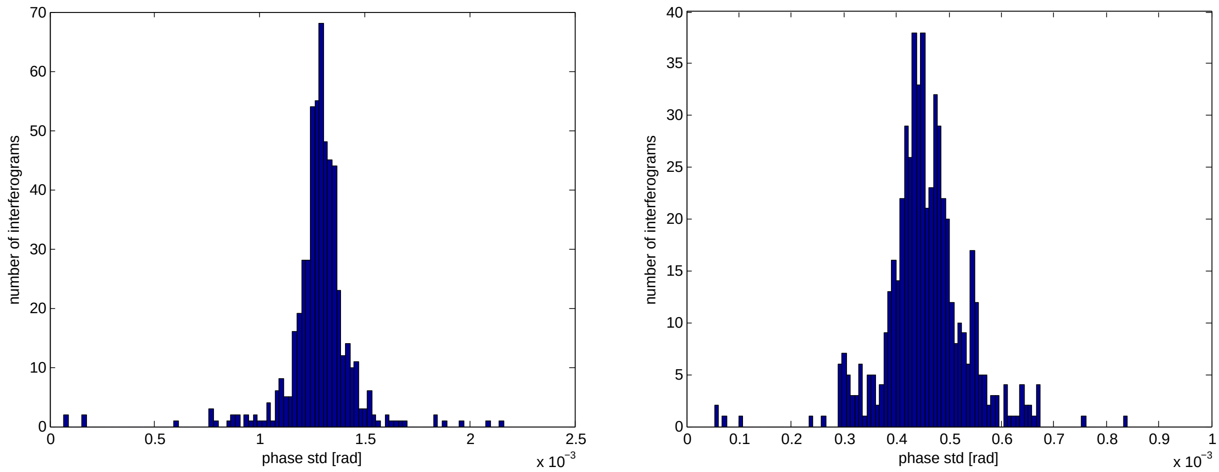

a b

Figure 13.4: The histogram of the phase standard deviation computed for each interferogram within the previously selected most-coherent pixels for Ervěnice (a) and Košťany (b) areas.

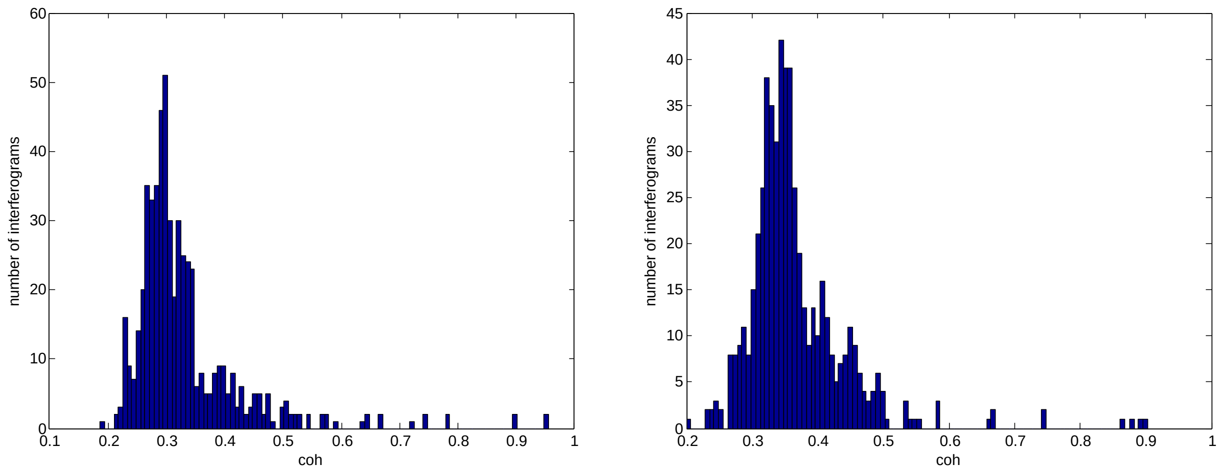

a b

Figure 13.5: The histogram of the mean coherence computed for each interferogram within the previously selected most-coherent pixels for Ervěnice (a) and Košťany (b) areas.

a difference bettwen two points in an interferogram. For example, atmospheric delay or orbit errors do change very slowly in space, and therefore may be approximated by a constant in first approximation, or by a plane in the second one.

13.4.1 Requirement for the reference point

It is expected that this point is as close as possible to the area where deformations are mapped and the area between the mapped region and the reference point is expected to be correlated in order to allow for the best possible phase unwrapping.

Ideally, the reference point should be stable, should not be subject to ground deformation. Due to the relativity of the interferometric measurements, the requirement of stability of the reference point allows to expect that the adjusted results directly correspond to the occured deformations. On the other hand, if the reference point is not stable – and the computations need a reference point – the computed results are relative with respect to the reference point and the deformations of the reference point must be computed using an information from a different source.

However, in our case it is irreliable to assume a point of the cropped areas to be stable, and therefore we dropped the stability requirement. In addition, the reference point cannot be selected after interferometric processing due to the fact that the reference point is used as the initial seed in the phase unwrapping process (see Chapter 7). Therefore, the reference point was selected manually as one of the points which are coherent throughout most of the interferograms. In addition, the interferograms where the coherence of this point is lower than a threshold (0.3) specified within the unwrapping procedure, are not unwrapped at all. However, the threshold for exclusion of interferograms due to a low coherence of the reference point, used during the postprocessing step, is higher (0.4).

13.4.2 Ways of referencing

The first possibility is to reference the whole interferogram with regard to a single (stable) point. However, the phase of this point may be imprecise due to decorrelation. In this case, this point is assumed to be stable - if it is not, it must be taken into account after adjustment when results are referenced back to absolute values (using e.g. in-situ measurements).

Another possibility, suggested in [36], is to compute the reference phase out of a small neighbourhood of this point (e.g. 3 by 3), using an average or weighted average (unwrapped phase is required, even if the adjustment is performed using wrapped phase). Here, the decorrelation errors are assumed to be three times smaller, assuming non-weighted average and the same phase accuracy of all involved points.

Another possibility is to compute the reference phase as a mean of all points in the interferogram, selected for further processing. Here, the phase must be unwrapped, too, and the result is largely influenced by unwrapping errors which are large far away from the unwrapping seed. If referencing is performed in this way, the average of the area is assumed to be stable, which influences back-referencing process of the adjustment results.

Referencing of the interferograms is a crucial step in order to fill the sum conditions (8.17), (8.18). All referencing errors are projected into the phase sums and this causes both higher adjustment residues and higher estimation of phase standard deviation.

It is possible to compute the sums of two or three referencing constants, for the (wrapped) phase sums have typically a significant histogram maxima and a small disperse. However, out of the reference sums, we did not find a way to compute the referencing constant for each interferograms, due to a high rank deficit of the matrix C (see e.g. equation (8.19)). Even if the matrix is decomposed into separated "diagonal" blocks, the rank deficit of the largerst block was still almost 20 (out of around 90). We did not find a way how to separate the block of referencing constants, which can be computed (if a referencing constant of one or two interferograms is assumed to be estimated correctly) from the others.

We measure the "correctness" of referencing constants by computing the (wrapped) phase sums s for one cycle and for all the appropriate points. The "correct" value is known - it is zero. Therefore

$$\sigma_{cyc,i} = \sqrt{\frac{\sum_j s_{ij}^2}{n}}, \tag{13.1}$$

where n is the number of valid points (indexed as j) in the two or three interferograms and i is the cycle ID. This is computed for all cycles. Then,

$$\sigma_{cyc,i,intf} = \frac{\sigma_{cyc,i}}{\sqrt{N_i}}, \tag{13.2}$$

where N_i is the number of interferograms involved in cycle i. The final phase standard deviation given by referencing is then computed as

$$\sigma_{ref} = \sqrt{\frac{\sum_i \sigma_{cyc,i,intf}^2}{N_{cyc}}}, \tag{13.3}$$

where N_{cyc} is the number of cycles. Please note that this standard deviation is directly independent from coherence and therefore, it is to be quadratically summed with the phase standard deviation evaluated from coherence in formula (6.8).

Before the description of the method we finally used for referencing, let us sketch here the values of σ_{ref} we got when using different referencing procedures:

- with no referencing, we get $\sigma_{ref} = 0.75$ rad,
- using phase of the unwrapping seed for referencing, we get $\sigma_{ref} = 0.54$ rad,
- using the phase average of the 3-by-3 neighbourhood of the unwrapping seed for referencing, we get $\sigma_{ref} = 0.58$ rad,
- using complex average of the interferogram for referencing (complex average is computed iteratively as a sum of shifts in each steps; in each step, the phases of all points are shifted so that their average is zero), we get $\sigma_{ref} = 0.78$ rad,
- using (unwrapped) average of the interferogram for referencing, we get $\sigma_{ref} = 0.72$ rad,
- using the SVD technique for solving the singular system of equations (having the referencing constants sums), $\sigma_{ref} = 0.67$ rad.

The values are only informative and were computed for the Ervěnice crop. We can now assume that the only reasonable ways are referencing to a single point or to its small neighbourhood. However, manually analyzing the values of $\sigma_{cyc,i,intf}$, we were able to exclude some interferograms and get the final standard deviation down to $\sigma_{ref} = 0.47$ rad. The procedure is described below.

13.4.3 Excluding interferograms on the basis of high phase sums

First, let us note that the process of exclusion of interferograms is not based on a statistical theory, it is performed manually and the moment where the exclusion is stopped, is also determined manually.

Out of the list of $\sigma_{cyc,i,intf}$, we take out the cycles with largest values, and make a list of interferograms which are involved in these cycles. We found out that mostly, if there is a double of interferograms (interferograms AB and BA), and one of them is wrong referenced, so is probably the other. Therefore, instead of excluding the interferogram which is contained in our list the most times, we try to figure out the doubles and exclude - if possible - only one interferogram from each cycle.

In the Ervěnice area, we excluded only 6 interferograms and the value of σ_{ref} got down to 0.47 rad from 0.54 rad. We stopped the process of exclusion due to the fact that there was a step between the last excluded cycle and the following worse cycle of more than 0.1 rad in $\sigma_{cyc,i,intf}$.

However, the precision of the reference point (if only one point is used) is the same as for the other points, and therefore the precision of the referenced phase is worsened by $\sqrt{2}$.

13.5 Interferogram consistency check

As relations (8.17) and (8.18) apply for each non-noisy point (or apply approximately for a little-noisy points) when the phase is only flat-Earth and topography subtracted and referenced to a single point, they must also apply for the unwrapped phase where there are no unwrapping errors. First, let us use these relations for recognizing (and excluding) the noisy points. The process consists of two steps:

- All 2-cycles and 3-cycles are found within the processed interferograms. A matrix C (used e.g. in (8.19)) is constructed in this step: the number of columns corresponds to the number of interferograms, and the number of lines corresponds to the number of cycles. Each line contains three non-zero elements: 1 means that the phase of the interferograms must be added, -1 means that the phase must be subtracted in order to give 0.

- For each selected point, the unwrapped phase is checked for noise. The difference between the left-hand side of equations (8.17), resp. (8.18), and an integer multiple of 2π is allowed to be less than $\pm 2\sqrt{2}\sigma_{\Delta\varphi,ref}$, resp. $\pm 2\sqrt{3}\sigma_{\Delta\varphi,ref}$, considering the phase standard deviation to be given by (8.22), although the interferogram phases are not independent.

  Stefania Usai in her article [37] notes that she corrects the referencing errors on the basis of cycle sums; however she does not describe her approach in detail. That leads us to the idea that in her case, only few interferograms are biased and need a correction, which is not our case. She uses the histogram maximum as the correct reference cycle sum, not its mean – on the other hand, due to a very strong maximum, we suppose both methods would bring very similar results.

  Some interferogram doubles and triples are then considered bad, and only the interferograms contained in at least one good cycle, are considered OK. The bad cycles and interferograms are not processed any more and do not enter the adjustment. The causes of the non-zero phase sums are described in section 12.2.

That also means that isolated interferograms, i.e. interferograms which cannot be grouped to a double or triple, are excluded.

Please note that such an exclusion is performed for a single point.

13.6 Iterative adjustment

Due to the nonlinear nature of the problem (see section 8.9) and the risk of getting stuck in a local minimum, the problem is solved iteratively. The basic steps performed during the process (possibly multiple times) are listed below:

- Point selection (`point_sel`). Please note that the unwrapping errors are found for each point individually, but together for all interferograms in the stack.

  Due to the terrain and large decorrelated areas, we can say that the unwrapping error is not constant for the whole interferogram, nor for large areas of it, but it is assumed to change slowly. Therefore, for evaluation of the unwrapping errors of a particular point, we use the (already evaluated) unwrapping errors of the neighbouring points.

  Therefore, the point selection algorithm is to maximize the number of already-computed neighbours. The starting point is the reference point (see section 13.4), which is the unwrapping seed. Here, the unwrapping errors are assumed to be zero, such as the phase values themselves.

  Then, the points are selected according to the scheme drafted in figure 13.6. If an edge of the scene is encountered, the scheme remains the same, but the "non-scene" points are not evaluated.

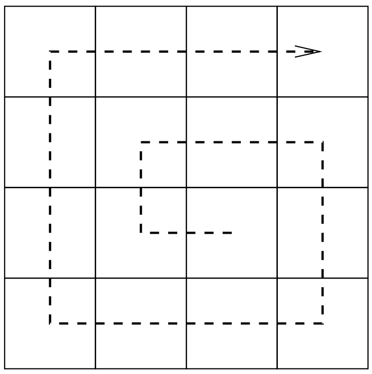

Figure 13.6: The scheme of selecting points.

- Initial estimation and correction of phase-unwrapping errors (`init`). As described in Chapter 7, the process of phase unwrapping is irreliable and errorneous, especially in forested, mountaineous or agricultural areas and in interferograms with longer temporal or spatial baselines where the coherence is lower. However, the phase unwrapping errors are always integer multiples of 2π which makes the errors potentially easily recognizable.

The initial estimation of the unwrapping errors is based on the unwrapping errors of the neighbours (only those which were already processed). Due to the fact that the processed points are not always spatially continuous (and some points may have been excluded during coherence thresholding and consistency check (see section 13.5)), we also consider more distant points – the scheme is illustrated in figure 13.7. First, the points of level 1 are selected and the corrected phases are averaged – and the points of each of the following levels are selected only in the case if the previous levels contained no processed points. In other words, only points from a single level are averaged and no weights are introduced.

5	4	3	4	5
4	2	1	2	4
3	1	■	1	3
4	2	1	2	4
5	4	3	4	5

Figure 13.7: An approximate neighbourhood scheme. The actual neighbourhood width is 8 (here 5).

- Adjustment according to one of the models described in Chapter 8 (`adj`). The results are then the unique standard deviation m_0 and adjustment residues r according to formula (8.15), together with the adjusted deformations and their standard deviations. The unique standard deviation m_0 is expressed as

$$m_0 = \sqrt{\frac{r^T r}{l}}, \tag{13.4}$$

where l is the number of degrees of freedom (i.e. the difference between the number of interferograms and the number of unknows). Please note that no weights are introduced. In this step, the statistical tests are performed too (see section 13.9).

Details for adjustment using different models from Chapter 8 are discussed in section 13.8.

- Estimation of the phase unwrapping errors on the basis of adjustment residues (`corr_res (n)`) where n is the number of unwrapping errors to be adjusted). Parameter n changes during the iterative adjustment process. n unwrapped phases are adjusted which have the highest residues – the adjustment size is the negative value of the residue rounded to the closest multiple of 2π.

- Getting the system out of local minima (`release`). A minimum is recognized if none of the previously described steps changed the estimated unwrapping errors, and therefore the unique standard deviation did not change. This happens if all residues are smaller than 2π and indicates the solution is almost optimal – however, there is no way to distinguish the really optimal solution from the suboptimal ones. Therefore, we try out a certain number of solutions and select the one with the smallest unique standard deviation m_0.

  Please note that we search the space of ambiguities (or unwrapping errors), but the search is not complete. First, the number of possible unwrapping errors is infinite (but countable), and second, the number of attempts is limited due to a very large space, as mentioned in section 8.9.

  However, this step is only performed if the cycle condition (8.19) is not fulfilled. If it is, no change in the release step is possible due to the implemented algorithm.

  A detailed description of the procedure of getting the system out of local minima may be found in section 13.7.

The scheme of performing these steps for each point is illustrated in figure 13.8. The scheme also contains procedures `update` and `downdate` which allow us to have two sets of variables: the current optima and working variables which are used for all adjustments as attempts. Let us note here that except for the last part of the process (containing the `release` step), all steps are performed with the working variables. The step `update` then means that the working variables are set to be the current optima and the `downdate` step means that current optima are set to be working variables (i.e. the current working variables are discarded).

13.7 Getting the system out of local minima

As already mentioned, the system of equations is nonlinear and tends to get stuck in a local minimum. It is no way how to guarantee that the right solution was found if we do not search the whole ambiguity (unwrapping error) space. In addition, this ambiguity space is not finite due to the integer nature of ambiguities, and although high unwrapping errors (or their differences within a small neighbourhood) are less probable, such a limitation would be artificial.

We therefore decided to use a heuristic approach in order to reach fulfillment of both conditions specified in section 8.9. First, we compute the vector of cycle residues r_{amb} (meaning of the symbols is the same as in formula (8.19))

$$r_{amb} = C \cdot u \tag{13.5}$$

which indicates whether condition (8.19) is fulfilled or not. Typically, it is not, because as shown in the scheme in figure 13.8, the fulfillment of the condition was not applied at all during the iteration process. The vector r_{amb} indicates an error in each cycle and now, we are to transfer it into interferograms, i.e. each interferogram is to be attributed an estimation of its error.

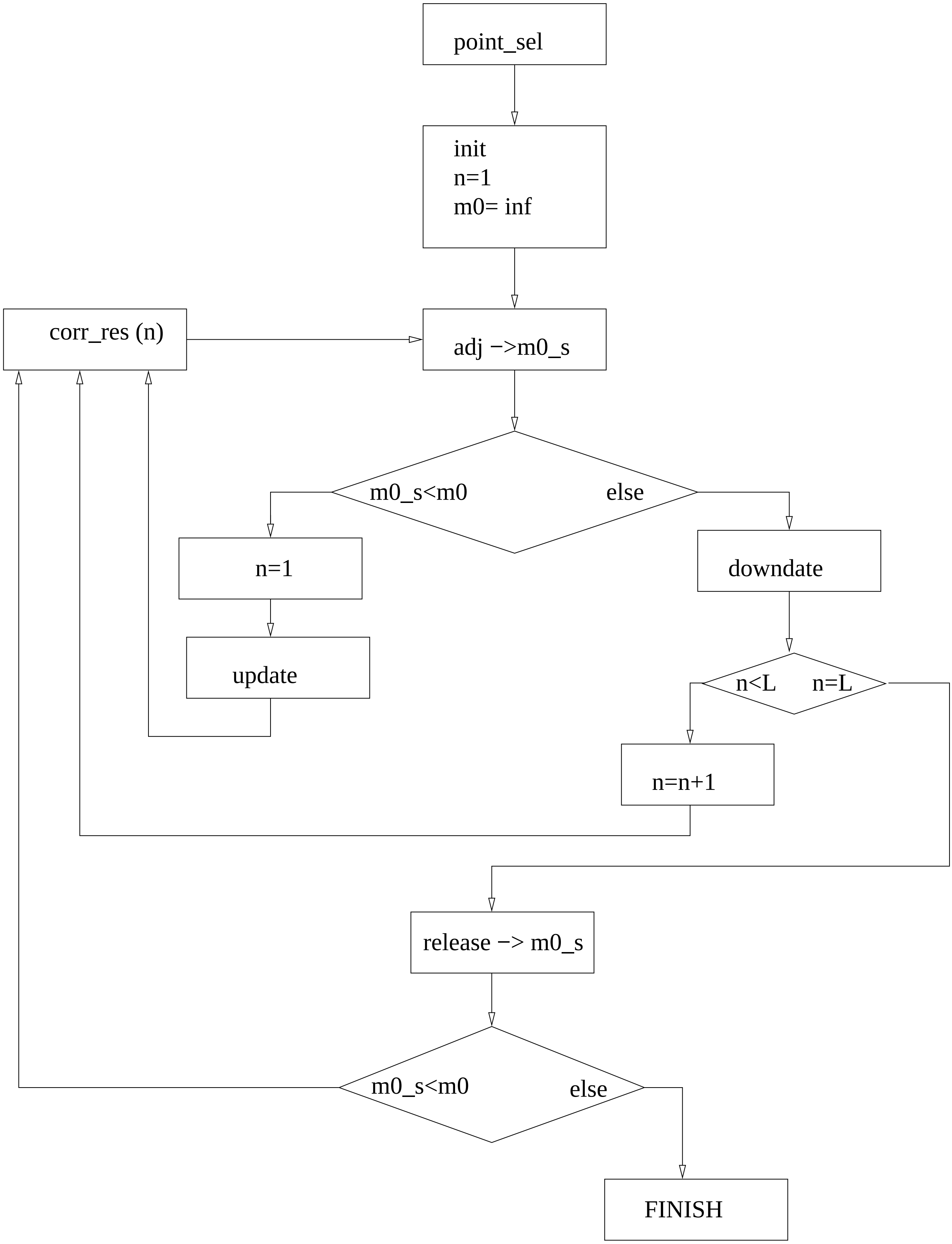

Figure 13.8: The scheme of the iteration process. The constant L here means the number of interferograms processed.

This value is estimated as a mean (within the valid cycles) of all cycles where the particular interferogram participates.

Then, the estimated error of the interferogram is multiplied by the residue for each interferogram. The interferogram for which this value is highest, is corrected by one phase cycle (2π) in the appropriate direction – according to the residue. Please note that all "computations" in this step are approximate – this step is only performed if applying `corr_res` step iteratively did not change anything (see figure 13.8), i.e. all residues were smaller than π.

A new 'solution' is found this way and it is completely evaluated – i.e. the adjustment is performed, adjustment residues are computed, as well as ambiguity residues (r_{amb}). If this solution is better (according to m_0) than all of the previous ones, it is used for evaluation of another solution etc. However, the number of solutions to be looked for is limited in a cycle of the `release` step, but, as can be seen in the scheme in figure 13.8, the `release` step can be performed more times if a better solution was found than before. However, the set of solutions, together with the information about what solutions have been tried, is saved for another iteration.

Finally, only the solutions with zero r_{amb} are selected as the output from the `release` step.

However, if a solution with smallest m_0 has zero r_{amb}, this step has no possibility to continue.

13.8 Adjustment

13.8.1 Deformation model

As mentioned in section 8.4, A^TA (or $A_{aux}^TA_{aux}$; A or A_{aux} are the design matrices) is singular and one column has to be taken out of A in order to regularize it. Let us call the scene, which the column corresponds to, the reference scene. By definition, all deformations are zero at its time of acquisition.

As already mentioned, the deformation model may be underdetermined in some cases. This is caused by possible exclusion of some interferograms during the unwrapping error check process – some scenes may get lost from the system or the scenes may be in more separate sets. In order for the adjustment to be possible, the design matrix A_{aux} (as specified in section 8.4) must be adapted in order not to contain the excluded interferograms, as well as not to contain columns containing only zeros (excluded scenes). Similarly, the vector of interferogram phases must be adapted, as well as the adjusted deformation vector must be adapted back to correspond to the whole system - the excluded scenes may be different for each point. For those non-adjusted points and interferograms, we use the NaN value.

However, it is senseless to select a different reference scene for each point (in order to allow the maximum number of adjusted deformation): the results would be inconsistent. Therefore, the reference scene must be selected carefully in order to make as many as possible coherent interferograms. Then, the set of scenes to be adjusted always contains the reference scene and the other sets (possible more than one) cannot be computed. We select scene 9767 as the reference scene for the Ervěnice area and 11771 for the Košťany area.

13.8.2 Changing-velocity model

In the velocity model, the problem of separate scene sets is solved by the SVD technique, as described in section 8.7, together with two significant disadvantages of this method, which are the higher standard deviations at the end of the deformation series, and the possibility of atmospheric delay influencing a lot of adjusted deformations. On the other hand, the deformations are better sampled in time.

However, the resulting deformations cannot be temporally filtered for the atmospheric disturbances due to the fact that some of them are really adjusted and some of them are estimated (the velocities are minimized) by the SVD method.

We use the scene 23428 as the reference one for both crops.

13.9 Reliability of the results, statistical tests

The accuracy of the results (i.e. deformations at the times of acquistion, resp. deformation speed) depends on many factors. First, let us mention the random phase noise, which also influenced the previous processing and caused some interferograms to be excluded from the adjustment.

A priori, we consider the area (all pixels of the interferograms) to be stable. The null hypothesis of the stability may be disclaimed with some criteria. The first way suggested is to filter out the deformations which are smaller than a multiple of their standard deviation.

On the other hand, we can use the regular approach: we reject the hypothesis of the reliability of the adjustment model with respect to statistical tests.

We tried two ways to filter out the irreliable results:

- As suggested in [37], the adjustment residues were tested if they are normally distributed with the a priori precision. The a posteriori standard deviation and the a priori standard deviation are compared and tested. Here, only the standard deviation is tested, not the normality.

- The residues are tested for normality using the Kolmogorov-Smirnov test, as implemented in MATLAB in the `kstest` command. Here, the residues are required to be normally distributed with zero mean and unique standard deviation.

Both statistical tests are performed on confidence level of 5 % and in detail discussed below.

13.9.1 Snedecorov-Fischer distribution

In accord with [13], let us have two independent variables y_1 and y_2 with distributions $\chi^2(n_1)$ and $\chi^2(n_2)$, where n_1 and n_2 are degrees of freedom of the respective distributions.

Their ratio

$$F = \frac{\frac{y_1}{n_1}}{\frac{y_2}{n_2}}, \tag{13.6}$$

has then Snedecorov-Fischer distribution $F(n_1, n_2)$.

We need to compare the a priori and a posteriori standard deviations. Here, in order to set the same value for all of the a priori phase standard deviation, we use the value of $\sigma_{\Delta\varphi} = \frac{2}{10}\pi$, while the a posteriori phase standard deviation can be computed from the adjustment residues.

Let us now consider the phase residues are normally distributed with zero mean. We then substitute

$$\frac{y_2}{n_2} = \sigma^2_{\Delta\varphi,ref}, \tag{13.7}$$

with $n_2 = \infty$, and

$$y_1 = s^T s, \tag{13.8}$$

where s are the adjustment residues. Here, n_2 is the number of redundant interferograms.

The value F is then compared to $F_\alpha(n_1, n_2)$, known from the Snedecorov-Fischer distribution, and if $F > F_\alpha$, then the hypothesis of a reliable result is rejected with the confidence level α.

Numerically, MATLAB is unable to compute a reasonable value of F_α for $n_2 = \infty$. In our case (low values of n_1), we can substitute it by $n_2 = 1000$ (the value then differs at the third decimal position).

13.9.2 Kolmogorov-Smirnov test

The Kolmogorov-Smirnov test allows to test if a data set belongs to a certain distribution. In our case, we test if the data set of $\frac{s}{\sigma_{\Delta\varphi,ref}}$ has the normal distribution N(0,1). In comparison to the Fischer test described above, this one does not only test the standard deviation, but also the normality of the residues. This test is described in detail in the MATLAB help.

13.10 Geocoding

In the topography subtraction step, the lookup table converting map to SAR coordinates, was created. As already noted, GAMMA allows to coregister the DEM with the SAR magnitude, but this process was not successful in our case – the areas are too small and artificial objects are more clear in the magnitude image. However, trying to geocode the whole scene, we found out that the difference between the DEM and interferogram is less than a pixel. We therefore consider geocoding to be precise enough.

The last step is the conversion of the computed velocity or deformation maps into map coordinates. It is performed with regard to the DEM processed in the topography subtraction step, and therefore the coordinates are in the same system, i.e. WGS-84. In GAMMA, the script to perform the conversion is called `geocode_back`.

Chapter 14

Results

Finally, we decided to perform the processing with both wrapped and unwrapped data. Theoretically, the adjustment is to be performed only with the unwrapped data – however, our algorithms allows to correct for small unwrapping errors, and the unwrapping errors produced by the classical algorithm (described in Chapter 7) seem to be large due to low coherence of the region, especially of those pixels which were not included in processing. On the other hand, our approach to unwrapping error correction allows to take into account also the third dimension – time. On the other hand, the spatial continuity is not guaranteed (unlike in the classical algorithm), it is only supported by the `init` step.

Due to the fact that some interferograms could not be unwrapped by the classical method, and therefore these interferograms are not available for processing using unwrapped data, the properties of the processed data (such as number of interferograms, standard deviation computed from the cycle conditions (see section 12.2)) are different for the wrapped and unwrapped case. See tables 14.1 and 14.2 for details.

This chapter contains only some results - one scene for each crop, for both the deformation and velocity model, and for both the wrapped and unwrapped phase used. All results computed using the deformation model can be found in appendix B, results computed using the velocity model cannot be found in this thesis at all, due to the fact that the velocity model did not give a solution sufficiently reliable (compare the number of points excluded by the statistical test in tables 14.1, 14.2 – the number of validated points was lower than 10). In addition, using the velocity model, we did not even achieved to fulfill the cycle conditions (8.17), (8.18), except for a few of the first points computed – the points nearest to the reference point. Please also compare the value of the unique standard deviation for both models in figures 14.6 and 14.12.

Figure 14.1: Colorscale. The left and right borders are defined individually for each image.

	wrapped	**unwrapped**
pixel selection coher. threshold	0.3	0.3
interferogram selection coher. threshold	0.35	0.34
number of selected interferograms	122	124
number of intfs after exclusion 25432	112	113
selected points	3028	3028
crop size (lines x pixels)	600 x 250	600 x 250
other interferogram doubles excluded	12773 - 15779 12773 - 16280 5759 - 9767 5759 - 25933 14777 - 16280 24430 - 25933 10268 - 16280 9767 - 14777 24430 - 5759 12773 - 14777 11771 - 14777	5759 - 10268 5759 - 25933 4757 - 9767
std. dev. computed from phase cycles [rad]	0.53	0.47
standard deviation total [rad]	0.83	0.79
threshold for exclusion of a pixel due to high phase sum error [rad]	2 x 0.53 x $\sqrt{2}$ ($\sqrt{3}$)	2 x 0.47 x $\sqrt{2}$ ($\sqrt{3}$)
total selected pixels	272,520 (90 x 3028)	323,996 (107 x 3028)
low coherence points to be excluded	116	29,211
points excluded during cons. check	57	787
total points entering adjustment	272,347	293,998
points excl. by the Kolm. test (defo model)	1287	1372
points excl. by the Fischer test (defo model)	1789	1235
points excl. by the Kolm. test (c-vel model)	3021	3009
points excl. by the Fischer test (c-vel model)	3021	3012

Table 14.1: Basic processing data about the Ervěnice area (both wrapped and unwrapped case).

	wrapped	**unwrapped**
pixel selection coher. threshold	0.3	0.3
interferogram selection coher. threshold	0.4	0.4
number of selected interferograms	129	120
number of intfs after exclusion 25432	123	114
selected points	5408	5408
crop size (lines x pixels)	500 x 100	500 x 100
other interferogram doubles excluded	5759 - 9767	5759 - 9767
std. dev. computed from phase cycles [rad]	0.41	0.42
standard deviation total [rad]	0.76	0.76
threshold for exclusion of a pixel due to high phase sum error [rad]	2 x 0.41 x $\sqrt{2}$ ($\sqrt{3}$)	2 x 0.42 x $\sqrt{2}$ ($\sqrt{3}$)
total selected pixels	654,368 (121 x 5408)	605,696 (112 x 5408)
low coherence points to be excluded	161,606	202,532
points excluded during cons. check	9.061	11.475
total points entering adjustment	483,701	391,689
points excl. by the Kolm. test (defo model)	4670	4223
points excl. by the Fischer test (defo model)	1699	2077
points excl. by the Kolm. test (c-vel model)	5400	5404
points excl. by the Fischer test (c-vel model)	5357	5360

Table 14.2: Basic processing data about the Košťany area (both wrapped and unwrapped case).

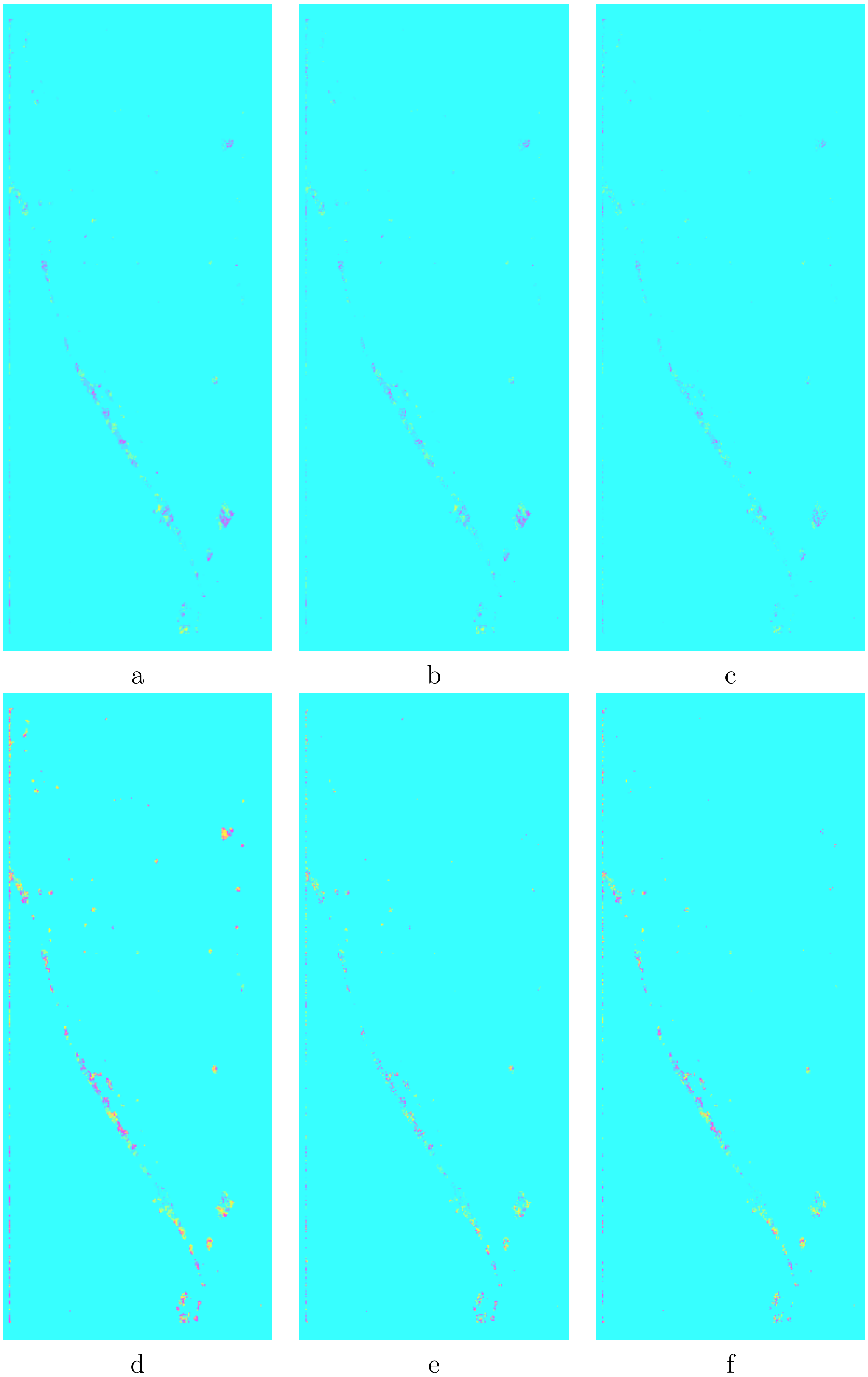

Figure 14.2: Results for the Ervěnice area – deformation model, deformation occured between 1997-03-03 and 1997-09-29. Results achieved from the wrapped phase are imaged in (a), (b), (c), results achieved from the unwrapped phase are imaged in (d), (e), (f). Images (a), (d) contain all processed points, images (b), (e) contain points validated using the Kolmogorov-Smirnov test, and images (c), (f) contain points validated using the Fischer test. The scale is imaged in figure 14.1, with -150 mm on the left and 150 mm on the right. Not all the values are in this range – this only applies for most of the corridor. The values of other pixels cannot be read out of this figure.

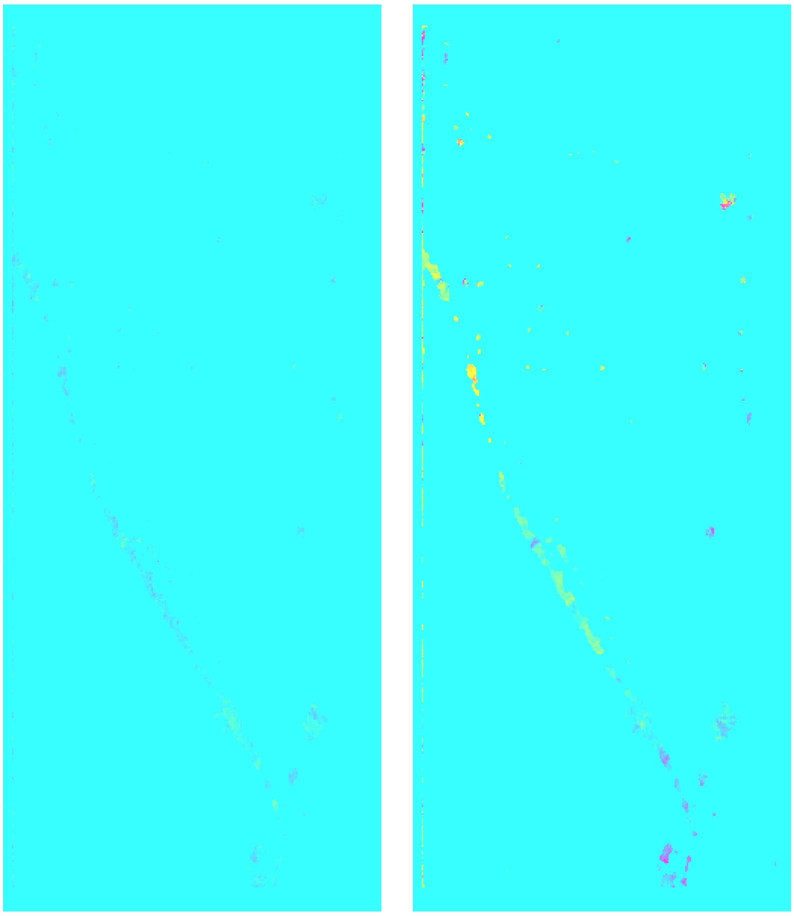

a b

Figure 14.3: Results for the Ervěnice area – velocity model, deformation occured between 1996-01-07 and 1996-03-17. Results achieved from the wrapped phase are imaged in (a), results achieved from the unwrapped phase are imaged in (b). Due to the very small number of points validated by the statistical tests (see table 14.1), we do not present the results validated by them. The scale is imaged in figure 14.1, with -50 mm on the left and 50 mm on the right. Not all the values are in this range – this only applies for most of the corridor. The values of other pixels cannot be read out of this figure.

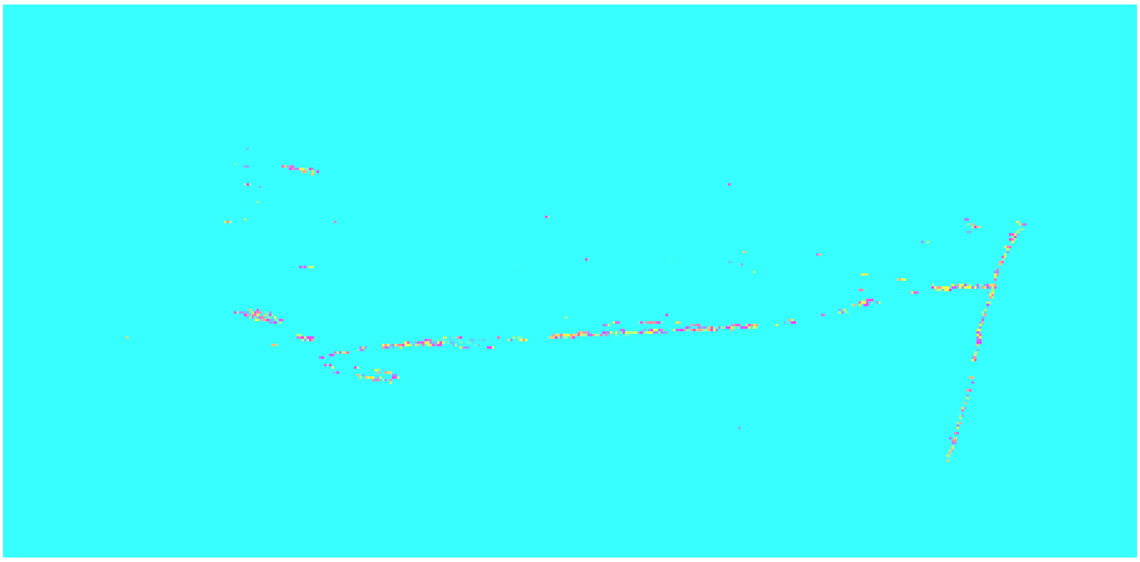

Figure 14.4: The Ervěnice corridor geocoded (unwrapped phase, deformation model). The deformation between scenes 9767 (1997-03-03) and 12773 (1997-09-29) is imaged. The resampling partially damaged the picture, and we therefore show this only for better orientation of the area. The coordinate system is latitude-longitude (WGS-84).

14.1 Interpretation

14.1.1 The Ervěnice area

It is not easy to interpret the Ervěnice corridor, the area which is more coherent than its surroundings, but the low coherence of its surroundings significantly influences phase unwrapping of the corridor itself. In addition, as seen in figures B.5 to B.7, the processed area contains gaps which may be in some interferograms large enough to interrupt the spatial continuity of the estimated phase unwrapping errors, which should be strengthened by the `init` step. The reference point is located in the bottom part of the corridor, in the magenta area in figure B.1 upper left.

Unfortunately, the reference point is not stable. The area of Ervěnice corridor is of such a nature, that we cannot rely that any of the points processed within the relatively spatially continuous (coherent) area might be stable. Therefore, we cannot say anything about the corridor as a whole, we can only look for the differences between individual parts of the corridor. However, partially due to the spatial incontinuity of the processed area, we can never be sure if the phase differences are caused by a real deformation or by inappropriate estimation of the unwrapping error.

One would expect the point near the reference point to have a similar deformation in time. The temporal progress of the deformation is imaged in figure 14.5 (a, b); please note that the deformation scale is significantly different, for the wrapped data the progress looks better (except for few scenes at the beginning), but it is probably comparable with regard to the range of possible values – probably, there was a large unwrapping error estimate in the wrapped case. On the other hand, the wrapped case loooks to be better spatially continuous.

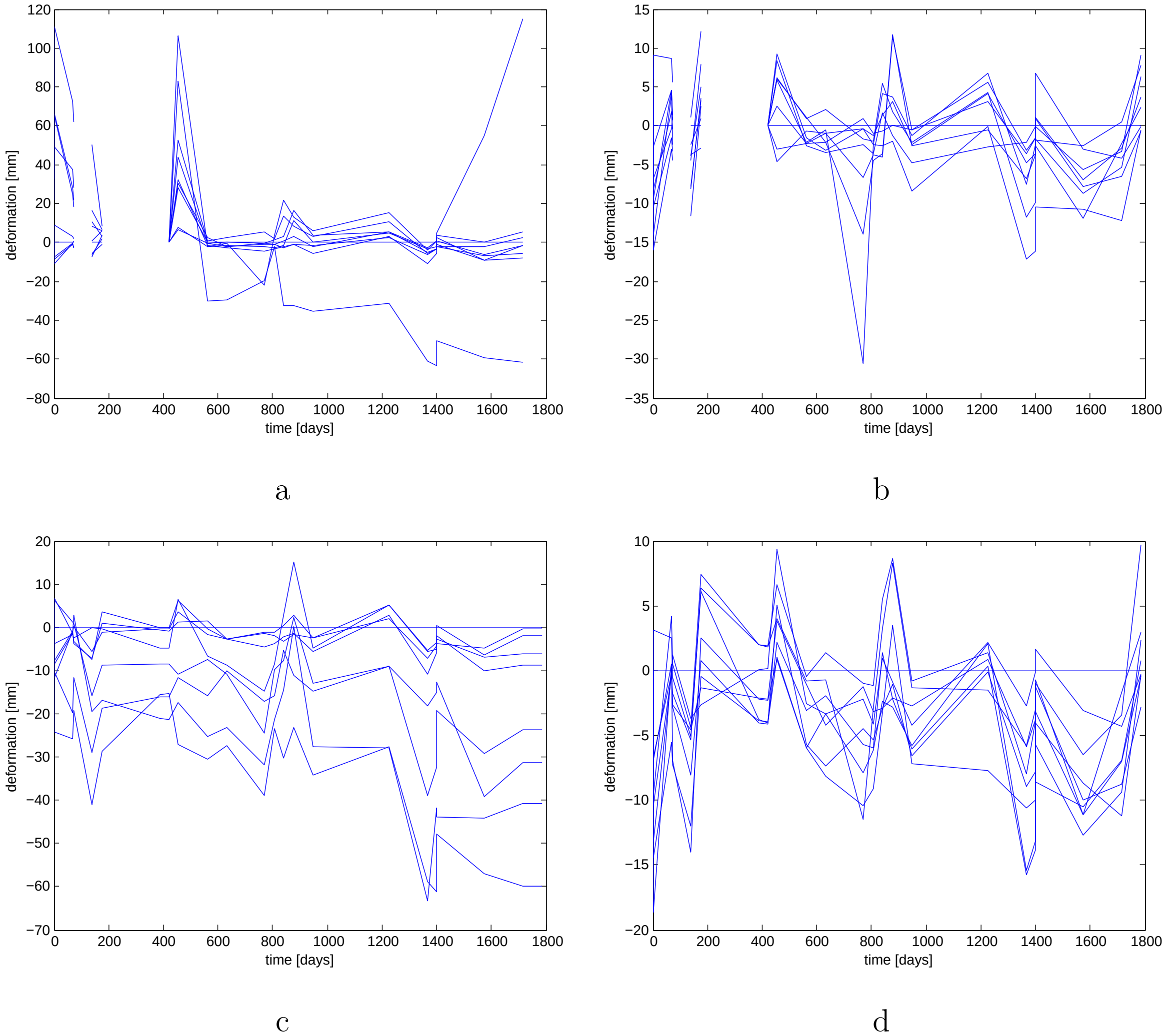

Figure 14.5: Progress of the deformation in time for the Ervěnice area. The figure images the reference point and its 8 neighbours. Atmosphere is not filtered. Image (a) contains the deformation for the wrapped phase and deformation model, image (b) contains the deformation for the unwrapped phase and deformation model, image (c) contains the deformation for the wrapped phase and velocity model, and image (d) contains the deformation for the unwrapped phase and velocity model.

In comparison to the Košťany area, where the same interferograms were excluded due to large referencing errors, here preanalysis showed different interferograms to be excluded (see table 14.1). This may cause the difference between the unwrapped and wrapped deformation (see figure 14.5 (a, b)) in comparison to the Košťany area (see figure 14.13) (a,b)), where both progressions were similar with regard to jumps (corresponding to the referencing errors).

However, referencing errors are attributed to interferograms, not to the scenes, and therefore may influence the temporal progression in a different way (due to the instability of the adjustment method).

For the Ervěnice area, we decided to interpret the wrapped data, we attribute the spatial

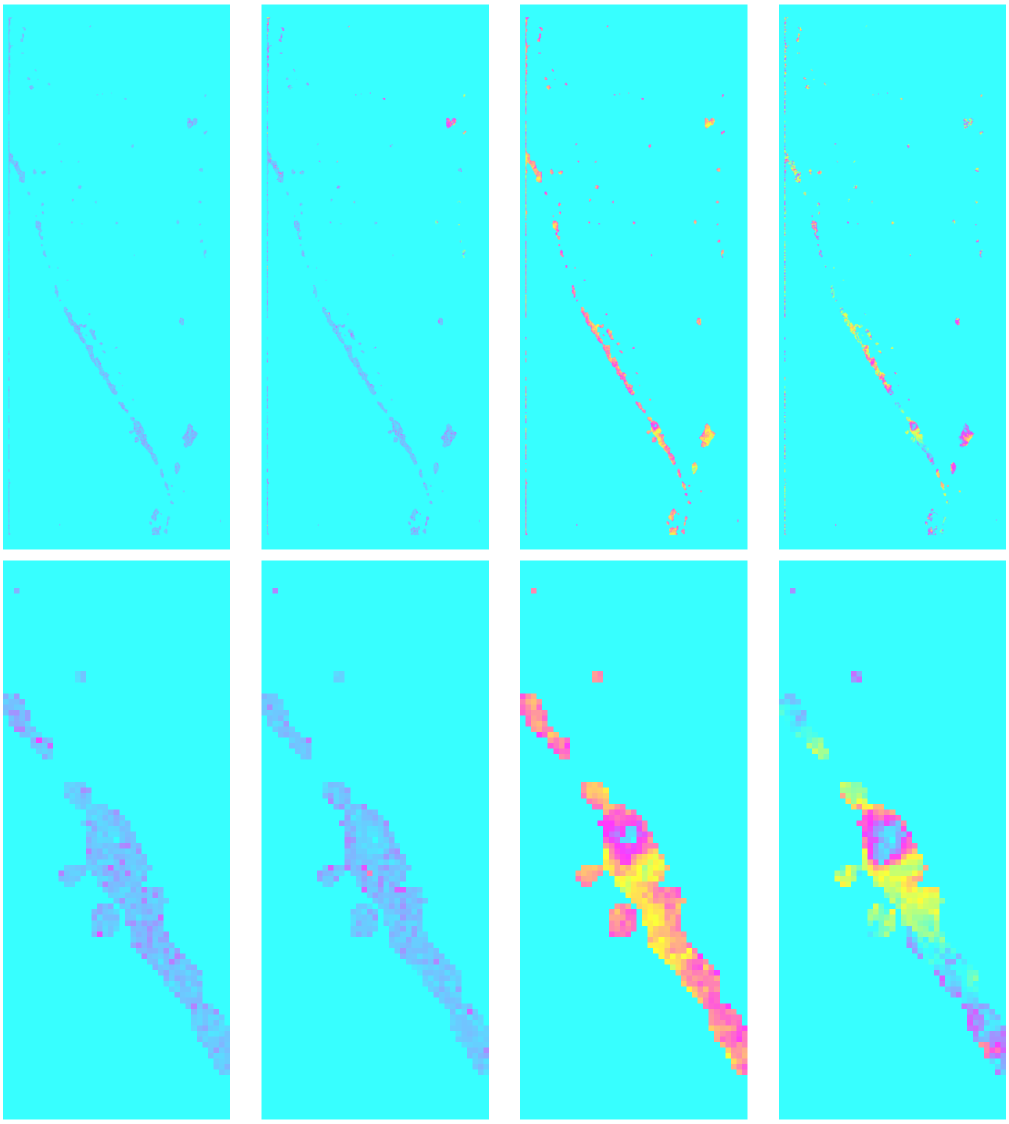

a b c d

Figure 14.6: Unique standard deviation m_0 for the Ervěnice crop. Image (a) contains the case where wrapped phase is used together with the deformation model, image (b) contains the case where unwrapped phase is used together with the deformation model, image (c) contains the velocity model with wrapped phase and image (d) contains the velocity model with unwrapped phase. The scale is imaged in figure 14.7 and is from 0 to 43 mm. The lower row represents the details of the upper figures – details around the reference point.

incontinuity to large unwrapping errors, influenced partially by the incoherent data out of the corridor. In the neighbourhood of the reference point, unwrapped and wrapped data give similar results.

Figure 14.8 shows the temporal progress of the deformation for points distant from the reference point. Please note that for the point close to the reference point (image (a)), all points within the small neighbourhood have a very similar temporal development.

Figure 14.7: Colorscale for the unique standard deviation.

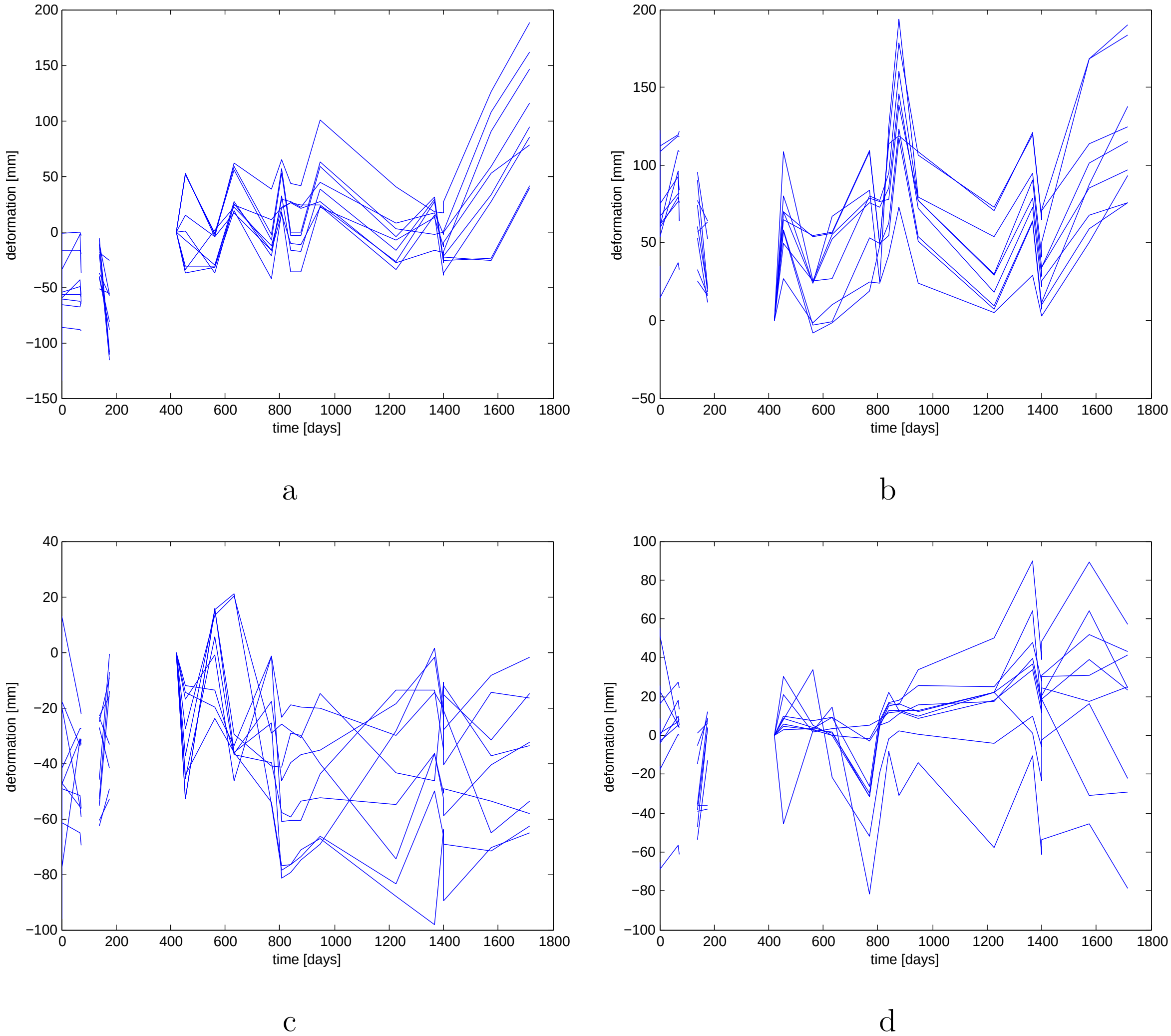

Figure 14.8: Temporal progress of the deformation in the Ervěnice crop for a point very close to the reference point (a), for a point in the right part of the area, separated from the corridor itself (b), for a point located near the centre of the corridor (c) and for the top part of the corridor (d). Deformation computed from the wrapped phase, using deformation model is imaged. The figures contain the progress of the deformation for nine points – centered at (470,154) for (a), (476,207) for (b), (389,98) for (c) and (180,16) for (d). The bottom part of the corridor is geographically located on the west, and the part separated from the corridor is on the south (see figure 14.4).

This is not the case of the other points, more distant from the reference point, and in all cases separated from the continuous area by a gap. Figure 14.8 therefore illustrates the

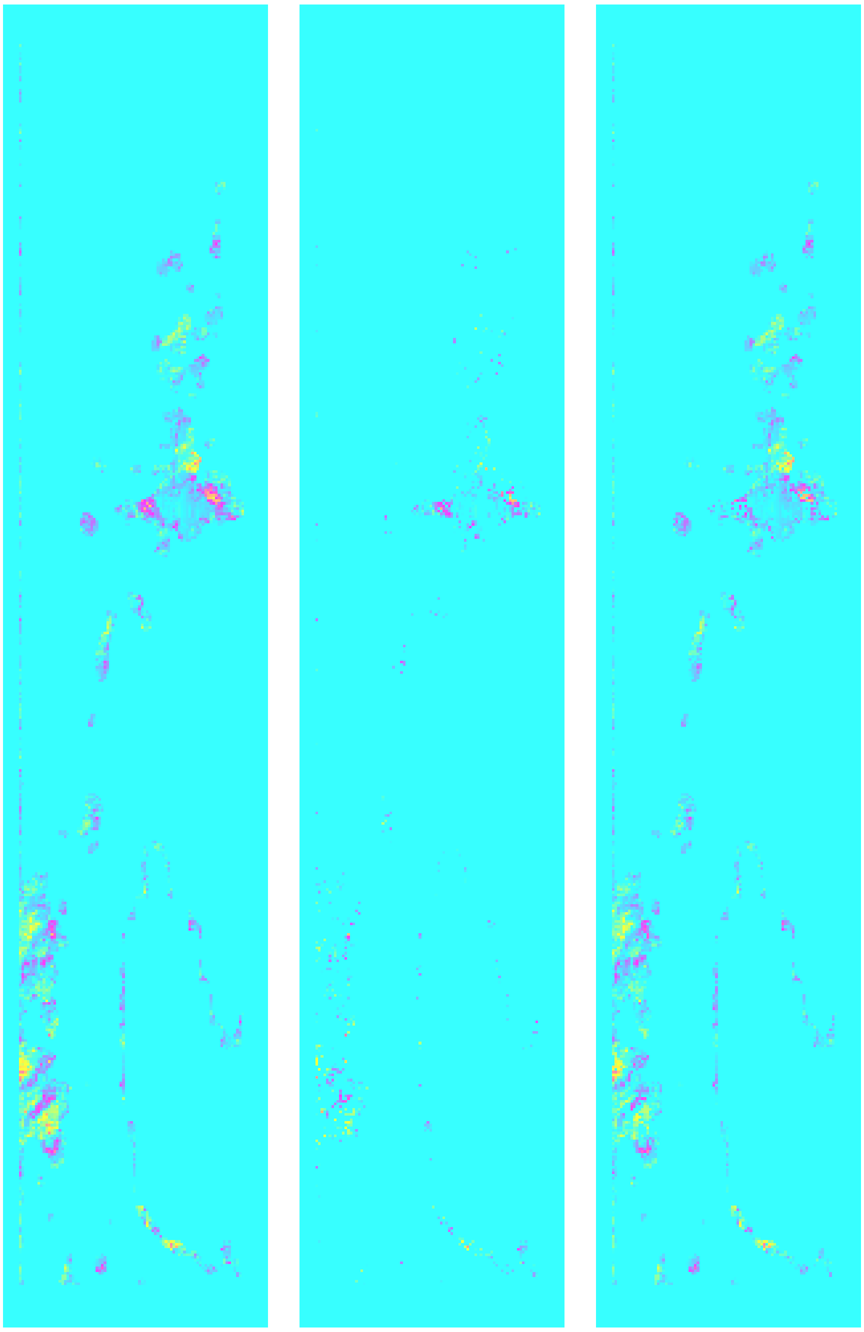

a b c

Figure 14.9: Results for the Košťany area – deformation model, wrapped case. Deformation occured between 1997-07-21 and 1998-04-27 are imaged. Image (a) represents all processed points, (b) represents points validated by the Kolmogorov-Smirnov test, and (c) represents points validated using the Fischer test. The scale is imaged in figure 14.1, with -150 mm on the left and 150 mm on the right. Not all the values are in this range – this only applies for the continuous region in the middle of the crop. The values of other pixels cannot be read out of this figure. Results for the unwrapped case are imaged in figure 14.10.

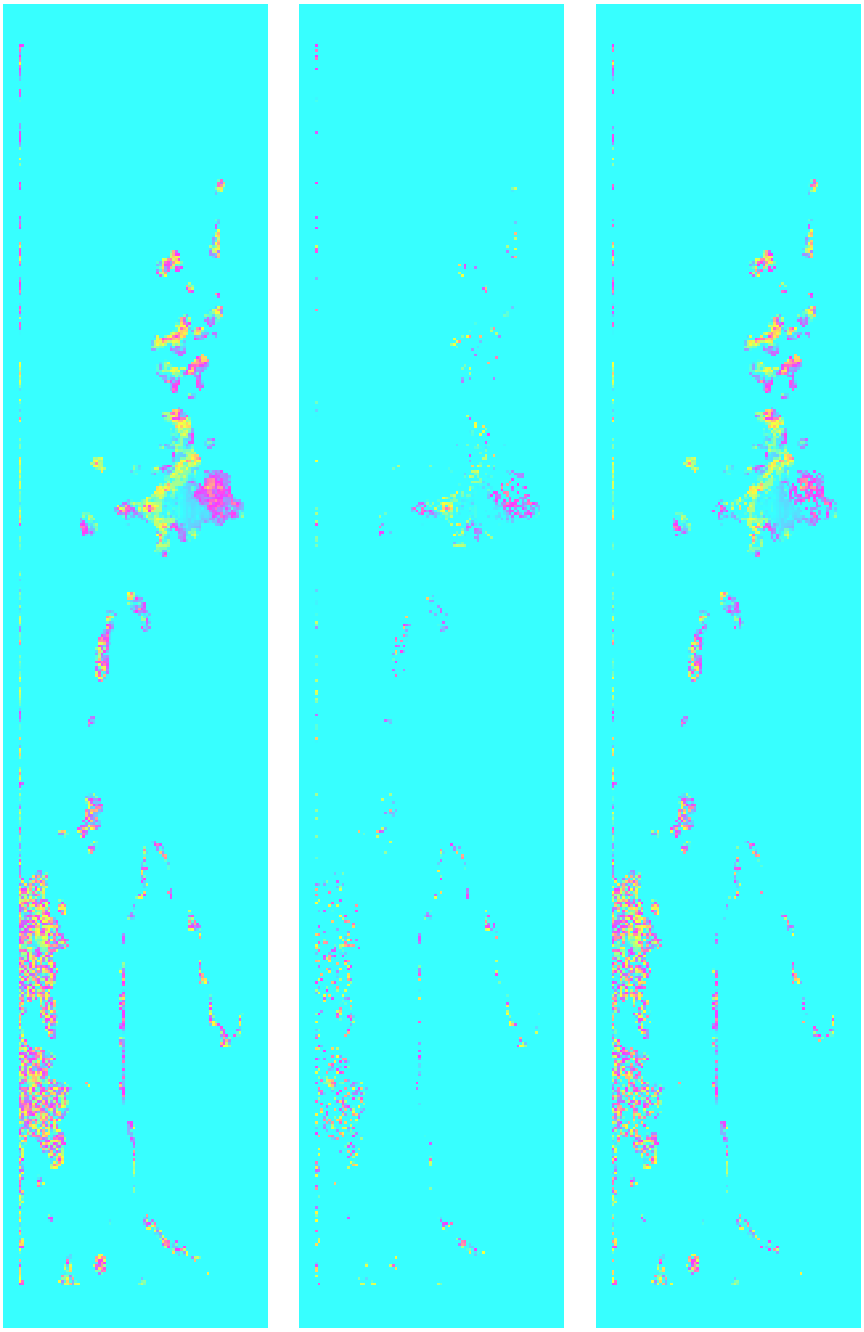

a b c

Figure 14.10: Results for the Košťany area – deformation model, unwrapped case. Deformation occured between 1997-07-21 and 1998-04-27 are imaged. Image (a) represents all processed points, (b) represents points validated by the Kolmogorov-Smirnov test, and (c) represents points validated using the Fischer test. The scale is imaged in figure 14.1, with -150 mm on the left and 150 mm on the right. Not all the values are in this range – this only applies for the continuous region in the middle of the crop. The values of other pixels cannot be read out of this figure. Results for the wrapped case are imaged in figure 14.9.

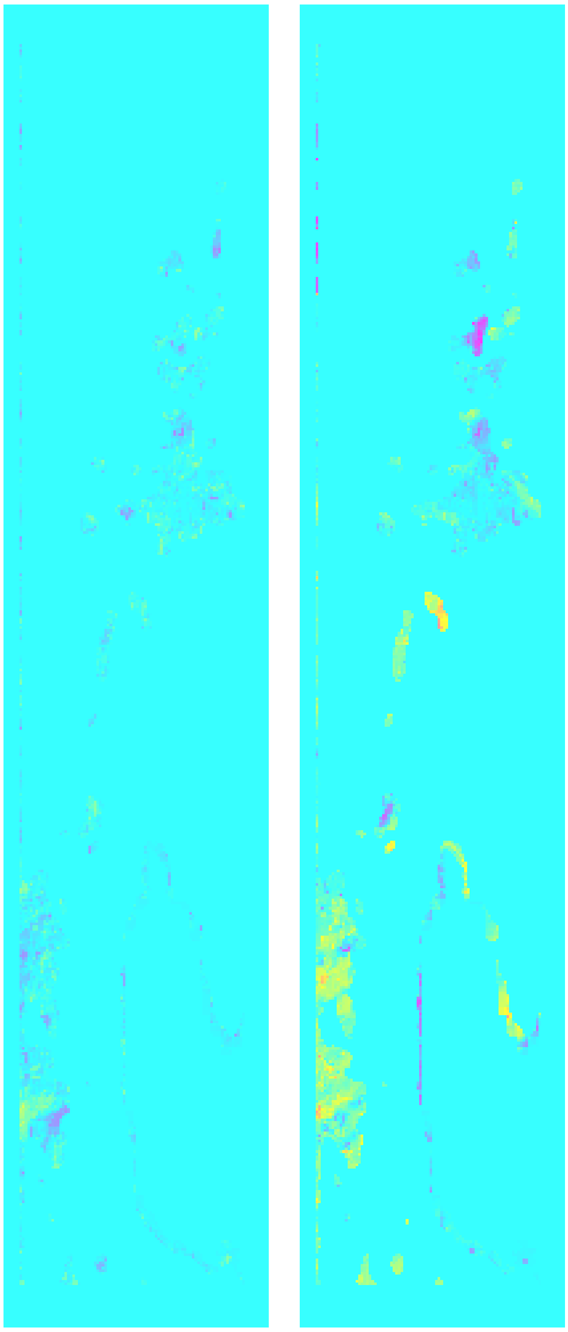

a b

Figure 14.11: Results for the Košťany area – velocity model, deformation occured between 1996-01-07 and 1996-06-30. Results achieved from the wrapped phase are imaged in (a), results achieved from the unwrapped phase are imaged in (b). Due to the very small number of points validated by the statistical tests (see table 14.2), we do not present the results validated by them. The scale is imaged in figure 14.1, with -150 mm on the left and 150 mm on the right. Not all the values are in this range – this only applies for the continuous region in the middle of the crop. The values of other pixels cannot be read out of this figure.

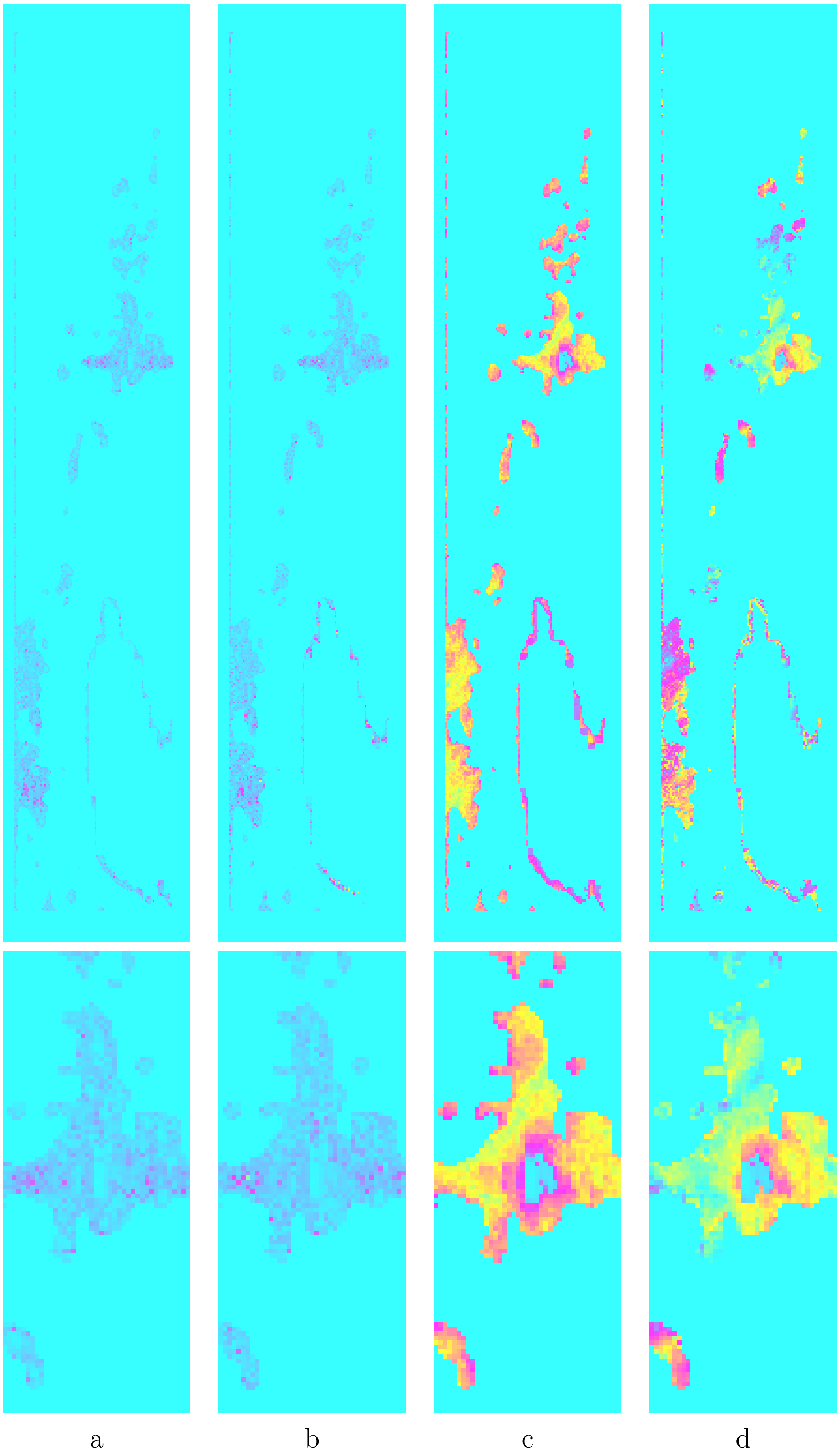

Figure 14.12: Unique standard deviation m_0 for the Košťany crop. Image (a) contains the case where wrapped phase is used together with the deformation model, image (b) contains the case where unwrapped phase is used together with the deformation model, image (c) contains the velocity model with wrapped phase and image (d) contains the velocity model with unwrapped phase. The scale is imaged in figure 14.7 and is from 0 to approx. 43 mm. The lower row represents the details of the upper figures – details around the reference point.

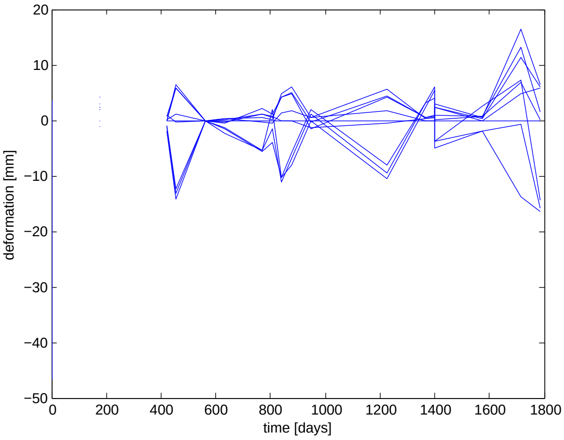

a

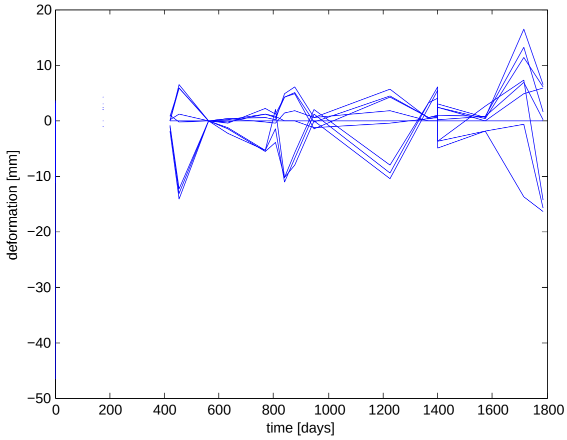

b

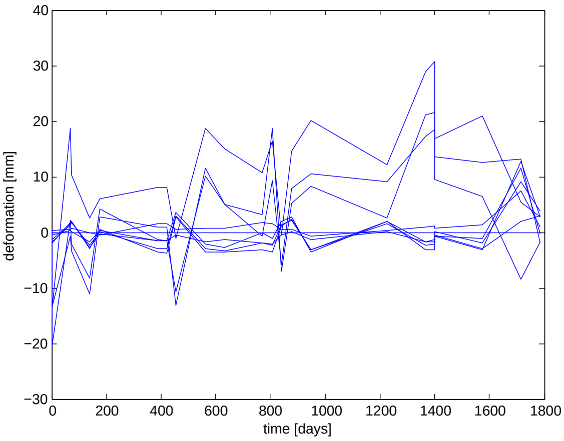

c

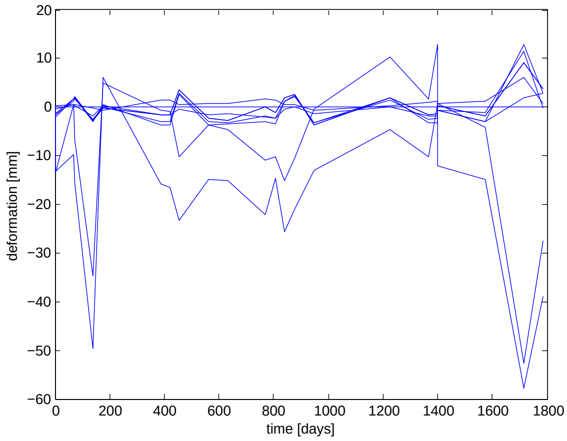

d

Figure 14.13: Progress of the deformation in time for the Košťany area. The figure images the reference point and its 8 neighbours. Atmosphere is not filtered. Image (a) contains the deformation for the wrapped phase and deformation model, image (b) contains the deformation for the unwrapped phase and deformation model, image (c) contains the deformation for the wrapped phase and velocity model, and image (d) contains the deformation for the unwrapped phase and velocity model.

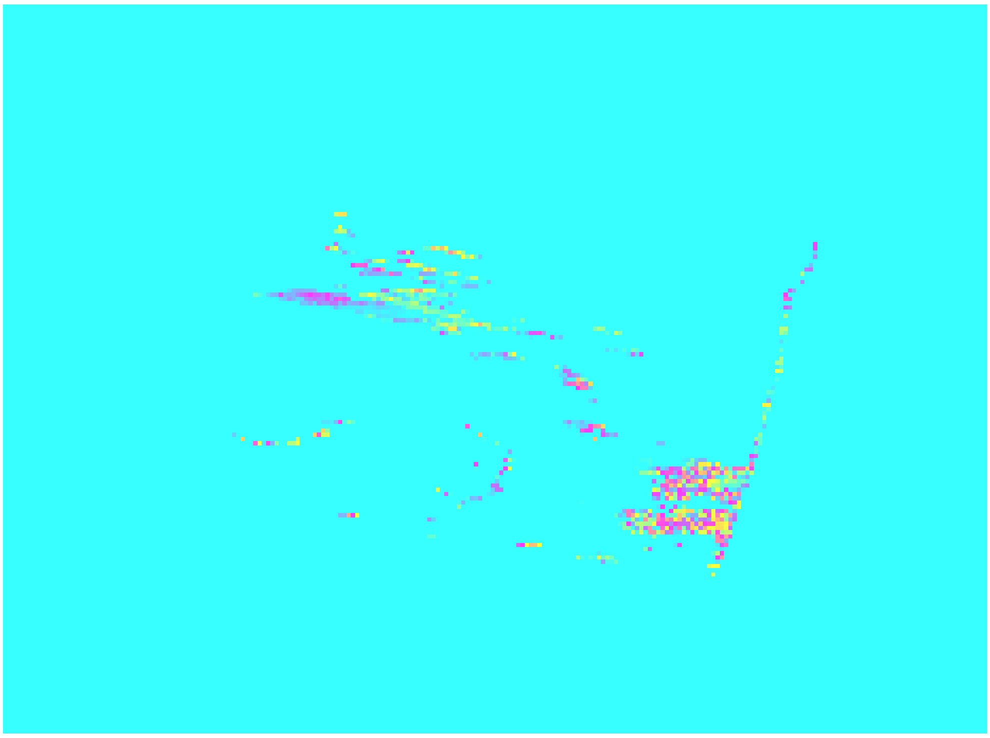

Figure 14.14: The Košťany area geocoded (unwrapped phase, deformation model). The deformation between scenes 11771 (1997-07-21) and 15779 (1998-04-27) is imaged. The resampling partially damaged the picture, and we therefore show this only for better orientation of the area. The coordinate system is latitude-longitude (WGS-84).

importance of the spatial continuity, i.e. the importance of the `init` step. The wrapped nature of the phase helped in the case of image (b) which corresponds to an area out of the corridor.

However, a subsidence trend or even the subsidence velocity cannot be estimated from these images, probably due to referencing errors.

14.1.2 The Košťany area

Regarding spatial continuity, which is a feature recognizable at the first glance, we can see that the results from the unwrapped phase are comparable to those computed from the wrapped phase (see figures B.8 to B.11 in Appendix B), considering the area containing the reference point (the centre of the village). Theoretically, the phase must be unwrapped – the wrapped case was involved into the study due to the suspiction that unwrapping errors to be corrected in the iterative adjustment may be smaller than in the unwrapped case. We will therefore only interpret the unwrapped results.

We can also see that the deformations computed for later dates are more continuous in space – however, figure 14.13 does not suggest a strange temporal development, except for the beginning of the time axis (the first tandem pair). On the other hand, this figure only concerns the area very close to the reference point (60 m in range and 10 m in azimuth).

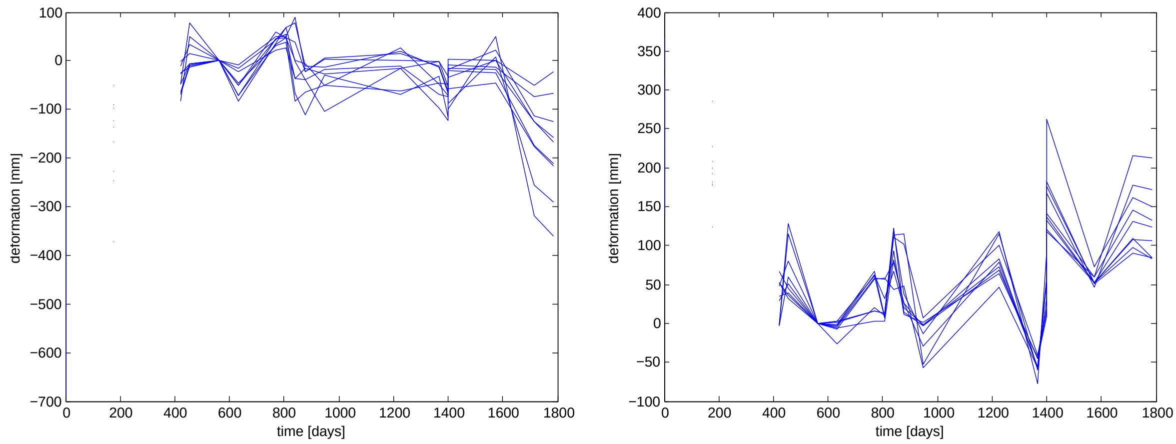

a b

Figure 14.15: Temporal progress of the deformation for the right (a) and left (b) side for the Košťany area – unwrapped phase, deformation model. The figures contain the progress of the deformation for nine points – centered at (191,51) for (a) and (191,83) for (b). The right side of the processed area corresponds to the south and the left side corresponds to the north of the area (see figure 14.14).

Regarding the temporal development of the deformation, imaged in figure 14.13 (b), it can be seen that the curves divide into two, which makes us think that the developments are computed rather well. On the other hand, the temporal discontinuity is probably caused by referencing errors (i.e. the phase of the reference point is imprecise due to partial decorrelation) or by atmosphere (which is improbable due to the small distance from the reference point). This opinion is enforced by the fact that all curves are discontinuous in a similar way. Unfortunately, a trend cannot be recognized here, and therefore we must conclude that the referencing errors are more significant that potential deformation trend.

Figures B.10 and B.11 suggest that the left and right sides of the coherent part of the Košťany area are deformed in a different way – a similar development may be seen in figure 14.13 (b) where the temporal development for 9 points follows two dominant curves. We therefore decided to plot the temporal development for two other points – one on the left side (north-eastern part of the village) of the coherent area and the other on the right side (south-western part of the village); see figure 14.15. Please note that both of these points are still in the centre of the village, due to the fact that the edges are not coherent. However, neither this figure confirms a deformation trend in any part of the area, the temporal incontinuities are probably caused by the referencing errors – we consider such temporal discontinuities very improbable to happen. Please note that the development in 14.15 (a) is more strange than in 14.15 (b), especially at the end of the time scale. This may be a sign for possible deformations in the north-eastern part of the village; however, the trend is too short (in time) and the difference between both parts of the village are less significant than the temporal irregularities found in figure 14.15. Let us here also remind that the spatial continuity is enforced by the `init` step, which may influence the similarity between both developments.

Unfortunately, this area is not in-situ monitored (according to our information), making it impossible to compare the results with other methods.

14.2 Discussion

An important problem in the interpretation is the unfamiliarity to the monitored area, or even a nonexistence of a coherent stable point. This is the case of the Ervěnice corridor – the area is a large waste dump where a road and a railway was built, with first estimations for subsidence about half a meter a year (in 1980s). If the reference point was stable, theoretically, it would be easy to say which part of the monitored area subsides and which one does not – without the knowledge, the only possibility is to find out the temporal progress of the deformation for the reference point and add it to the computed deformations of other pixels.

However, even if we supress the stability problem by looking only for deformation relative to the reference point, the results cannot be easily interpreted. There is always the possibility that the unwrapping errors estimation is wrong – the cycle condition fulfillment is not a guarantee that the errors are estimated right, and however small the unique standard deviation is, it is always a possibility that it might be even smaller for other solution. The problem of finding the "right" unwrapping error vector is impossible due to two facts:

- there is no guarantee that the unwrapping error vector with the smallest unique standard deviation is that one that corresponds to the physical reality;
- the vector with the smallest unique standard deviation can be found only if all vectors are exploited, which is not possible due to the limited computation time.

The results displayed spatially, see figures B.5 to B.11, look to be quite spatially continuous. However, if we use a more detailed colorscale (colorscale at 14.1 corresponding to the $\langle -3\pi, 3\pi \rangle$ interval), the images do not look spatially continuous any more. That means that the changes between neighbouring points are not very small, but they are smaller with regard to very points; however, they are not generally smaller with regard to relatively close (but not neighbouring) points.

In addition, the temporal progresses, imaged in figures 14.5, 14.8, 14.13, 14.15, are not continuous at all, and the trends cannot be estimated. This problem is attributed to the unsolved referencing, described in section 13.4, which therefore is an important problem to be solved in future.

As can be seen mainly in the Košťany area, out of the coherent village centre, the results here are spatially very incontinuous – one can say that it is neccessary to know the unwrapping errors exactly for one point, to estimate the unwrapping errors of the whole area – only gaps smaller than the range of the `init` step (described in section 13.6) can be overrun.

The difference between the results in both areas can be attributed to the following:

- the Košťany area is more coherent (see coherence thresholds in tables 14.1 and 14.2), and therefore the phase values are more reliable;

- the village centre of Košťany is spatially continuous, and we can afford to interpret only the results in the area containing the reference point;
- the Košťany area is probably more stable; the spatial variations at the Ervěnice corridor may be really caused by waste-dump subsidence.

Unfortunately, increasing the coherence threshold for the Ervěnice area would leave less points, creating even more (and larger) gaps, which would even worsen the spatial continuity of the results. Therefore, the problem seems unsolvable with the given coherence. On the other hand, it might help to increase the coherence threshold not by spatial selection, but by interferogram selection – to decrease the number of processed interferograms. Consequently, the number of redundant measurements would be smaller and it would probably even exclude several scenes (the results will be available for less dates).

The spatial continuity may be also improved by increasing the number of searched solutions in the `release` step (see section 13.7). However, due to the fact that the `release` step is mostly finished after this number of searched solutions (the only possibility to finish it earlier is to find the optimal solution at the beginning, when only few other solutions were found and the estimations cannot be developped any more (please remind that new solutions may be developped only if the cycle conditions are not fulfilled)), the time required for computations would increase together with the increasing number of searched solutions.

Another suggestion is also to adapt the `release` step so as to work also in case when the cycle conditions are fulfilled – if a suboptimal solution was found before the `release` step, with cycle conditions fulfilled, there is no way to continue searching for a better solution; however, we never know if the solution found is optimal or not.

The results computed for the velocity model are better spatially continuous; on the other hand, the unique standard deviation is much larger here than for the deformation model (see figures 14.6 and 14.12). In addition, the cycle conditions were not fulfilled for most of the points in the processed area. This is due to the fact that the `release` step, designed for the deformation model, does not work for the velocity model and requires an adaptation:

As described in section 13.7, the cycle residues vector r_{amb} (see formula (13.5)) is multiplied by the adjustment residue vector. However, due to the rank deficit in the velocity model, some adjustment residues are NaN (not-a-number), and also some cycle residues are zero, if some of the cycle conditions were fulfilled. In the velocity model, it often happens, that for all interferograms, the multiplication result is either NaN, or zero. The `release` step then cannot continue looking for other solutions.

The fact that the `release` step does not work here, also causes that the unwrapping errors do not change so much and the results look better spatially continuous.

One can see for both areas, that the deformations computed from wrapped phase are not so large as deformations computed from the unwrapped phase. This is given by the nature of phase unwrapping: the wrapped phase is within the $\langle -\pi, \pi \rangle$ interval, while the unwrapped phase is within the $(-\infty, \infty)$ interval, and taking that the estimated phase unwrapping errors are within a similar range, the wrapped data are expected to result in smaller deformations. However, it is not clear which of these deformations is closer to reality – if the unwrapping errors are really large and the differential interferograms should have not been unwrapped, or if the unwrapping errors are small and the phase of the differential interferogram varies in such a long range.

Coherence analysis

Appendix A contains graphs of mean coherence: each scene is paired with all of the others and the coherence of each pair is plotted with regard to both temporal and perpendicular baseline. We would like to to evaluate the influence of the temporal and perpendicular baselines to coherence.

One can say that the coherence is relatively high (except for the scene 25432) for the tandem pairs (temporal baseline is 1 day), but in other cases, it is practically independent from both temporal and perpendicular baselines. For some scenes, one can see that if paired with one or two other scenes, the coherence is significantly higher than if paired with others – we attribute this to seasonal effects: two scenes both acquired in winter are expected to be more coherent than two scenes, of which one (or both) was acquired in summer (due to vegetation).

Statistical tests

Statistical tests are described in section 13.9 in detail. Although the Fischer test only tests the value of the unique standard deviation with regard to the required accuracy, and the Kolmogorov-Smirnov test also tests the distribution of the residues, the number of points validated by these tests is similar (although there are many points validated by only one of these tests).

For the Košťany area, one can see in table 14.2 that the number of points excluded due to the Kolmogorov-Smirnov test is much larger than the number of points excluded due to the Fischer test (for the deformation model). This means that the unique standard deviation was small enough, but the residues did not have normal distribution.

Both tests were performed with the same confidence level of 5 %, and therefore it was not expected not happen that there are more points excluded due to the Fischer test than due to the Kolmogorov-Smirnov test, as was the case of Ervěnice, deformation model, wrapped phase (see table 14.1). Also in other cases it occured that there were some points excluded only due to the Kolmogorov-Smirnov test. The tests are performed independently, and the Kolmogorov-Smirnov test is implemented in MATLAB. However, we think that those points, which were excluded only by one of the tests, would be excluded by the other if slightly better accuracy was required. Therefore, we suggest to exclude all points which were not validated by both tests.

One would expect that the deformations, validated by the test, would look much more spatially continuous than the deformations without validation. However, figures 14.2, 14.9 and 14.10 do not confirm it, but the fact that the unfiltered figures look spatially more coherent may be caused by the fact that all points are imaged and spatial continuity is stressed by the `init` step of the iterative adjustment.

Regarding Košťany area, we would say that the Kolmogorov-Smirnov test filtered the results in a better way (see table 14.2 for the difference between the number of points excluded due to each test), but in the Ervěnice area, the filtered results look similar.

Chapter 15

Conclusions

InSAR is a potential technology to map ground deformations – landslides, subsidences, postseismic effects etc. Its advantage is that it allows to process the whole area at the same time, with no additional costs which would be the case of in-situ measurements. However, its temporal resolution is limited by the satellite overpass.

24 scenes from ERS-1/2, acquired in 1990s, were used for processing. A method was developped for processing, using iterative adjustment with the estimation of unwrapping errors. However bad the results look, they are much better than the first attempts, published in [44]. In the used scale, they are spatially continuous; however, no deformations can be estimated from the results.

The method might be useful to estimate an area which develops in a different way than any other area – e.g. in the Košťany crop, where the right and left sides of the coherent village centre develop differently. However, in our case, where referencing errors are higher than required, we cannot say if it is really caused by different deformation development, or by the instability of the method, particularly by the estimation of the unwrapping errors.

We think that the basic problem of our project is decorrelation. Although the Ervěnice corridor can be clearly distinguished from the surrounding area on the coherence map, its coherence is not high enough to provide a sufficient phase precision. Adjustment with unwrapping error correction is less stable (in the numerical way) than the conventional adjustment, and therefore requires better phase precision. The results from the Košťany area look better (the coherence threshold is higher here), but the coherence threshold of 0.5 (as recommended in [36]) cannot be used due to the fact that too few pixels would be selected for processing, and therefore the processed area would contain gaps.

In the designed algorithm, the gaps are a big problem: the algorithm relies on the spatial continuity of the area, estimating phase unwrapping errors on the basis of neighbouring points at the beginning. And it is now clear that without this estimation, the results are even less stable and therefore less spatially continous (and less reliable).

Unfortunately, InSAR always needs a pixel with known deformation. Usually, this is solved by putting the reference point into a stable area, but this procedure cannot be used in our case. In the Ervěnice corridor, no area can be a priori assumed to be stable. In addition, it is probable in this case that a stable point would be separated from the deformed area by an incoherent area, which would make the initial estimation of the unwrapping errors impossible.

However, in comparison to the preliminary results, these results look much better and we hope that future adaptation of the algorithm (most of all estimation of the referencing errors) will make the results reliable.

Chapter 16

Author's Contribution to the State of the Art

The following were performed by the author herself:

- Orbit error influence on the interferogram phase was derived for the flat-Earth phase, for DEM subtraction and also for the 3-pass case (instead of DEM, another interferogram is subtracted in order to eliminate topography influence) – see [41, 40].
- The method to coregister interferograms acquired on different tracks (see section 12.3.1) was developped – however, resampling introduces an error into the process.
- The approach to both point and interferogram selection was developed and used instead of manual selection of interferogram and processing all pixels in the interferograms (see section 13.2).
- The method to analyse phase sums and then exclude the worst interferograms was developed. However, this problem is not yet completed (see section 12.2).
- The system of iterative adjustment was designed (see figure 13.8):
  - `point_sel` (see figure 13.6),
  - `init`,
  - `corr_res`, see section 13.6,
  - `release`, see section 13.7.
- The whole postprocessing procedure was implemented in MATLAB, and optimized to be computed in a reasonable time (the pseudoinverse of the design matrix is computed only once for each point, however the adjustment is performed more times).
- The results were interpreted.

Chapter 17

Future Recommendations

In future, the following improvements in the method are suggested to be performed:

- The Permanent Scatterers method (as overviewed in Chapter 10) may be used, allowing deformation monitoring in areas which are not continuously coherent.
- GPS (or Galileo) measurements may be used to improve the accuracy of the InSAR measurements, especially allowing to estimate the unwrapping ambiguities/errors a priori (see e.g. [29, 30]).
- It may be possible to adapt the phase unwrapping, described in Chapter 7, using the map of pixels selected for unwrapping, and enforce that the pixels out of the selected area are not used for unwrapping. This time, we are not sure if GAMMA allows it, but it may be performed using a more complex approach.
- The reference phase of each interferogram may be adjusted with regard to the phase sums (the mean value or the histogram maximum) in interferogram doubles or triples. Thesis [36] uses the histogram approach; however, we are not sure if this is possible even for the case when most of the reference phases contain an error – the problems are described in section 13.4. The value of σ_{ref} (see section 13.4) should be ideally negligible with regard to the coherence standard deviation $\sigma_{\Delta\varphi,\gamma}$ (see section 6.3).
- The results are spatially incontinuous except for larger coherent areas. The condition of spatial continuity should be more stressed, e.g. taking more points in a different distance (using weights) into account is suggested. It is practically useless to perform adjustment for points where no a priori unwrapping errors are known.
- Another results may be achieved from a different track (where data are already delivered), or from an ascending track, allowing even to compute the deformations in the individual components, not just in the radar line of sight. This is theoretically possible even in the case of processing two neighbouring tracks – however, numerical instabilities are very probable here.

- In this thesis, the DEM error was estimated preliminarily and was not a part of the adjustment, as suggested in section 8.8. We suggest to perform the adjustment without the DEM error corrected, and also with its estimation during the adjustment, and to compare the results.

- The `release` method should be adapted in order to work also in the case when the cycle conditions are fulfilled for the initial solution – it allows to find other solution with the cycle conditions fulfilled with smaller m_0. In addition, the `release` method should be adapted in order to work also with the velocity model.

- Another suggestion for improvements in the deformation model is to estimate the atmospheric influence after adjustment, its elimination and to repeat the adjustment, together with unwrapping error correction. On the other hand, the atmospheric influence is expected to be small due to the fact that the interferograms were referenced to a single point and atmospheric influence is assumed to change only slowly in space (see section 9.4).

Bibliography

[1] R. Bamler and B. Schättler. SAR data acquisition and image formation. In G. Schreier, editor, *SAR Geocoding: data and systems*, pages 53–102. Wichmann Verlag, Karlsruhe, 1993.

[2] P. Berardino, G. Fornaro, R. Lanari, and E. Sansosti. A new algorithm for surface deformation monitoring based on small baseline differential SAR interferograms. *IEEE Transactions on Geoscience and Remote Sensing*, 40(11):2375–2383, 2002.

[3] K. Capaliniová. Filtrace interferometrických dat, 2006.

[4] C. W. Chen and H. A. Zebker. Network approaches to two-dimensional phase unwrapping: intractability and two new algorithms. *Journal of the Optical Society of America A.*, 17(3):401–414, mar 2000.

[5] M. Costantini. A novel phase unwrapping method based on network programming. *IEEE Transactions on Geoscience and Remote Sensing*, 36(3):813–821, may 1998.

[6] M. Costantini, F. Malvarosa, F. Minati, L. Pietranera, and G. Milillo. A three-dimensional phase unwrapping algorithm for processing of multitemporal sar interferometric measurements. In *Proceedings of IEEE International Geoscience and Remote Sensing Symposium. IGARSS 2002*, volume 3, pages 1741–3, 2001.

[7] M. Costantini, F. Malvarosa, F. Minati, L. Pietranera, and G. Milillo. A three-dimensional phase unwrapping algorithm for processing of multitemporal SAR interferometric measurements. In *igarss02*, 2002.

[8] M. Crosetto. Calibration and validation of SAR interferometry for DEM generation. *ISPRS Journal of Photogrammetry and Remote Sensing*, 57:213–227, 2002.

[9] A. Ferretti, C. Prati, and F. Rocca. Permanent scatterers in SAR interferometry. *IEEE Transactions on Geoscience and Remote Sensing*, 39(1):8–20, jan 2001.

[10] F. Gatelli, A. Monti Guarnieri, F. Parizzi, P. Pasquali, C. Prati, and F. Rocca. The wavenumber shift in SAR interferometry. *IEEE Transactions on Geoscience and Remote Sensing*, 32(4):855–865, jul 1994.

[11] D. C. Ghiglia and M. D. Pritt. *Two-dimensional phase unwrapping: theory, algorithms, and software.* John Wiley & Sons, Inc, New York, 1998.

[12] R. M. Goldstein and C. L. Werner. Radar interferogram filtering for geophysical applications. *Geophysical Research Letters*, 25(21):4035–4038, nov 1998.

[13] M. Hampacher and V. Radouch. *Teorie chyb a vyrovnávací počet*. Vydavatelství ČVUT, 2000.

[14] R. Hanssen. Stochastic modeling of time series radar interferometry. In *igarss04*, pages cdrom, 4 pages, 2004.

[15] R. Hanssen and A. Feijt. A first quantitative evaluation of atmospheric effects on SAR interferometry. In *fringe96*, pages 277–282. ESA SP-406, 1996.

[16] R. F. Hanssen. An improved stochastic model for multi-pass radar interferometry. In *2nd International Symposium on Operationalization of Remote Sensing, Enschede, The Netherlands,*, 1999.

[17] R. F. Hanssen. *Radar Interferometry: Data Interpretation and Error Analysis*. Kluwer Academic Publishers, Dordrecht, 2001.

[18] R. F. Hanssen. *Radar Interferometry: Data Interpretation and Error Analysis*. PhD thesis, Delft University of Technology, 2001.

[19] M. Jehle, O. Frey, D. Small, E. Meier, and D. Nűesch. Improved knowledge of SAR geometry through atmospheric modelling. In *eusar2004*, pages 909–911, 2004.

[20] J. Kalát. Description of the košťany crop (private correspondence).

[21] B. Kampes. DORIS manual. http://enterprise.lr.tudelft.nl/doris/usermanual/.

[22] B. M. Kampes and R. F. Hanssen. Ambiguity resolution for permanent scatterer interferometry. *IEEE Transactions on Geoscience and Remote Sensing*, in print, 2004.

[23] H. Laur, P. Bally, P. Meadows, J. Sanchez, B. Schättler, E. Lopinto, and D. Esteban. Derivation of the backscattering coefficient sigmanought in ESA ERS SAR PRI. ESA Document No: ES-TN-RS-PM-HL09, http://earth.esa.int/pub/ESA_DOC/ers_sar_calibration_issue2_5f.pdf, 1998.

[24] P. Marinkovic, G. Ketelaar, and R. Hanssen. A controled Envisat/ERS permanent scatterer experiment, implications of corner reflector monitoring. In *CEOS SAR Workshop, Ulm Germany, 27–28 May 2004*, page submitted, 2004.

[25] D. Massonnet and K. L. Feigl. Radar interferometry and its application to changes in the earth's surface. *Reviews of Geophysics*, 36(4):441–500, nov 1998.

[26] C. Oliver and S. Quegan. *Understanding Synthetic Aperture Radar Images*. Artech House, 1998.

[27] ERS and ENVISAT precise orbit determination. http://www.deos.tudelft.nl/ers/precorbs/.

[28] B. Rabus, M. Eineder, A. Roth, and R. Bamler. The shuttle radar topography mission—a new class of digital elevation models acquired by spaceborne radar. *ISPRS Journal of Photogrammetry and Remote Sensing*, 57:241–261, 2003.

[29] S. Samsonov and K. Tiampo. Analytical optimization of DInSAR and GPS dataset for derivation of three-dimensional surface motion. *IEEE Transactions on geoscience and remote sensing*, 3:107–111, 2006.

[30] S. Samsonov, K. Tiampo, J. Rundle, and Z. Li. Application of dinsar-gps optimization for derivation of fine-scale surface motion maps of southern california. *IEEE Transactions on geoscience and remote sensing*, 45:512–521, 2007.

[31] Esa instrument description. http://envisat.esa.int/cgi-bin/printer_friendly.cgi?/dataproducts/asar/CNTR3-1.htm?06.12.2002.

[32] Pharus: More on the sar principle. http://www.tno.nl/instit/fel/os/fac/ra_fac_pha_more_sar.html

[33] D. Small, C. Werner, and D. Nüesch. Baseline modelling for ERS-1 SAR interferometry. In *igarss93*, pages 1204–1206, 1993.

[34] H. Tarayre and D. Massonnet. Effects of refractive atmosphere on interferometric processing. In *igarss94*, pages 717–719, 1994.

[35] H. Tarayre and D. Massonnet. Atmospheric propagation heterogeneities revealed by ERS-1 interferometry. *Geophysical Research Letters*, 23(9):989–992, may 1996.

[36] S. Usai. *A New Approach for Long Term Monitoring of Deformations by Differential SAR Interferometry*. PhD thesis, Delft University of Technology, 2001.

[37] S. Usai. A least squares database approach for SAR interferometric data. *IEEE Transactions on Geoscience and Remote Sensing*, 41(4):753–760, apr 2003.

[38] V. ústav pro hnědé uhlí a.s. Koncepce řešení ekologických škod vzniklých před privatizací hnědouhelných těžebních společností v Ústeckém a karlovarském kraji. http://www.kzv-most.cz/koncepce/, 2002.

[39] I. Čapková. Potenciálně nestabilní území severočeské hnědouhelné pánve a krušných hor, 2005.

[40] I. Čapková. Radarová interferometrie: chyby v georeferencování. In *Aktuální problémy fotogrammetrie a dálkového průzkumu Země*, 2005.

[41] I. Čapková. Satellite orbit errors and their influence on interferograms (diploma thesis), 2005.

[42] C. L. Werner, U. Wegmüller, and T. Strozzi. Processing strategies for phase unwrapping for insar applications. In *Proceedings 4th European Conference on Synthetic Aperture Radar. EUSAR 2002*, pages 353–6, 2002.

[43] Wikipedia, the free encyclopedia. http://en.wikipedia.org/wiki/Delaunay_triangulation, 2007.

[44] I. Čapková, D. David, and L. Halounová. Detecting land deformation in the area of northern bohemia using insar stacks (preliminary results). In *Proceedings of 25 EARSeL Symposium*, 2006.

Appendix A

Coherence Analysis

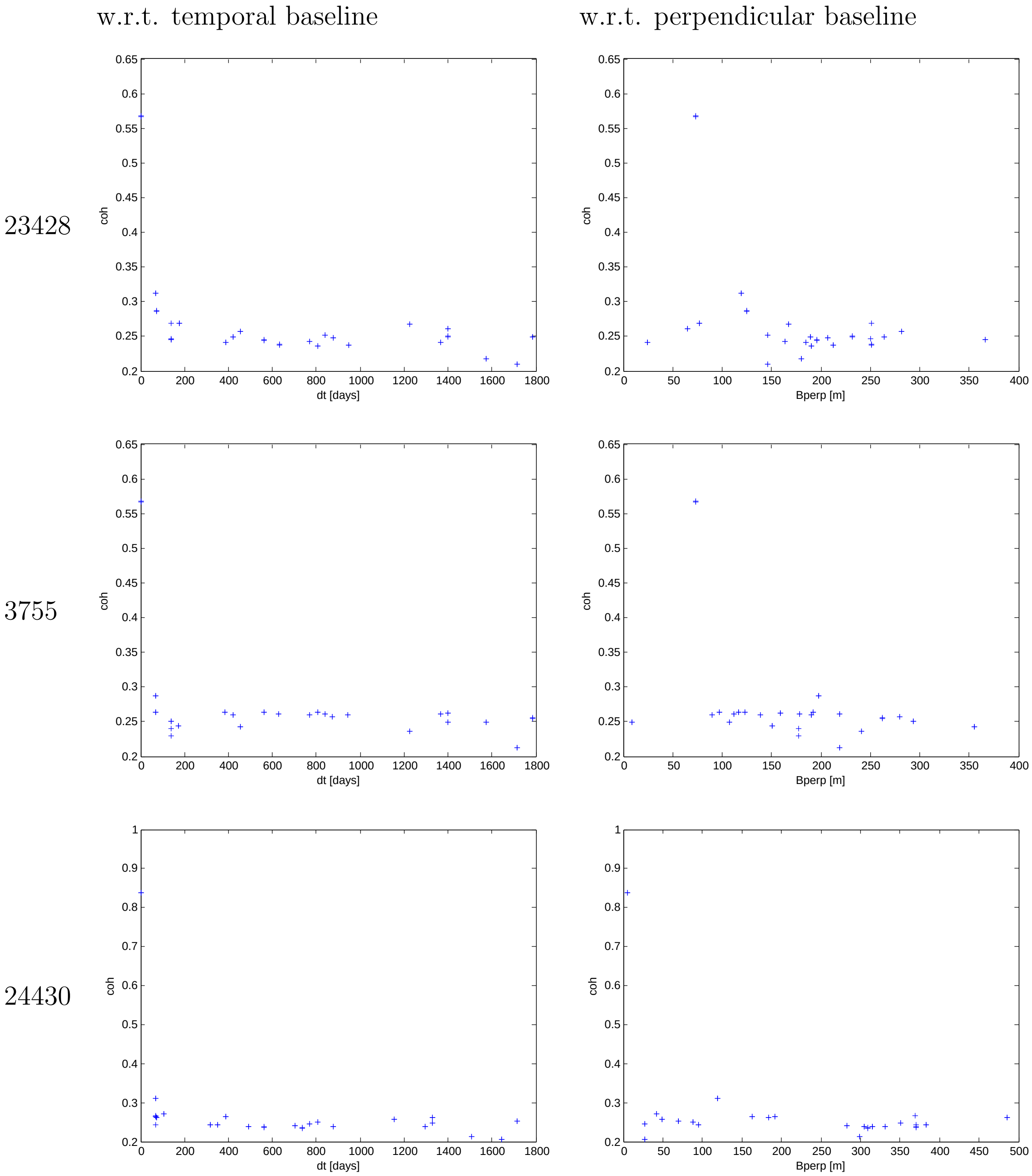

Figure A.1: Coherence with regard to the temporal and perpendicular baselines for the Ervěnice area for interferograms created from the scenes 23428, 3755 and 24430.

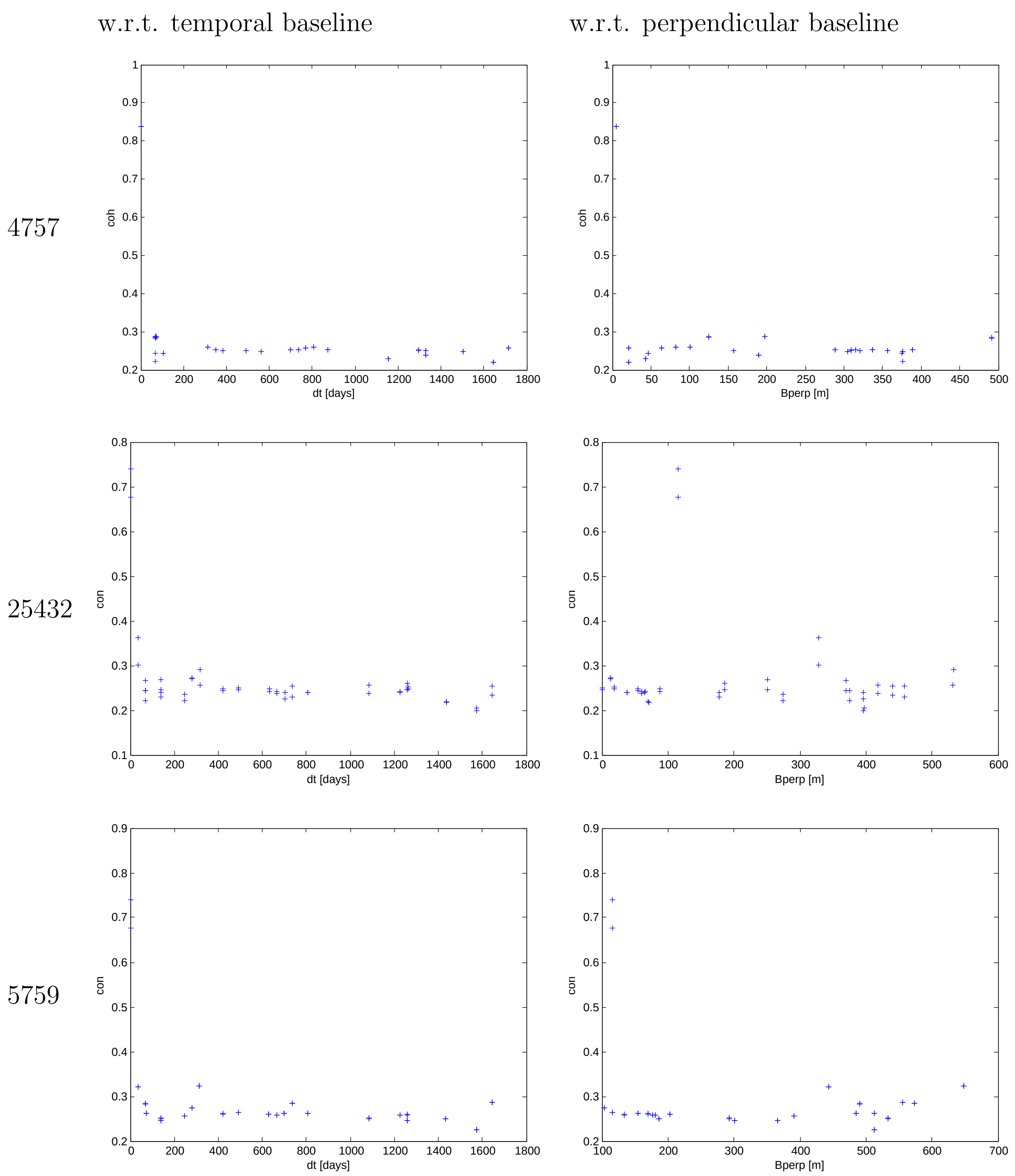

Figure A.2: Coherence with regard to the temporal and perpendicular baselines for the Ervěnice area for interferograms created from the scenes 4757, 25432 amd 5759.

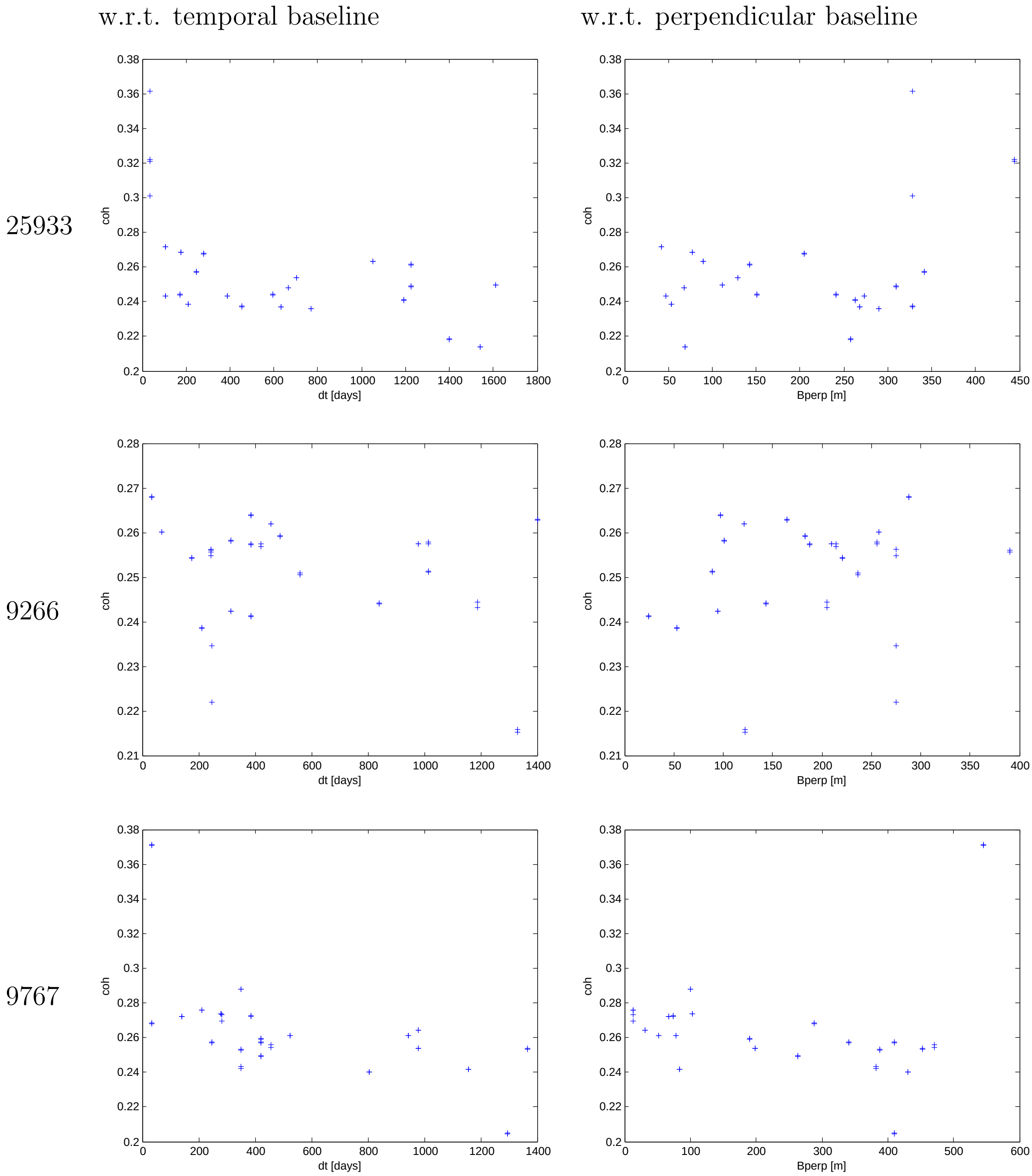

Figure A.3: Coherence with regard to the temporal and perpendicular baselines for the Ervěnice area for interferograms created from the scenes 25933, 9266 and 9767.

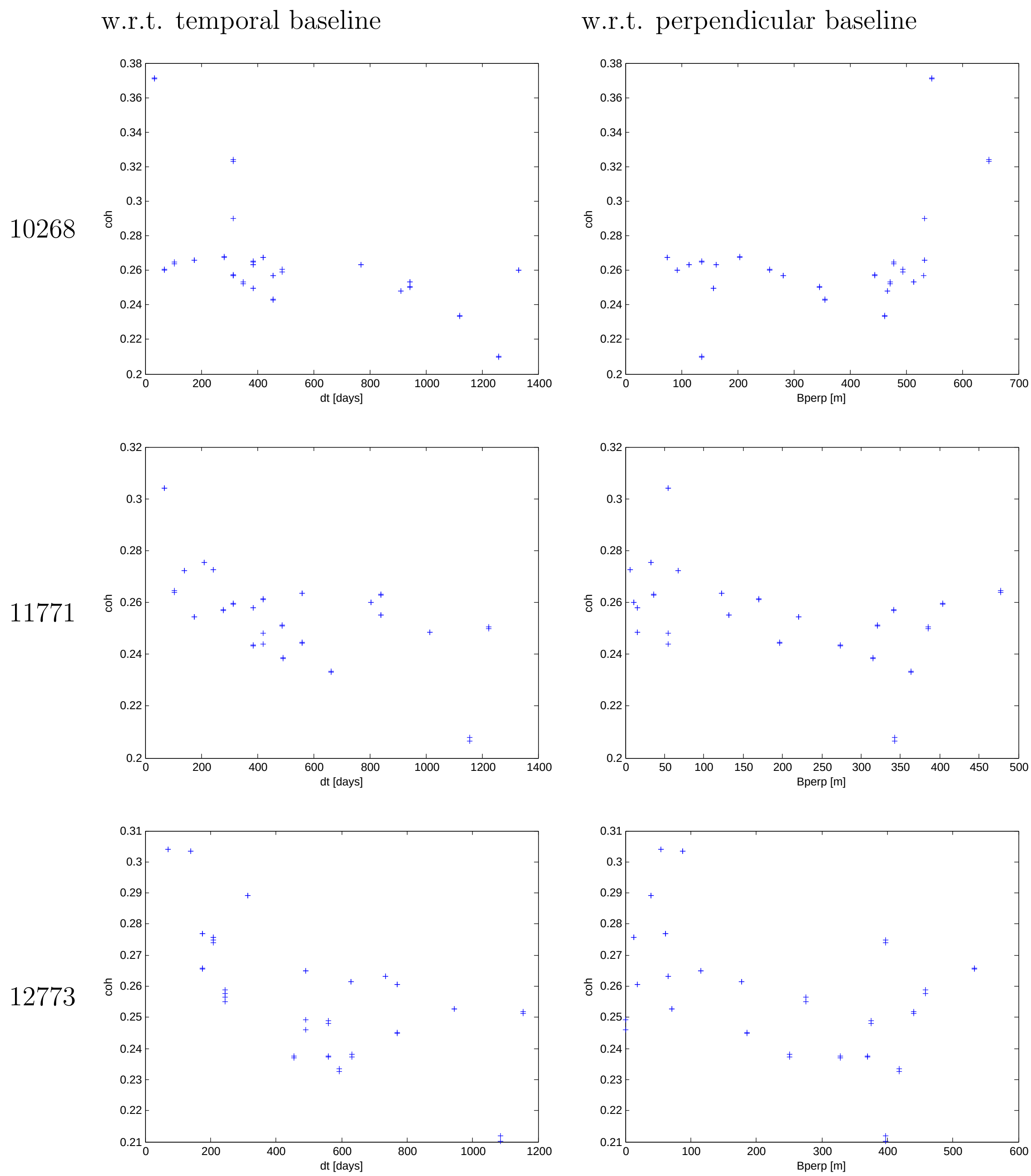

Figure A.4: Coherence with regard to the temporal and perpendicular baselines for the Ervěnice area for interferograms created from the scenes 10268, 11771 and 12773.

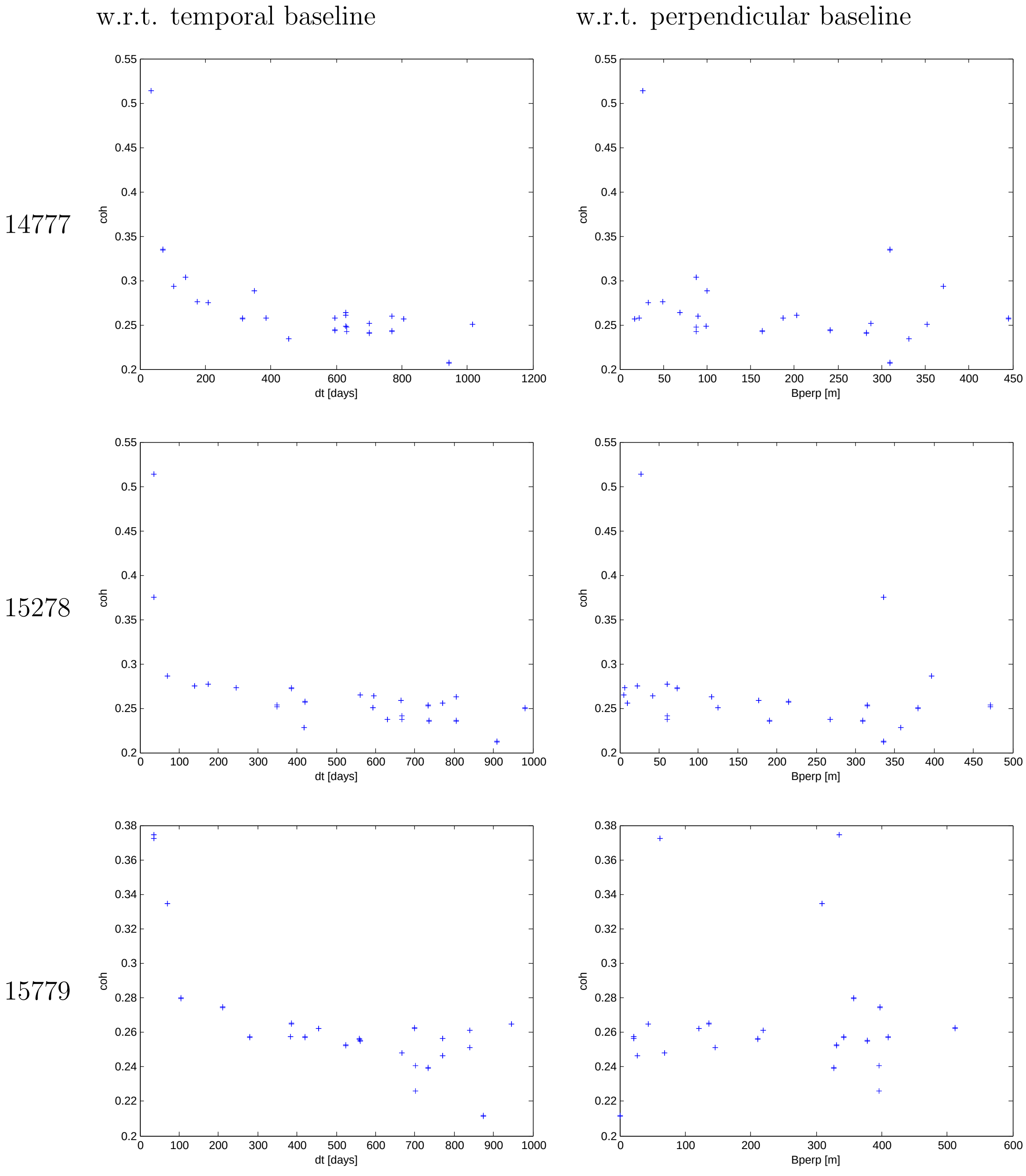

Figure A.5: Coherence with regard to the temporal and perpendicular baselines for the Ervěnice area for interferograms created from the scenes 14777, 15278 and 15779.

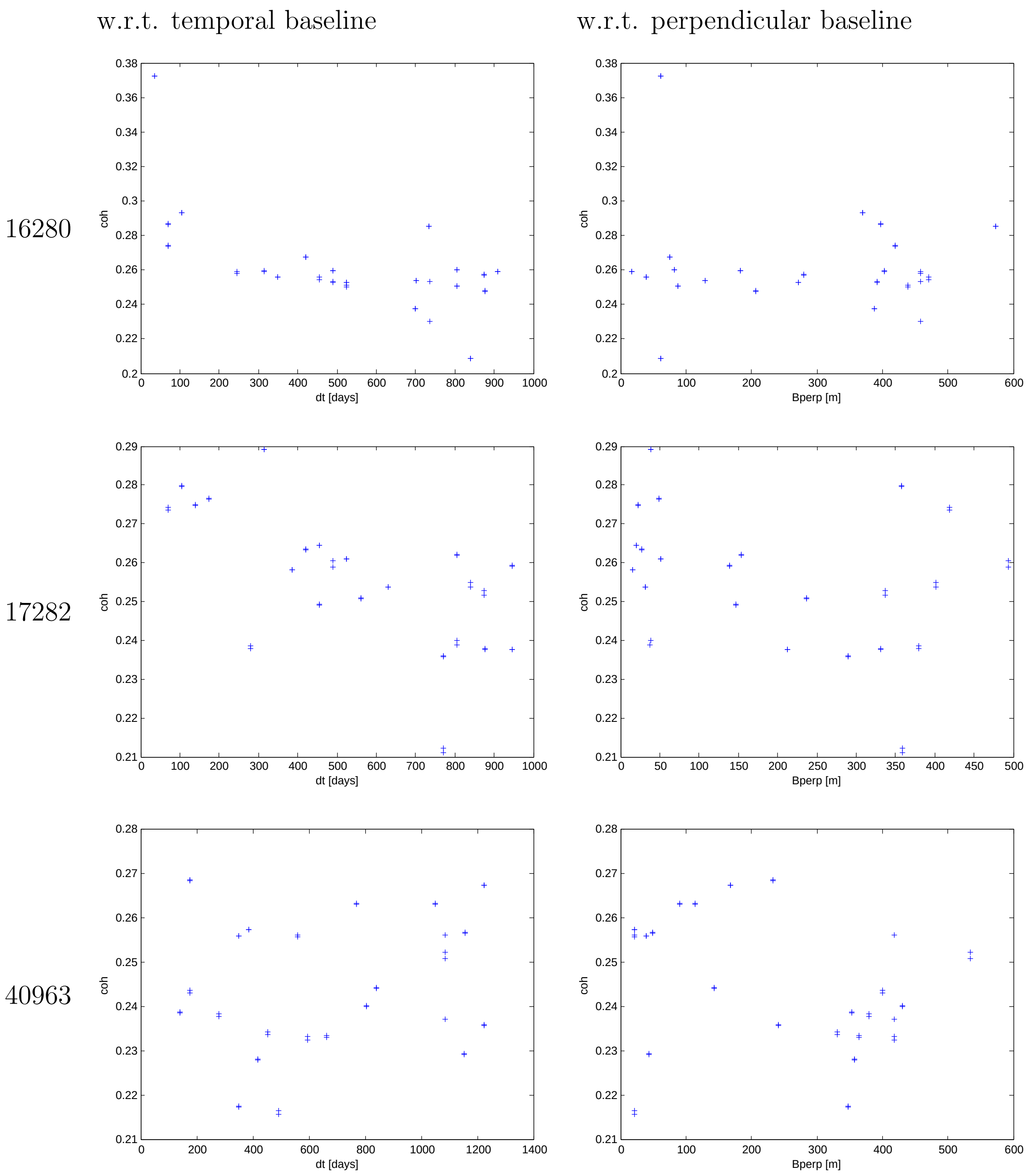

Figure A.6: Coherence with regard to the temporal and perpendicular baselines for the Ervěnice area for interferograms created from the scenes 16280, 17282 and 40963.

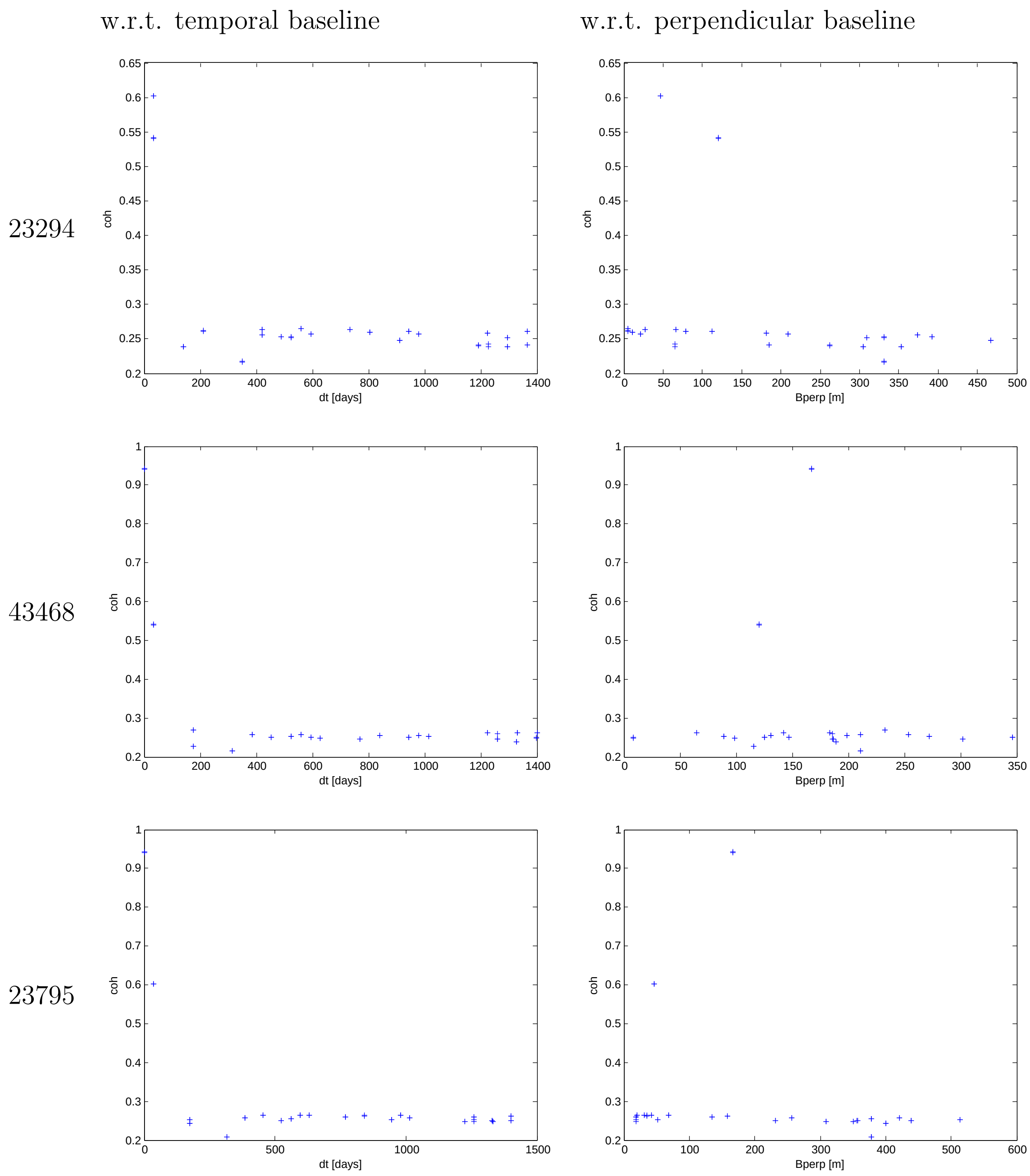

Figure A.7: Coherence with regard to the temporal and perpendicular baselines for the Ervěnice area for interferograms created from the scenes 23294, 43468, 23795.

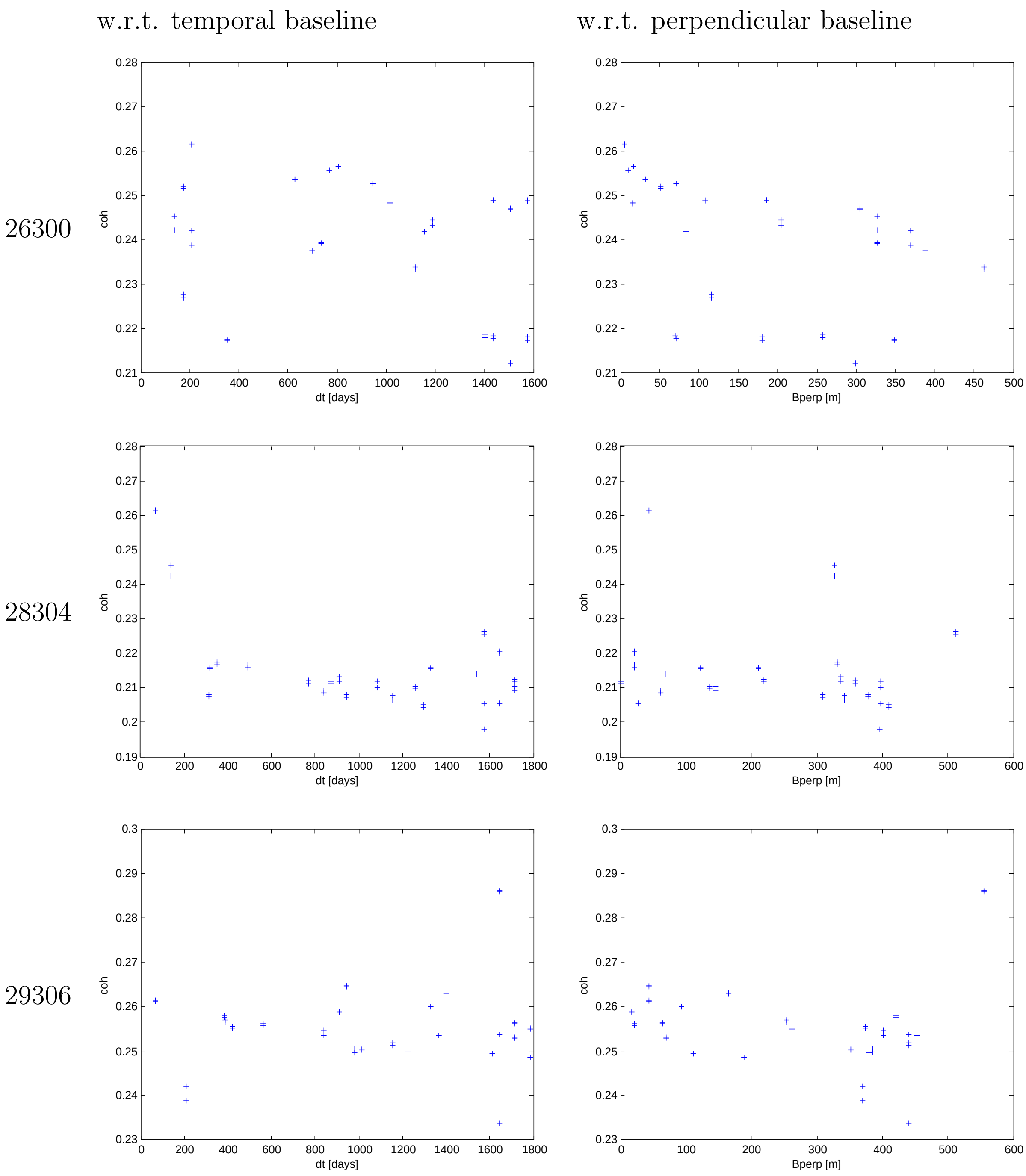

Figure A.8: Coherence with regard to the temporal and perpendicular baselines for the Ervěnice area for interferograms created from the scenes 26300, 28304 and 29306.

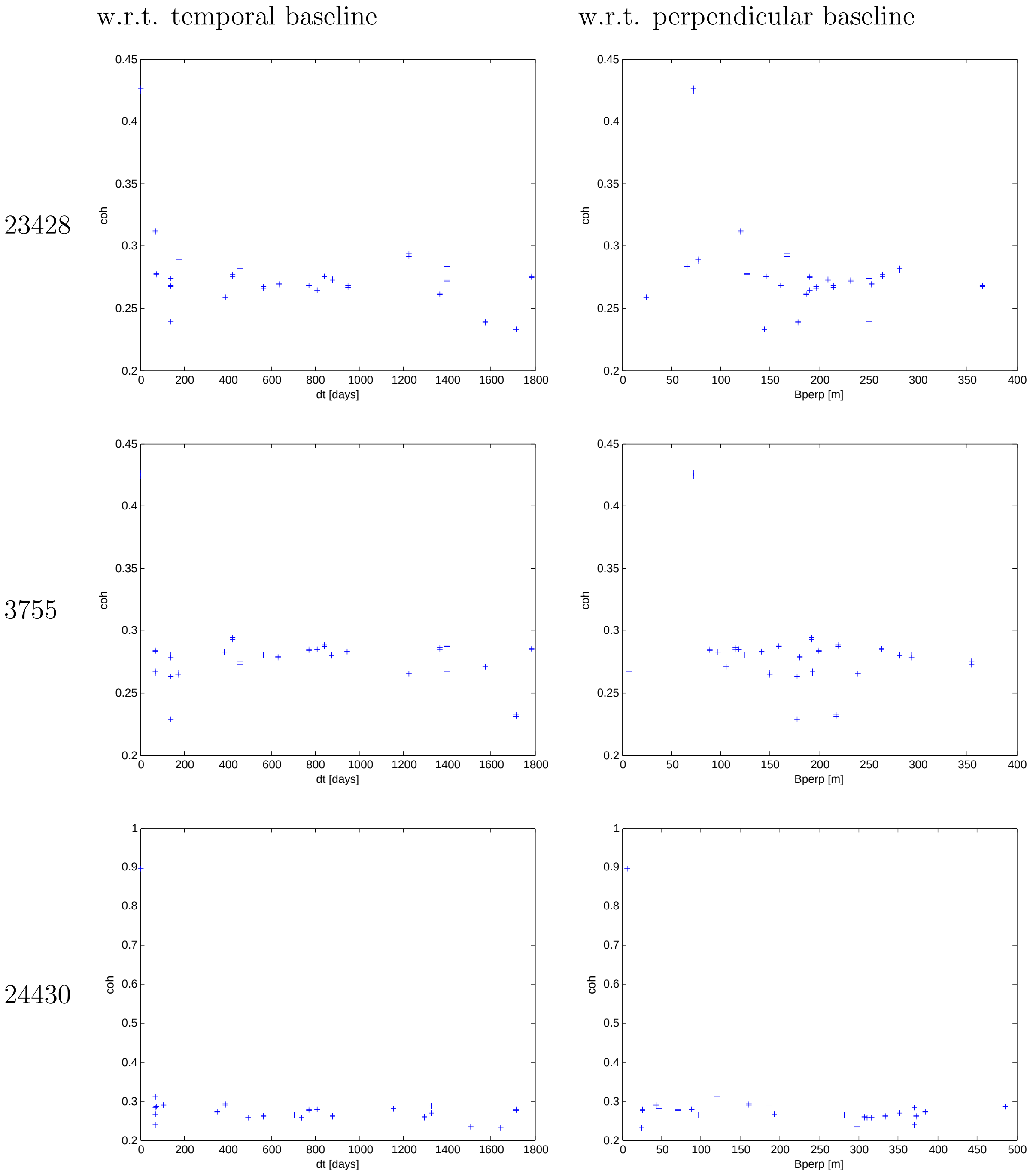

Figure A.9: Coherence with regard to the temporal and perpendicular baselines for the Košťany area for interferograms created from the scenes 23428, 3755 and 24430.

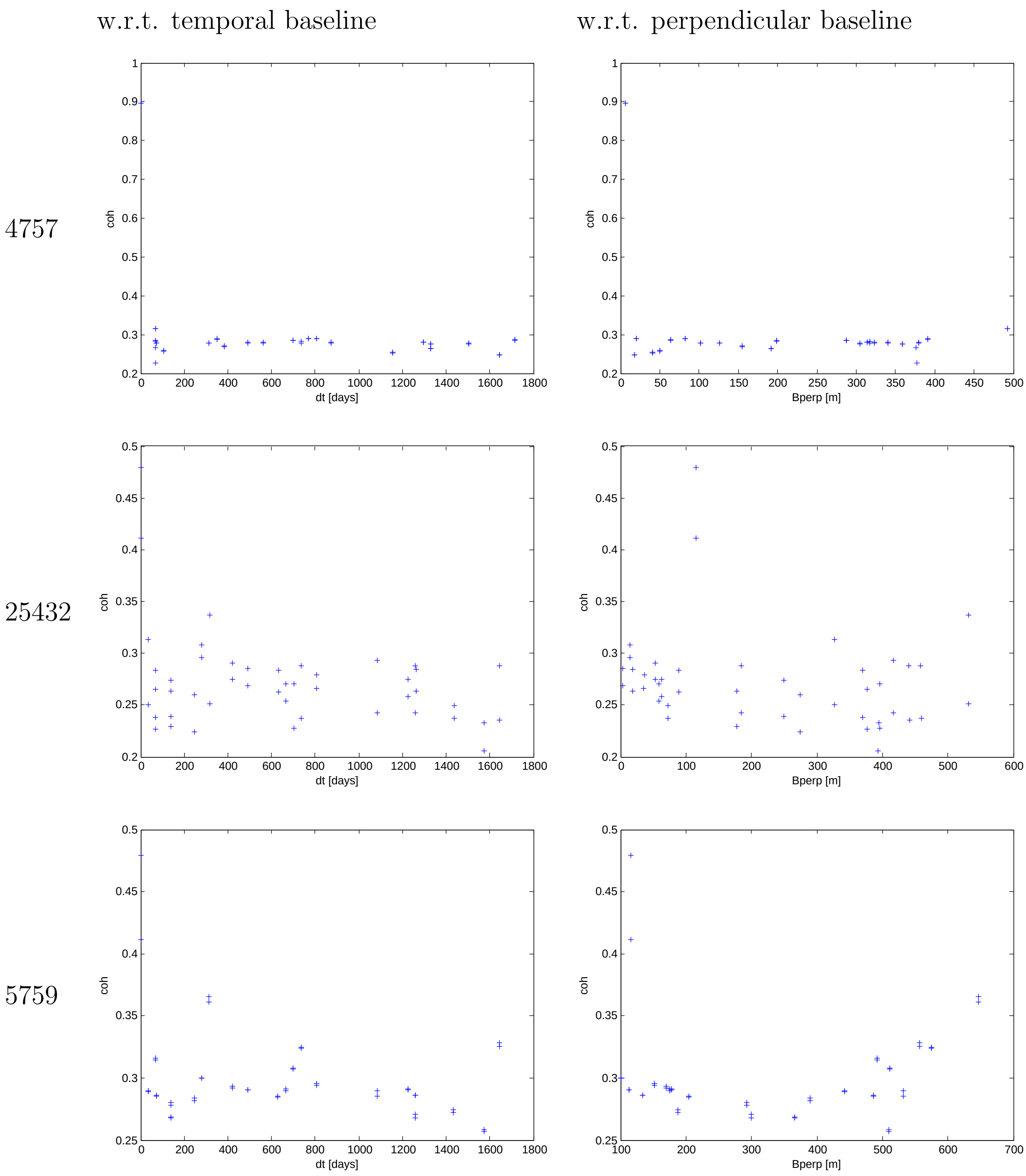

Figure A.10: Coherence with regard to the temporal and perpendicular baselines for the Košťany area for interferograms created from the scenes 4757, 25432 and 5759.

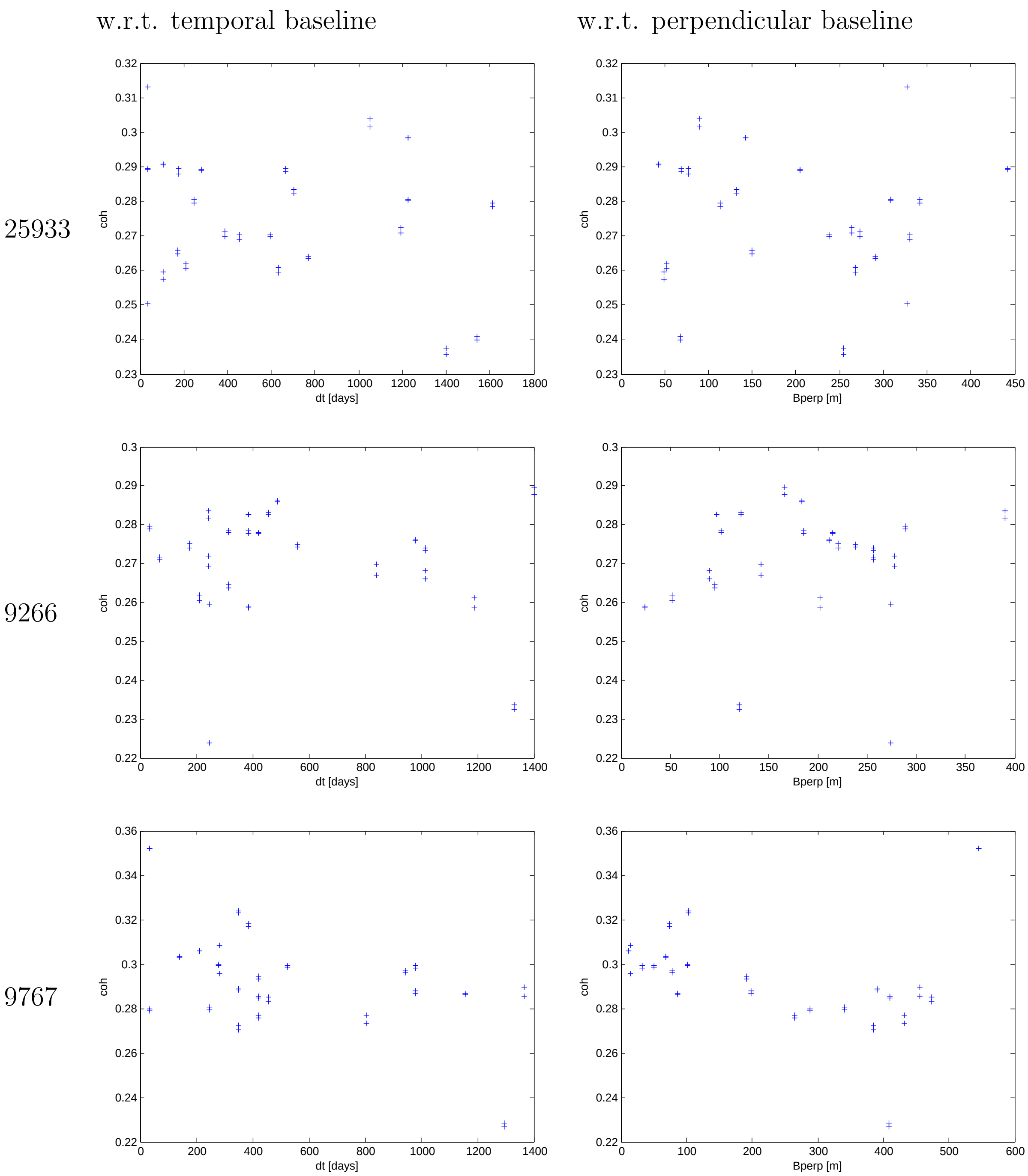

Figure A.11: Coherence with regard to the temporal and perpendicular baselines for the Košťany area for interferograms created from the scenes 25933, 9266 and 9767.

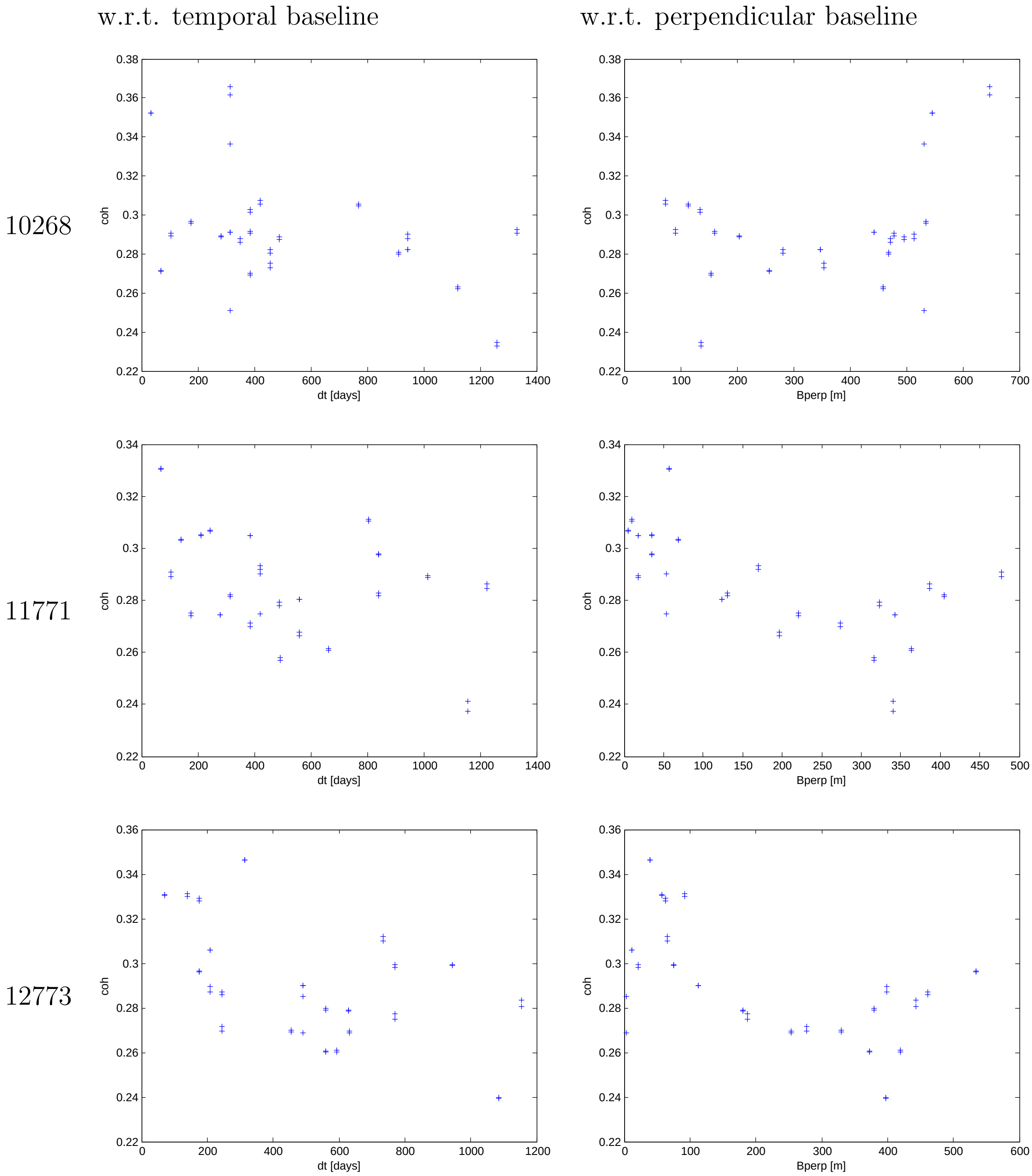

Figure A.12: Coherence with regard to the temporal and perpendicular baselines for the Košťany area for interferograms created from the scenes 10268, 11771 and 12773.

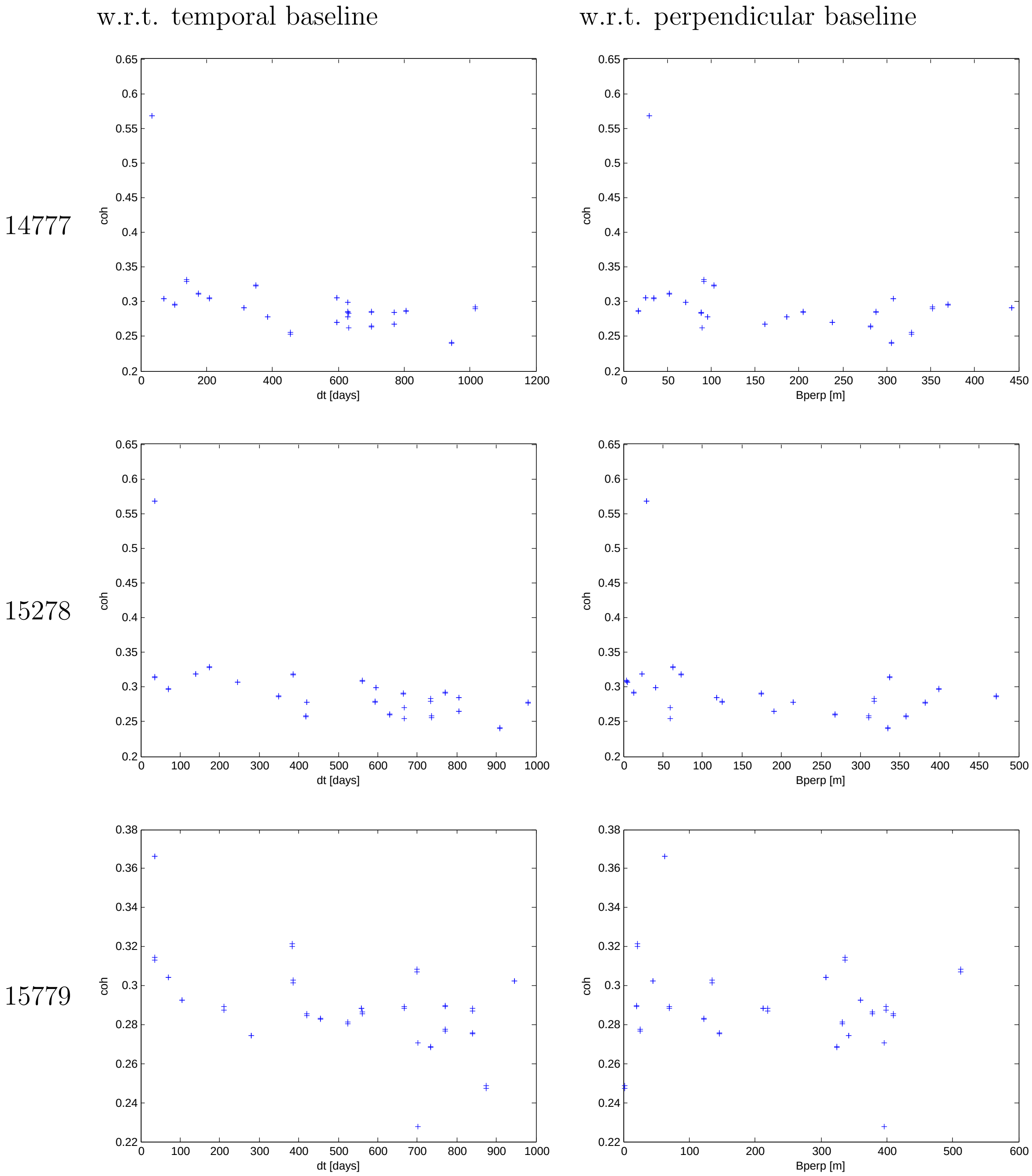

Figure A.13: Coherence with regard to the temporal and perpendicular baselines for the Košťany area for interferograms created from the scenes 14777, 15278 and 15779.

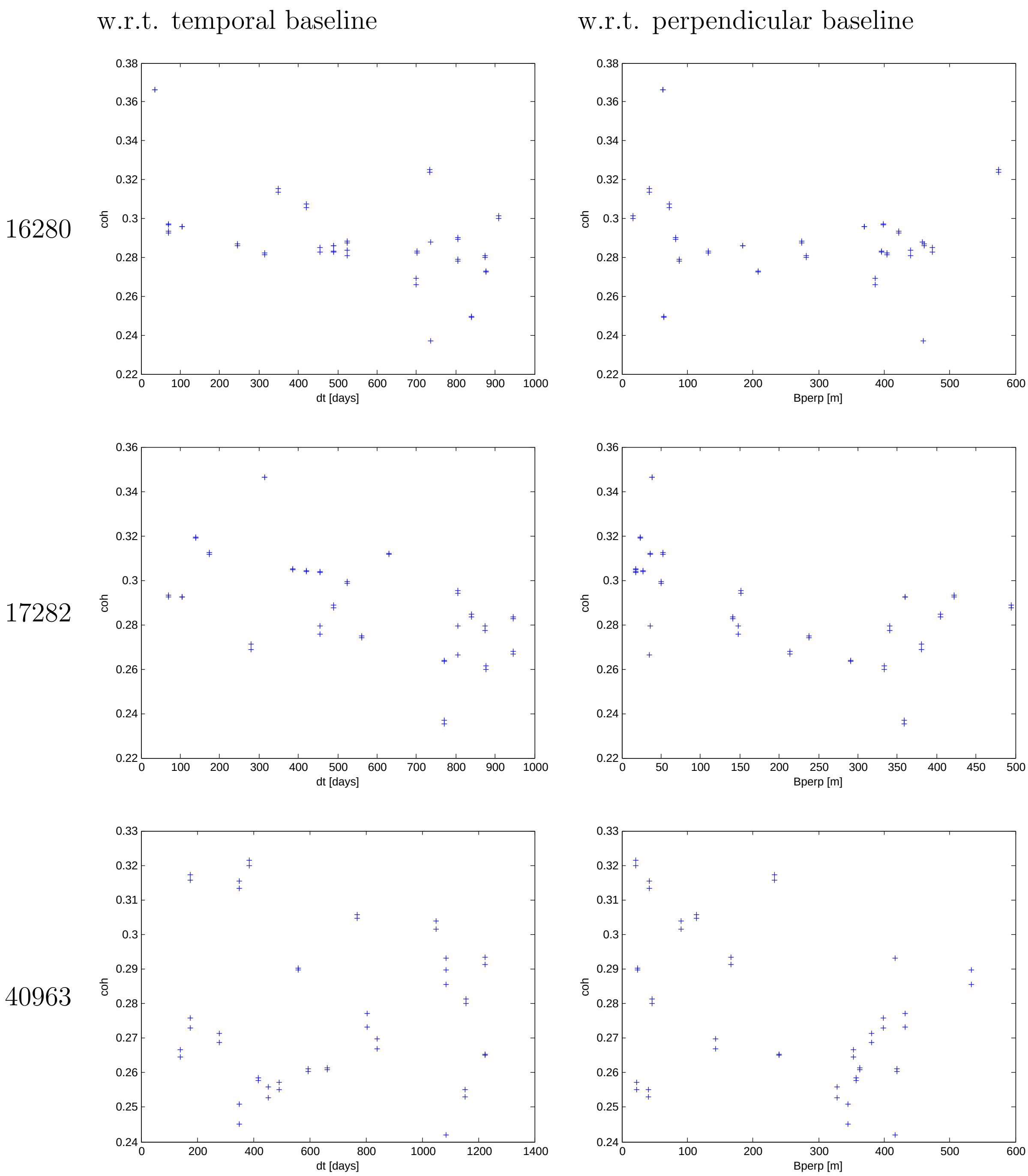

Figure A.14: Coherence with regard to the temporal and perpendicular baselines for the Košťany area for interferograms created from the scenes 16280, 17282 and 40963.

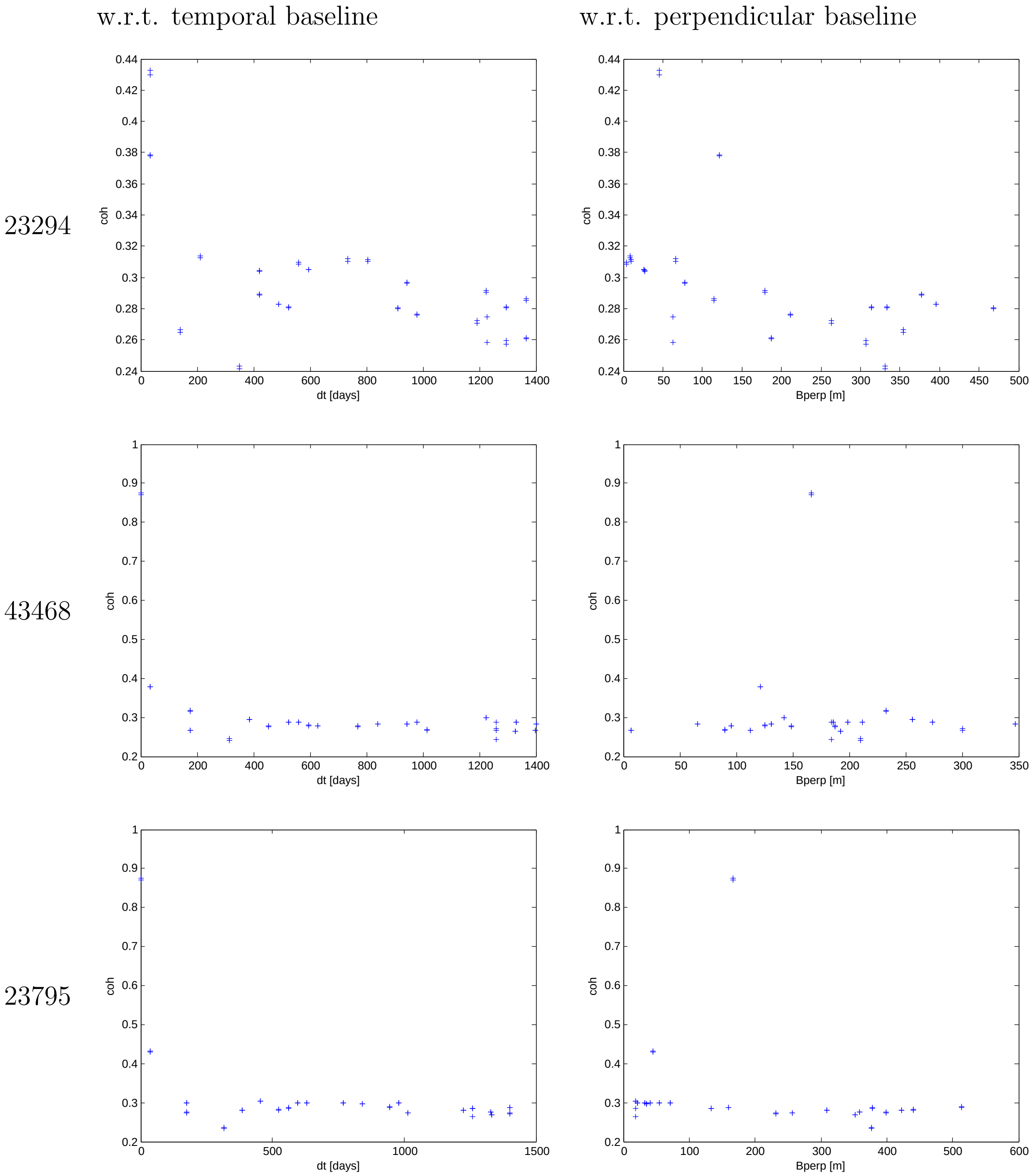

Figure A.15: Coherence with regard to the temporal and perpendicular baselines for the Košťany area for interferograms created from the scenes 23294, 43468 and 23795.

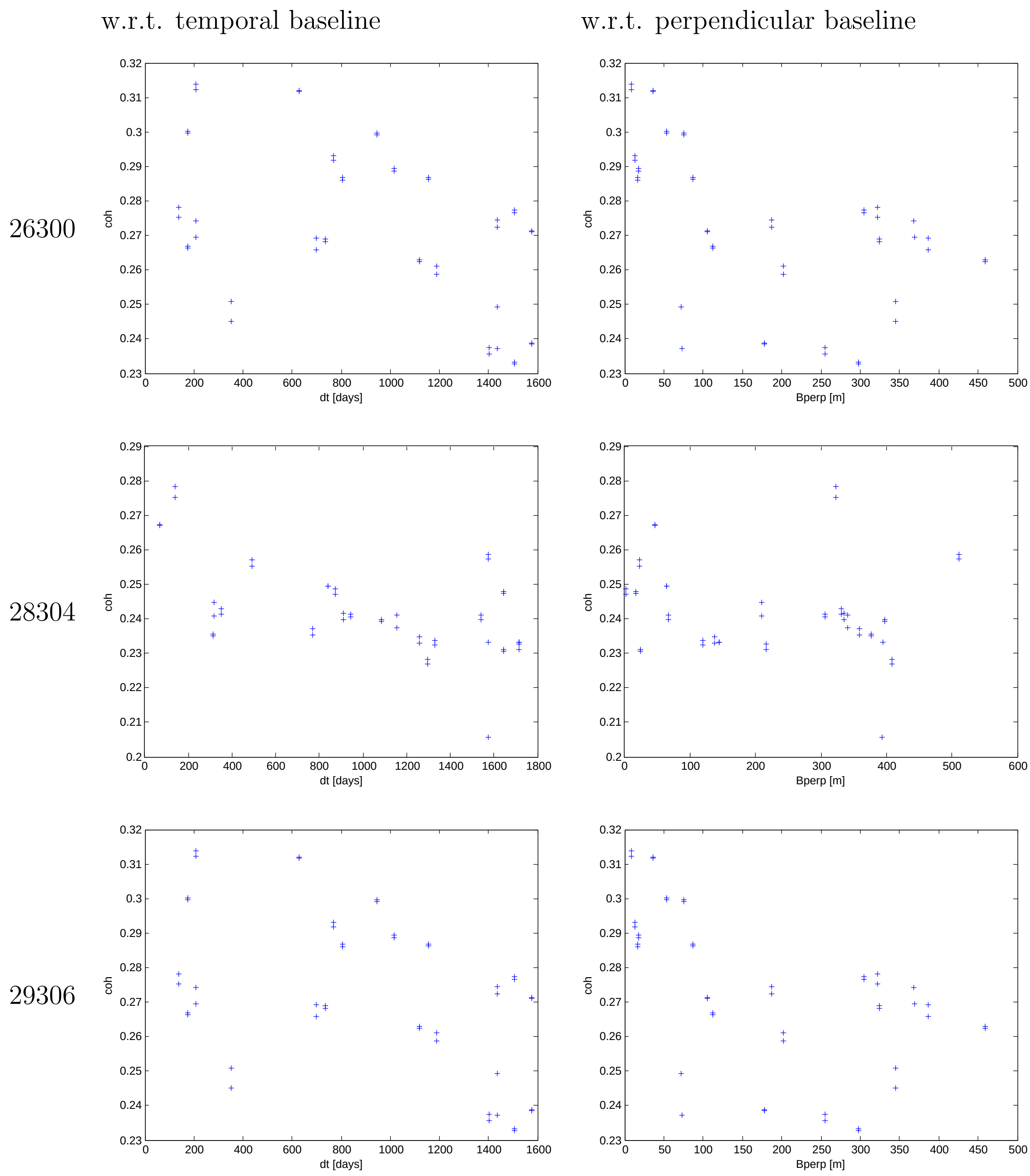

Figure A.16: Coherence with regard to the temporal and perpendicular baselines for the Košťany area for interferograms created from the scenes 26300, 28304 and 29306.

Appendix B

Detailed Results

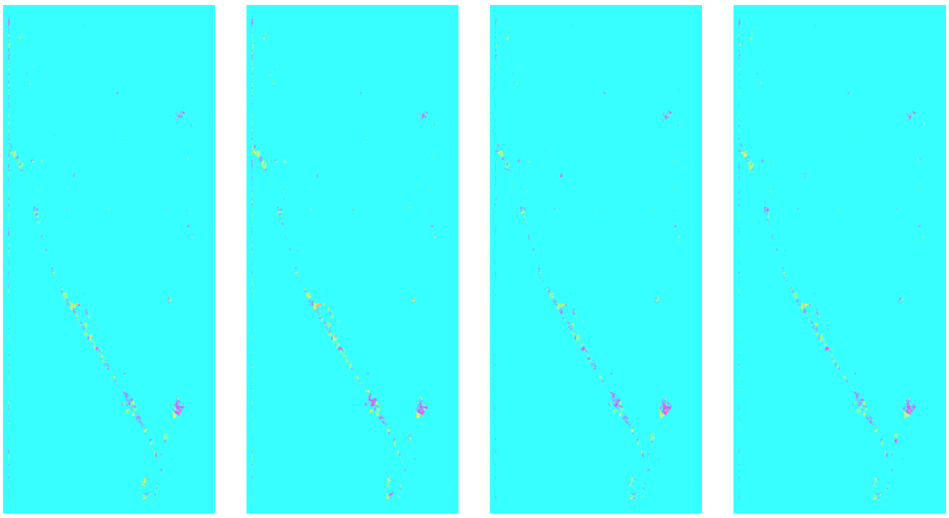

1996-01-07 (23428) | 1996-01-08 (3755) | 1996-03-17 (24430) | 1996-03-18 (4757)

Figure B.1: Deformation computed for the Ervěnice area – wrapped phase, deformation model. The deformations are with regard to 1997-03-03 (scene 9767). Scene 25432 (1996-05-26) was excluded due to high orbit errors, scenes 9266 (1997-01-27) and 29306 (2000-11-27) were excluded either during the interferogram selection, or during the consistency check process. Statistical test results were not taken into account for these results. The scale is imaged in figure B.2, with -150 mm on the left and 150 mm on the right. Not all the values are in this range – this only applies for the continuous region in the middle of the coherent area. The values of other pixels cannot be read out of this figure.

Figure B.2: Colorscale. The left and right borders are defined individually for each image.

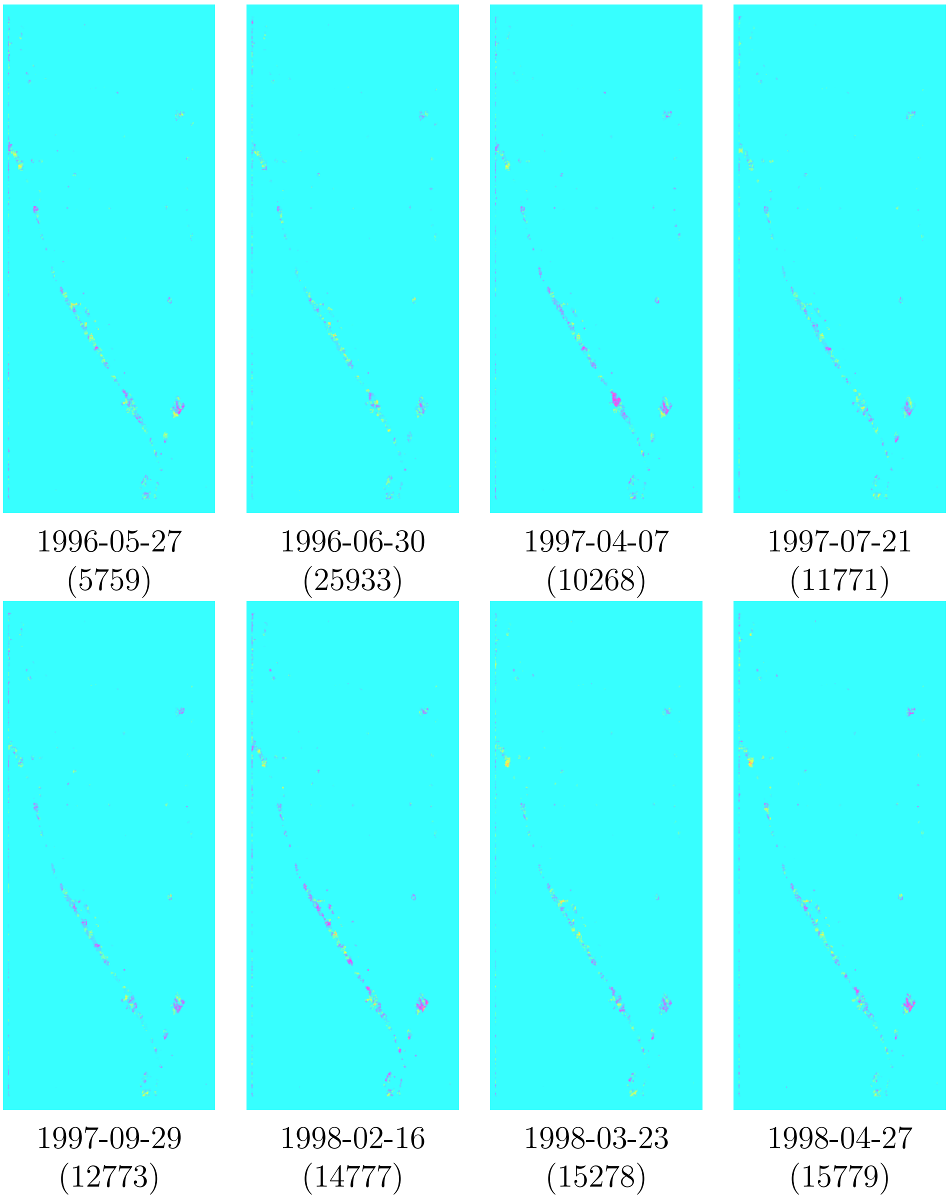

Figure B.3: Deformation computed for the Ervěnice area – wrapped phase, deformation model. The deformations are with regard to 1997-03-03 (scene 9767). Scene 25432 (1996-05-26) was excluded due to high orbit errors, scenes 9266 (1997-01-27) and 29306 (2000-11-27) were excluded either during the interferogram selection, or during the consistency check process. Statistical test results were not taken into account for these results. The scale is imaged in figure B.2, with -150 mm on the left and 150 mm on the right. Not all the values are in this range – this only applies for the continuous region in the middle of the coherent area. The values of other pixels cannot be read out of this figure.

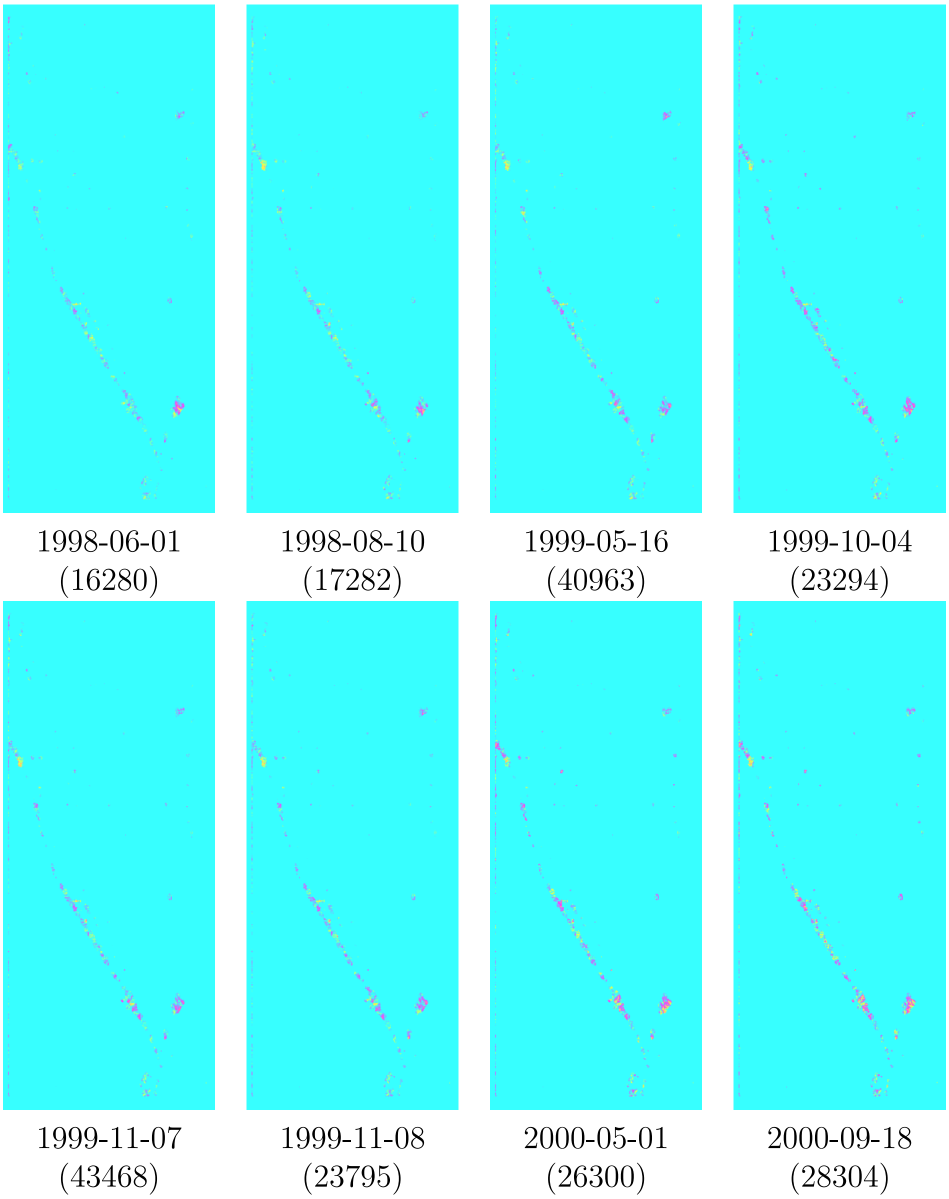

Figure B.4: Deformation computed for the Ervěnice area – wrapped phase, deformation model. The deformations are with regard to 1997-03-03 (scene 9767). Scene 25432 (1996-05-26) was excluded due to high orbit errors, scenes 9266 (1997-01-27) and 29306 (2000-11-27) were excluded either during the interferogram selection, or during the consistency check process. Statistical test results were not taken into account for these results. The scale is imaged in figure B.2, with -150 mm on the left and 150 mm on the right. Not all the values are in this range – this only applies for the continuous region in the middle of the coherent area. The values of other pixels cannot be read out of this figure.

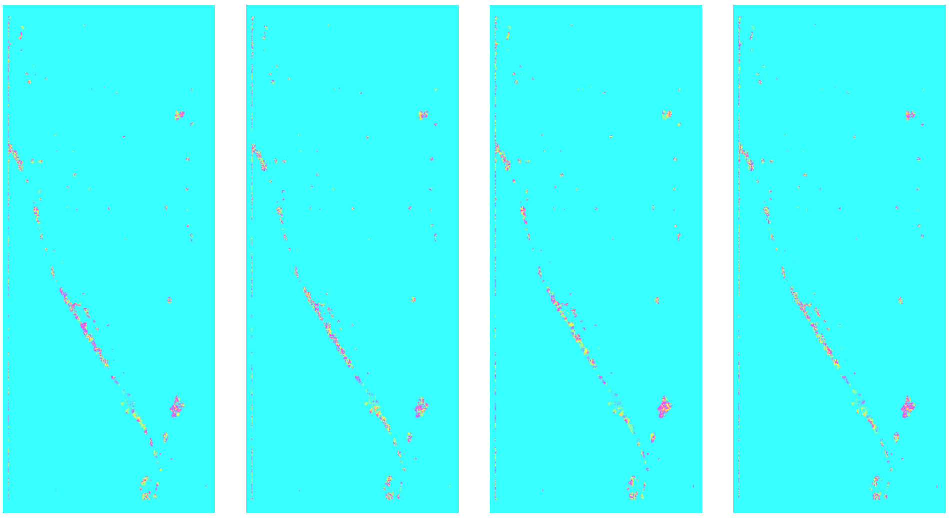

1996-01-07 (23428) | 1996-01-08 (3755) | 1996-03-17 (24430) | 1996-03-18 (4757)

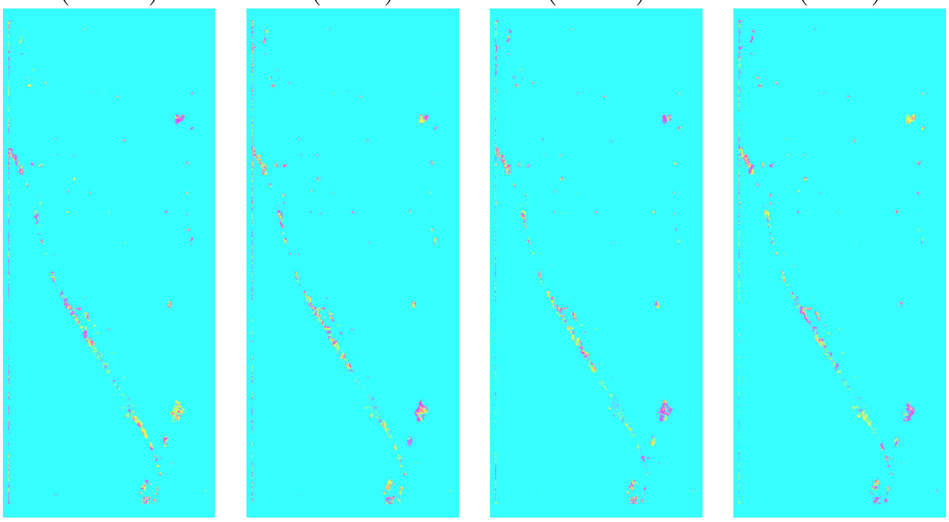

1996-05-27 (5759) | 1996-06-30 (25933) | 1997-04-07 (10268) | 1997-07-21 (11771)

Figure B.5: Deformation computed for the Ervěnice area – unwrapped phase, deformation model. The deformations are with regard to 1997-03-03 (scene 9767). Scene 25432 (1996-05-26) was excluded due to high orbit errors, scene 9266 (1997-01-27) was excluded either during the interferogram selection, or during the consistency check process. Statistical test results were not taken into account for these results. The scale is imaged in figure B.2, with -150 mm on the left and 150 mm on the right. Not all the values are in this range – this only applies for the continuous region in the middle of the coherent area. The values of other pixels cannot be read out of this figure.

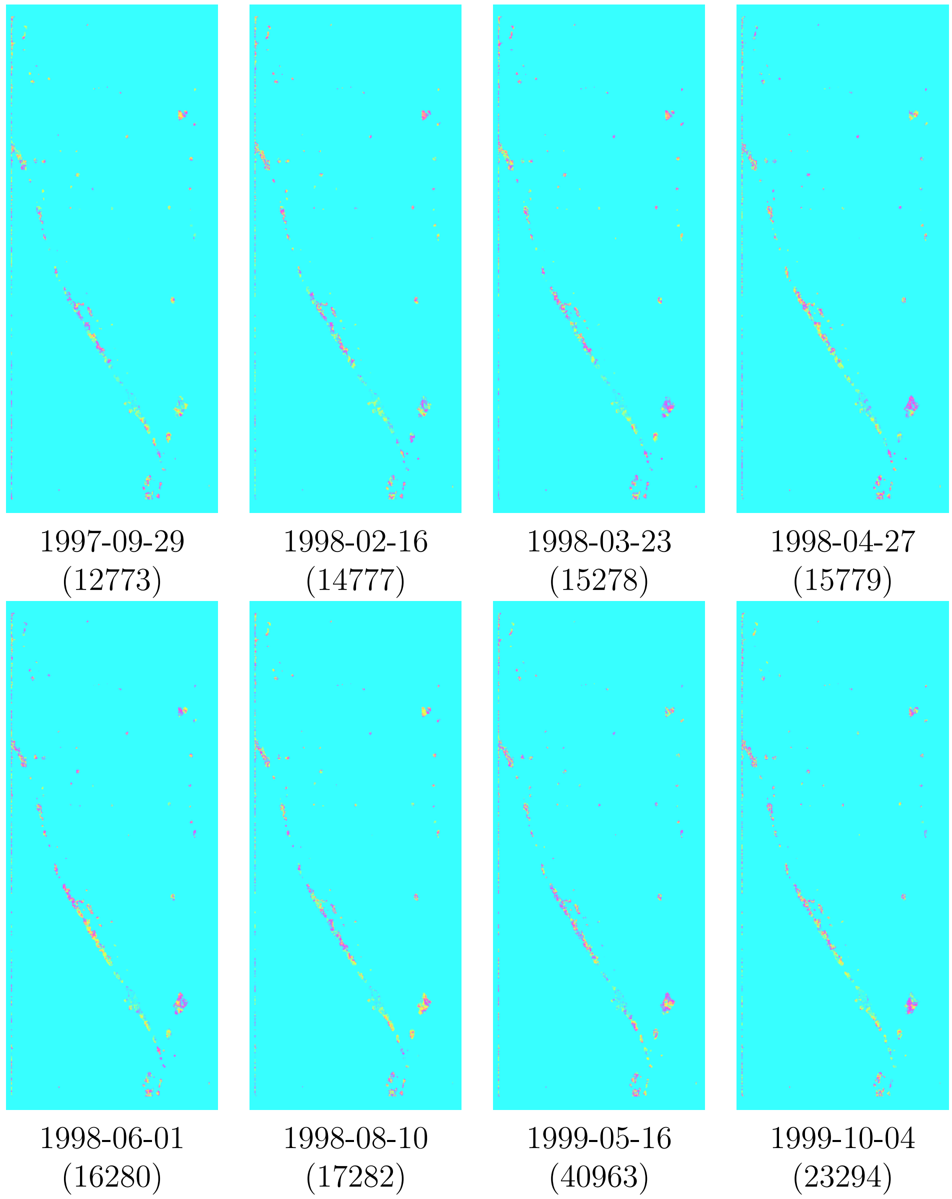

Figure B.6: Deformation computed for the Ervěnice area – unwrapped phase, deformation model. The deformations are with regard to 1997-03-03 (scene 9767). Scene 25432 (1996-05-26) was excluded due to high orbit errors, scene 9266 (1997-01-27) was excluded either during the interferogram selection, or during the consistency check process. Statistical test results were not taken into account for these results. The scale is imaged in figure B.2, with -150 mm on the left and 150 mm on the right. Not all the values are in this range – this only applies for the continuous region in the middle of the coherent area. The values of other pixels cannot be read out of this figure.

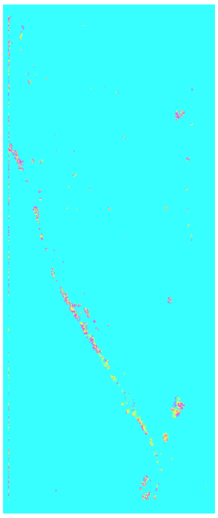

1999-11-07
(43468)

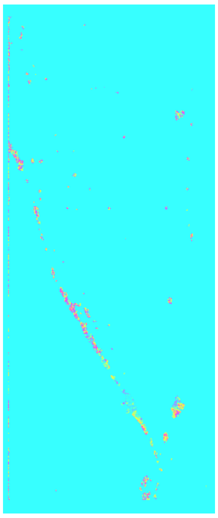

1999-11-08
(23795)

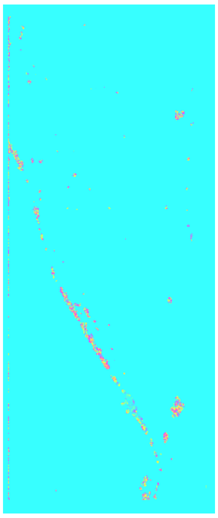

2000-05-01
(26300)

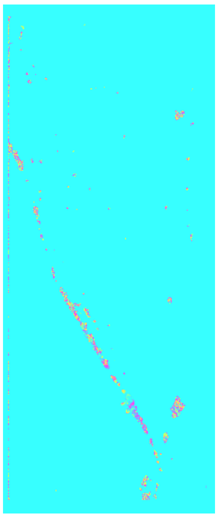

2000-09-18
(28304)

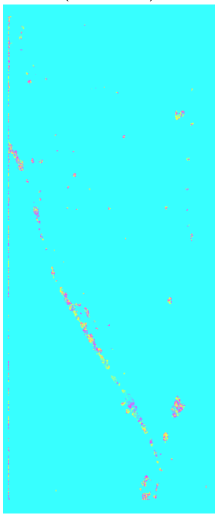

2000-11-27
(29306)

Figure B.7: Deformation computed for the Ervěnice area – unwrapped phase, deformation model. The deformations are with regard to 1997-03-03 (scene 9767). Scene 25432 (1996-05-26) was excluded due to high orbit errors, scene 9266 (1997-01-27) was excluded either during the interferogram selection, or during the consistency check process. Statistical test results were not taken into account for these results. The scale is imaged in figure B.2, with -150 mm on the left and 150 mm on the right. Not all the values are in this range – this only applies for the continuous region in the middle of the coherent area. The values of other pixels cannot be read out of this figure.

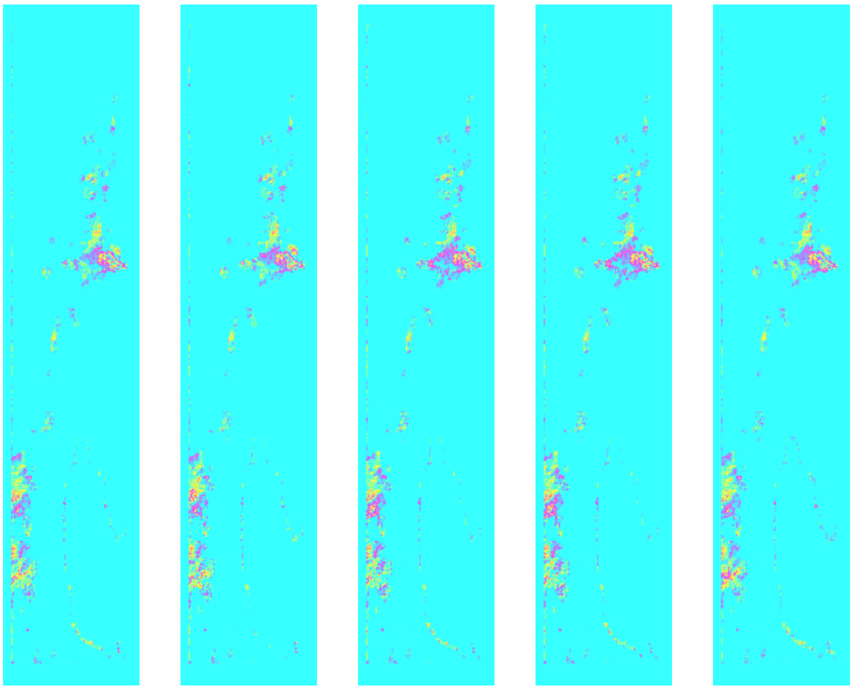

1996-01-07 (23428)	1996-01-08 (3755)	1996-03-17 (24430)	1996-03-18 (4757)	1996-06-30 (25933)

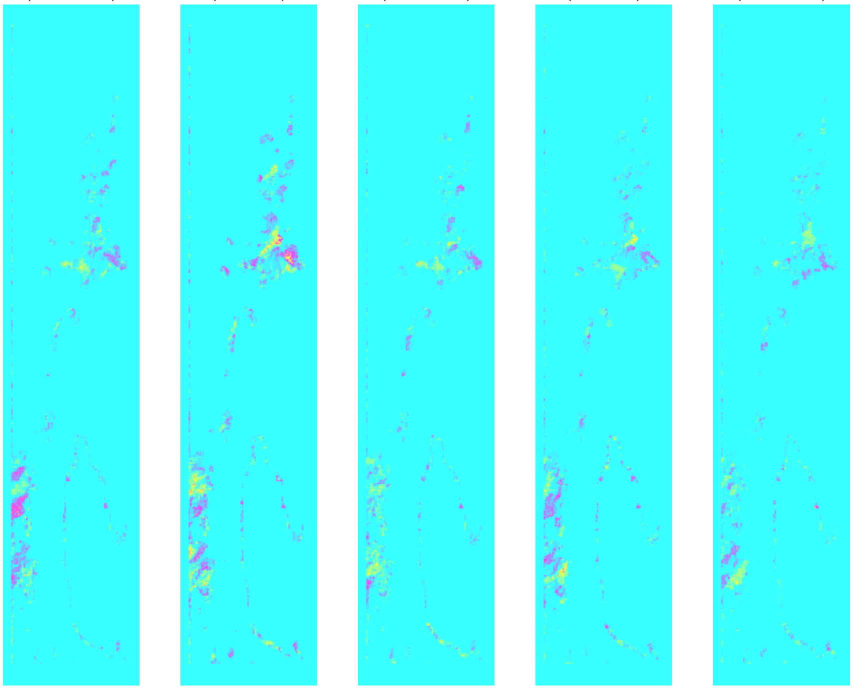

1997-03-03 (9767)	1997-04-07 (10268)	1997-09-29 (12773)	1998-02-16 (14777)	1998-03-23 (15278)

Figure B.8: Deformation computed for the Košťany area – wrapped phase, deformation model. The deformations are with regard to 1997-07-21 (scene 11771). Scene 25432 (1996-05-26) was excluded due to high orbit errors, scenes 5759 (1996-05-27) and 9266 (1997-01-27) were excluded either during the interferogram selection, or during the consistency check process. Statistical test results were not taken into account for these results. The scale is imaged in figure B.2, with -150 mm on the left and 150 mm on the right. Not all the values are in this range – this only applies for the continuous region in the middle of the coherent area. The values of other pixels cannot be read out of this figure.

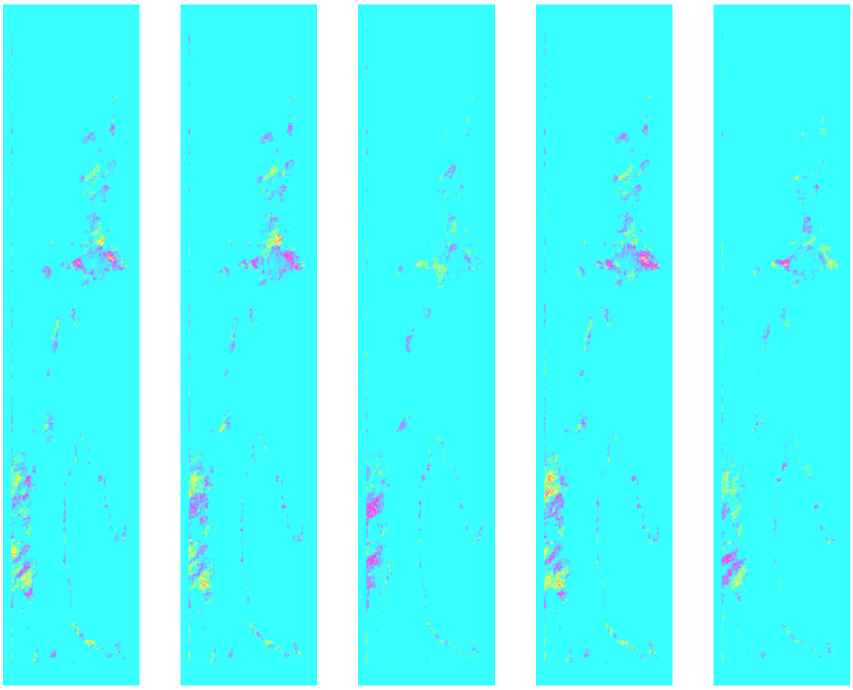

1998-04-27 (15779) 1998-06-01 (16280) 1998-08-10 (17282) 1999-05-16 (40963) 1999-10-04 (23294)

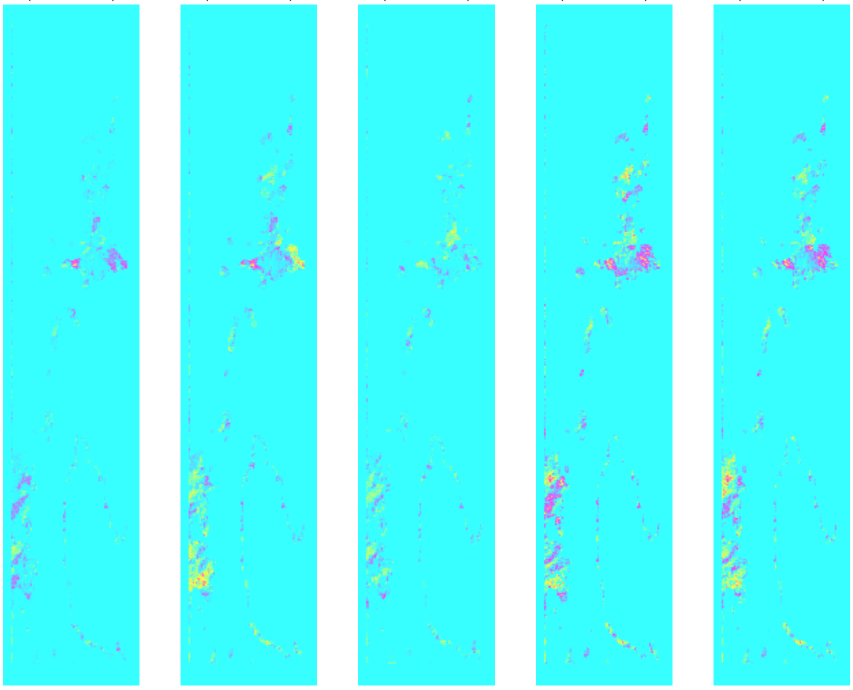

1999-11-07 (43468) 1999-11-08 (23795) 2000-05-01 (26300) 2000-09-18 (28304) 2000-11-27 (29306)

Figure B.9: Deformation computed for the Košťany area – wrapped phase, deformation model. The deformations are with regard to 1997-07-21 (scene 11771). Scene 25432 (1996-05-26) was excluded due to high orbit errors, scenes 5759 (1996-05-27) and 9266 (1997-01-27) were excluded either during the interferogram selection, or during the consistency check process. Statistical test results were not taken into account for these results. The scale is imaged in figure B.2, with -150 mm on the left and 150 mm on the right. Not all the values are in this range – this only applies for the continuous region in the middle of the coherent area. The values of other pixels cannot be read out of this figure.

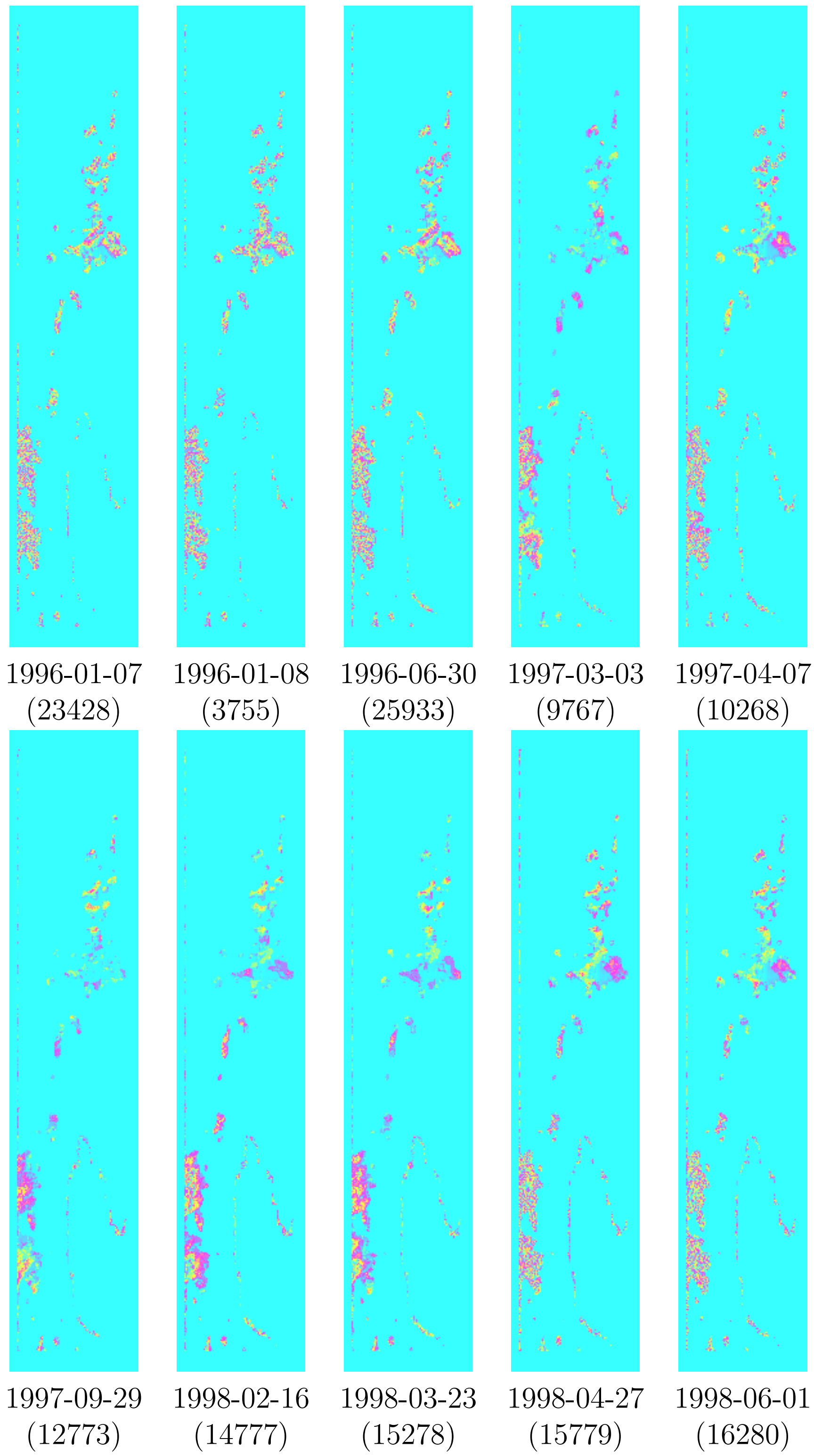

Figure B.10: Deformation computed for the Košťany area – unwrapped phase, deformation model. The deformations are with regard to 1997-07-21 (scene 11771). Scene 25432 (1996-05-26) was excluded due to high orbit errors, scenes 24430 (1996-03-17), 4757 (1996-03-18), 5759 (1996-05-27) and 9266 (1997-01-27) were excluded either during the interferogram selection, or during the consistency check process. Statistical test results were not taken into account for these results. The scale is imaged in figure B.2, with -150 mm on the left and 150 mm on the right. Not all the values are in this range – this only applies for the continuous region in the middle of the coherent area. The values of other pixels cannot be read out of this figure.

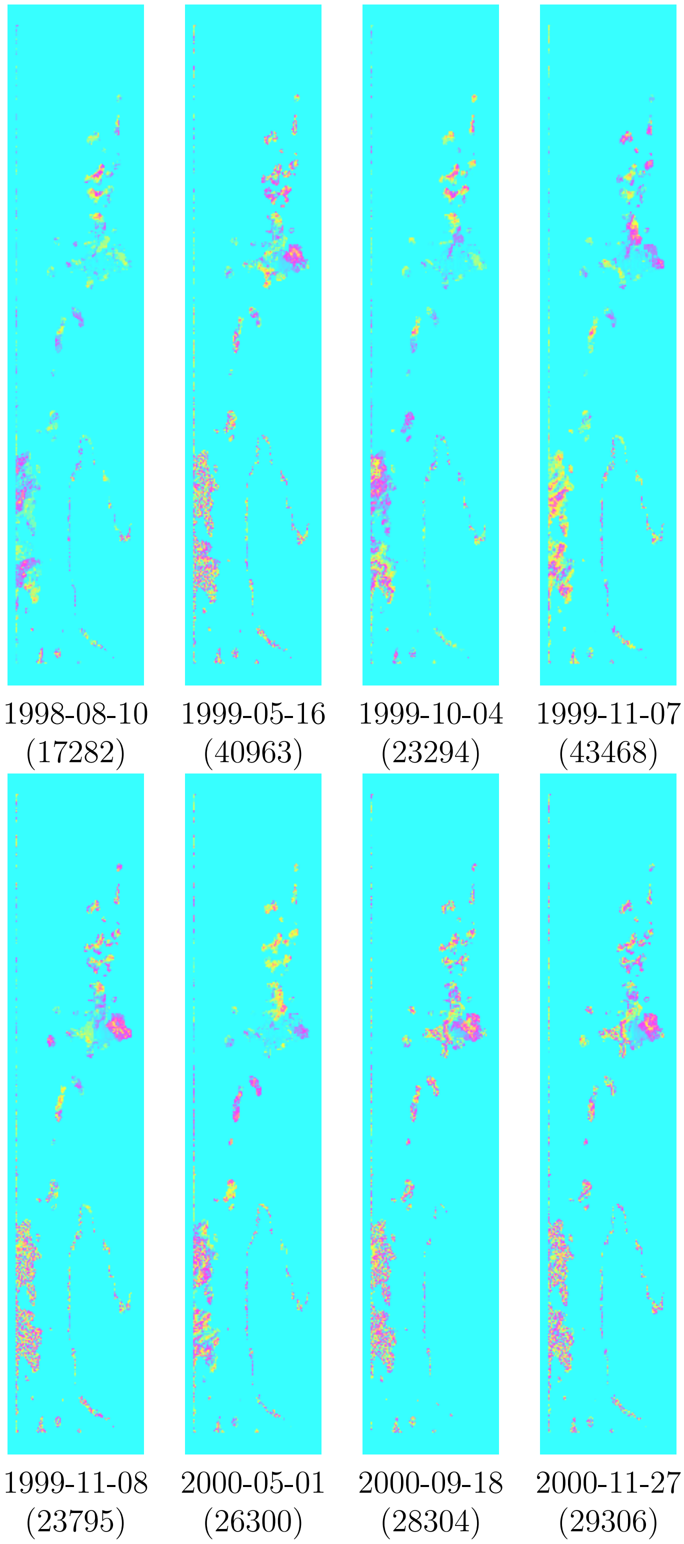

Figure B.11: Deformation computed for the Košťany area – unwrapped phase, deformation model. The deformations are with regard to 1997-07-21 (scene 11771). Scene 25432 (1996-05-26) was excluded due to high orbit errors, scenes 24430 (1996-03-17), 4757 (1996-03-18), 5759 (1996-05-27) and 9266 (1997-01-27) were excluded either during the interferogram selection, or during the consistency check process. Statistical test results were not taken into account for these results. The scale is imaged in figure B.2, with -150 mm on the left and 150 mm on the right. Not all the values are in this range – this only applies for the continuous region in the middle of the coherent area. The values of other pixels cannot be read out of this figure.